10-21-2022

Controlling Electro-Magnetic Functionality of Ruthenates by Heterostructure Design

Zeeshan Ali
Louisiana State University and Agricultural and Mechanical College

CONTROLLING ELECTRO-MAGNETIC FUNCTIONALITY OF RUTHENATES BY HETEROSTRUCTURE DESIGN

A Dissertation

Submitted to the Graduate Faculty of the
Louisiana State University and
Agricultural and Mechanical College
in partial fulfillment of the
requirements for the degree of
Doctor of Philosophy

in

The Department of Physics and Astronomy

by
Zeeshan Ali
M.Sc., University of Punjab, Lahore, Pakistan, 2014
M.S., Miami University, OH, 2018
December 2022

Acknowledgments

First, I am thankful to my research advisor Dr. Jiandi Zhang for his continual provision, academic mentorship, and supervision in my research. The completion of this thesis would not have been possible without Jiandi's valuable suggestions and leadership.

A very special thanks to Dr. Mohammad Saghayezhian for being my research mentor. Mohammad's advocacy, extensive breadth of knowledge, and intuition on all aspects of my work greatly benefited me and grow as a scientific researcher.

I must thank Dr. Zhen Wang and Dr. Yimei Zhu for scanning transmission electron microscopy experiments.

I like to thank my collaborators from Vanderbilt University: Dr. Sokrates T. Pantelides, Dr. Andrew O'Hara, and Dr. Donghan Shin for Density Functional Theory calculations, scientific inputs, and discussions. My sincerest thanks to RUTGERS collaborators: Dr. Weida Wu, Wenbo Ge, and Ying-Ting Chan for magnetic force microscopy. I am also obliged to Alessandro R. Mazza and Thomas Zac Ward from Oak Ridge National Laboratory for X-ray diffraction experiments. I am also thankful to Dr. Rongying Jin for her invaluable collaboration and lab sharing.

I must acknowledge my committee members, Dr. David Young, and Dr. Juana Moreno, as their advice greatly facilitated in shaping this thesis.

I am indebted to my lab mates, Dr. David Howe, Dr. Prahald Siwakoti, Dr. Roshan Nepal, Michael Wu, and Mojgan Dehghani. Thank you for creating a pleasant working environment, unflagging provision and lab-related efforts.

Lastly, to my dearest mother and sisters, a sincere thankfulness for constant care and inspiration.

Table of Contents

Abstract

Perovskite oxides (ABO_3) show wide range of functionalities originating from interplay of structural, spin, charge, and orbital degrees of freedoms. The bulk perovskite structure could be controlled via conventional chemical substitution, though exploiting heterostructure engineering novel ground states could be observed which otherwise are absent in bulk. In this thesis, the interest is to explore the electro-magnetic phenomena as complex oxides are confined in heterostructures.

I first investigate electromagnetic properties of ultrathin epitaxial ruthenate: $SrRuO_3$ (SRO); spatially confined between $SrTiO_3$ (STO) i.e., STO^5-SRO^n-STO^5 with n = 1- and 2-unit cells. It is shown that STO^5-SRO^2-STO^5 heterostructure is nearly stoichiometric, metallic, and ferromagnetic with $T_C \sim 128$ K, even though it lacks characteristic bulk-SRO octahedral tilts. In contrast, STO^5-SRO^1-STO^5 is accompanied by a loss of metallicity and ferromagnetism, though octahedron remains non-tilted. However, STO^5-SRO^1-STO^5 exhibits a substantial interface induced Ti-Ru intermixture, which is responsible for the loss of metallicity and ferromagnetism. The results highlight role of B-site non-stoichiometry and interface-induced intermixture.

Next, we report the emergent electro-magnetic properties in ultrathin $CaRuO_3$ films by unique "δ-doping" engineering i.e., atomically replacing A-site with single SrO layer, though keeping identical B-site (Ru). While bulk $CaRuO_3$ is metallic and nonmagnetic, the films confined to thickness of ~15-unit cells (u.c.) are insulating and remain nonmagnetic. However, δ-doping of SrO to middle of $CaRuO_3$ films induces an insulator-to-metal transition and unusual ferromagnetism, while retaining bulk-orthorhombicity. Through, atomically resolved structural analysis, density-functional-theory calculations as well as transport and magneto-transport, we find that emergent magnetic ordering is coupled to subtle electronic and structural effects introduced via A-site cation.

To further investigate effect of A-site on ruthenates functionalities, we employ heterostructure engineering to stabilize $Sr_{1-x}Ba_xRuO_3$ ($0 \leq x \leq 0.7$) films. The strain-stabilized Ba substitution transmutes lattice symmetry from bulk-like orthorhombic ($x = 0$) to cubic phase ($x = 0.2$) without RuO_6 rotations. The cubical film exhibits robust ferromagnetic ordering (T_c = 145 K) with a strong perpendicular magnetic anisotropy. Though, increased Ba-substitution significantly condenses the ferromagnetism, suggesting that besides determining octahedral distortion, the A-site introduces certain entangled electro-magnetic effects that greatly affect the ruthenates magnetic ordering.

Chapter 1. Perovskite Oxides

1.1 Introduction

The term "*Perovskite*" originated from a mineral with the chemical formula $CaTiO_3$ (calcium titanium oxide) and is named after Count Lev Aleksevich Von Perovski [1]. With time, numerous compounds were discovered possessing similar crystal structures as that of $CaTiO_3$, and nowadays perovskite designates a large number of compounds that adopt crystal structures analogous to $CaTiO_3$. Generally, perovskites have the formula ABO_3, where A is a big cation, B is a medium cation and O is oxygen. Cation A is usually alkali metal ion, or rare-earth lanthanoid, and B cation is transition metal. Perovskites are fundamentally attractive due to wide-spectrum functionalities, such as ferroelectricity, ferromagnetism, anti-ferromagnetism, colossal magnetoresistance, superconductivity, and piezoelectricity [1,2].

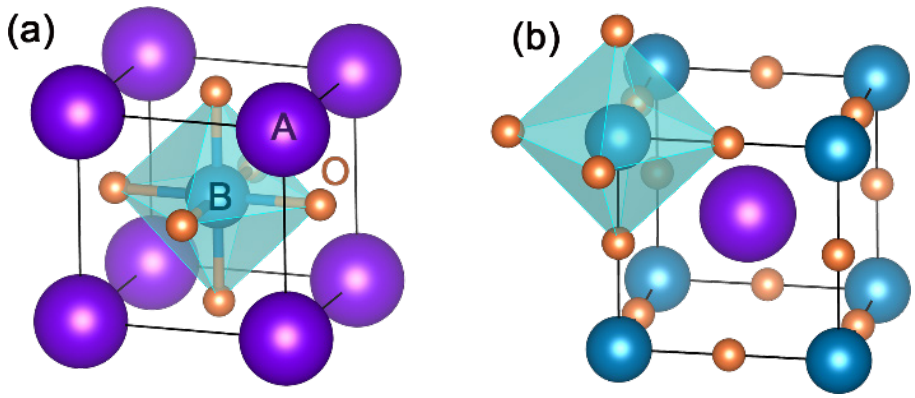

Figure 1.1. Crystal structure of perovskite. (a) B-cation at the cubic-cell center, and (b) A-cation at the center of unit-cell.

The ideal perovskite structure is cubic such as $SrTiO_3$, but this is rare. There are two overall methods to represent cubic unit cell. At first, the origin of coordination is considered at the location of the A-atom (Sr atom) (0, 0, 0). The B-cation (Ti-atom) resides at center (½, ½, ½), and oxygen atoms are at face centers as in Figure 1.1(a). Thus, B-cation (Ti^{4+}) is 6-fold coordinated to the O^{2-} ions, hence forming an octahedron, while A-atom residing in the

interstices is coordinated to 12 anions. However, sometimes, it is beneficial to move the origin to the B-site. In this case, the large A-atoms, are now positioned at the unit cell center (½, ½, ½), while oxygen is placed between the B-atoms [see Figure 1.1(b)].

1.2 Structural Distortion

The ideal perovskite structure is cubic, though most perovskites exhibit various types of structural distortions due to mismatch between A and B cations radii, leading to a lower symmetry structure such as tetragonal, orthorhombic, monoclinic, triclinic, and rhombohedral. The prediction criteria for distortion is given by the tolerance factor (t) suggested by Goldschmidt as [1]: $t = \frac{r_A + r_o}{\sqrt{2}(r_B + r_o)}$. Here, r_A, r_B are A and B cations radii, respectively, and r_o oxygen radius. If we have $0.9 < t \leq 1$, then a cubic perovskite structure is preferred. If t = 0.71-0.9, then A-site is too small, which leads to a strain upon the octahedral network. The strain is accommodated via BO_6 octahedral rotations, leading to lower-symmetry structures. The decreased crystal symmetry is more often associated with the distortions that emerge in form of octahedral rotations, which are explained by Glazer notation [3]. On other hand, $t > 1$ implies a very large A-site or very small B-site, consequently, hexagonal and tetragonal structures are preferred. In this case, the off-centering of B-cation in the BO_6 octahedral could be observed. Lastly, in some systems, the electronically-driven distortions of octahedral (shape distortion) caused by a Jahn-Teller effect are also present. Three kinds of distortions might happen independently or can emerge collectively. These structural distortions are not only important in the perspective of crystallography but also post significant effects on the physical properties.

1.2.1 Octahedron Rotations

The most extensive distortions in perovskites are rotations of the octahedron. This kind of distortion is typically related to the placement of small A cations ($t < 1$), hence, the BO_6 octahedra rotates to efficiently decrease perovskite cavity dimensions. Glazer notation is

employed to describe these octahedral rotations/tilts [3]. In Glazer notation, a tilt system is designated by rotations of the octahedron around three orthogonal pseudo-cubic crystallographic axes. Glazer notation utilizes three labels $a^x\ b^x c^x$, where *a, b* or *c* denotes crystallographic axes [see Figure 1.2(a)]. The superscript x refers to whether adjacent octahedral can rotate in-phase (+), out-of-phase (–), or no rotation (0). Therefore, BO_6 could remain unrotated ($x = 0$) [Figure 1.2(b)], or the octahedra could rotate in-phase ($x = +$) [Figure 1.2(c)] or out-of-phase ($x = -$) [Figure 1.2(d)]. An additional parameter is the specification of rotation magnitude about an axis relative to the other crystallographic axes. The rotation angle magnitude is signified by *α*, *β,* or *γ,* respectively. The relative magnitudes are represented by letters *a*, *b*, or *c*, respectively, for example, *aac* implies equal rotations about [100] and [010] axes and different one around [001].

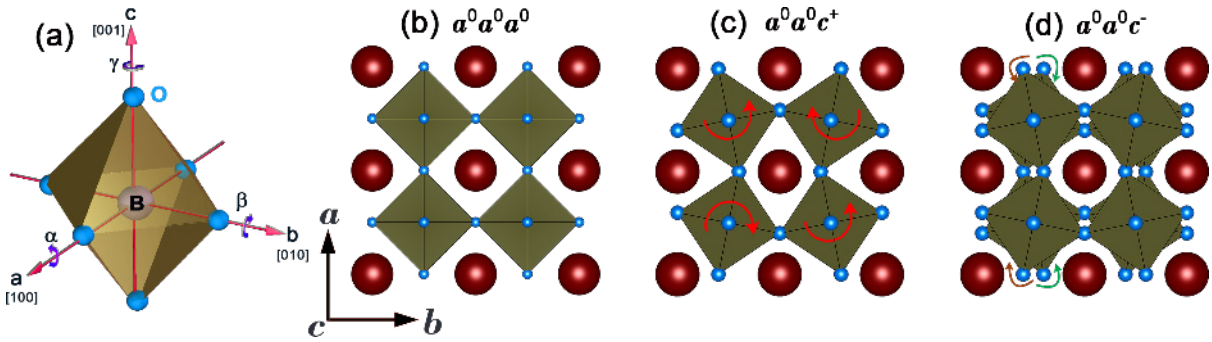

Figure 1.2. (a) Schematics of Glazer rotations. (b) no rotations, (c) in-phase, and (d) out-of-phase octahedral rotation.

It should be noted that distortion is dependent on the fact that the octahedral has to strictly preserve its corner connectivity, while approximately upholding its regularity. The undistorted perovskite shows $a^0a^0a^0$, where $\alpha = \beta = \gamma = 0°$, as in Figure 1.2(b). Two of the simplest examples of rotations are $a^0a^0c^+$ and $a^0a^0c^-$. In case of $a^0a^0c^+$ tilt system, it implies no rotation about *a*, and *b* axes, while rotation is in-phase around the *c*-axis [Figure 1.2(c)]. While in $a^0a^0c^-$, [Figure 1.2(d)], the octahedral along the *c*-axis, and the underlying octahedral (viewing into the page) rotate oppositely.

1.2.2 Electronic Structure Variation

In the perovskite structure (ABO_3), the B-site cation is selected from transition metal with *d*-orbitals. Since B site cation is always surrounded by 6 oxygen anions, the Coulomb repulsion among *d* orbital electrons and the surrounding oxygen *p* orbital electrons produce a crystal field. Consequently, the five-fold *d*-band degeneracy is partially lifted. Thereby, in an ideal octahedron, the orbitals split into two states: a 3-fold degenerate lower-energy t_{2g} consisting of the d_{xy}, d_{yz}, d_{xz} orbitals and a 2-fold degenerate higher energy e_g orbitals $d_{x^2-y^2}, d_{z^2}$. The *d*-orbitals in an BO_6 octahedral unit point towards or between the oxygens, whereas the lobes of t_{2g} comprising d_{xy}, d_{yz}, d_{xz} lies in yz, xy, and xz planes, respectively. However, the oxygen *p*-orbitals are along either $x, \mathrm{y}, or\ z$ axes, therefore t_{2g} orbitals $\left(d_{xy}, d_{yz}, d_{xz}\right)$ being at some distance from *p*-orbitals experiences lower repulsion. As a result, these t_{2g} are degenerate and are lower in energy. On the other hand, the e_g manifold comprising d_{z^2} and $d_{x^2-y^2}$ orbitals are directed along bonding axes and hence have stronger overlap with O-*p* orbitals, leading to strong repulsion from ligands and hence higher energy.

Consider a transition metal ion having an odd number of electrons in outmost e_g orbitals, for example, $Mn^{3+};\ d^4$: t_{2g}^3, e_g^1 have a degenerate ground state since it has two possible equal electron distributions. In this scenario, one of the electrons could go into either $d_{x^2-y^2}$ or d_{z^2}, leading to degenerate ground state energy. In 1937, Hermann Jahn and Edward Teller articulated that a metal-ion possessing a symmetrical atomic configuration and a degenerate ground state is unstable, therefore it undergoes a distortion to achieve lower energy, lifting the electronic degeneracy [1]. For example, a structural distortion can occur in the form of compression or elongation of BO_6 octahedra as shown in Figure 1.3. Therefore, via compression or elongation of the octahedra, the degeneracy is lifted by an additional splitting of the t_{2g} and e_g states. Octahedral elongation in so called Jahn Teller effect occurs when the degeneracy is lifted via

lowering of energy (achieving stability) of the *d* orbitals possessing a z-component, whereas the *d*-orbitals without z-component undergo a destabilization thus having higher energy. In the JT effect, due to $d_{x^2-y^2}$ antibonding nature, the $d_{x^2-y^2}$ increases its energy (while d_{z^2} is lowered in energy) because of elongation.

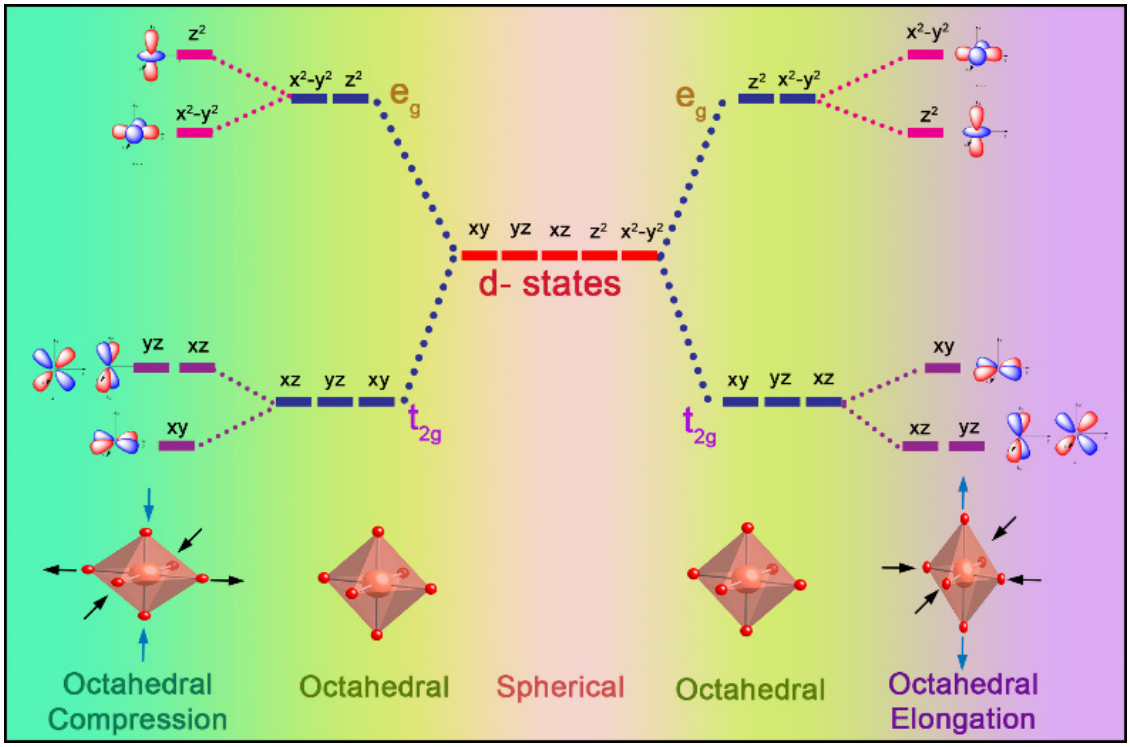

Figure 1.3. Schematic diagram of crystal field splitting and Jahn-Teller effect on *d*-electron energy levels for a B-site cation in an octahedra.

1.2.3 B-cation Displacement

This type of distortion could be pictured as in which the oxygen cage of BO_6 preserves its shape (or almost) but the B-cations undergo a displacement away from their central position of the octahedra. The B-cation displacement effect applies to nonlinear molecules having a nondegenerate ground state. As a result, the octahedral distortion happens which assists in a mingling of the ground state and excited state, thereby resulting in the lowering of ground state energy. The modification in symmetry is brought via the displacement of B-cation for example, $BaTiO_3$. To have a maximum degree of symmetry, the B-cation displacement should be along

octahedron symmetry axes [Figure 1.4]. The associated displacement give rise to electric dipoles, leading to ferroelectric effect.

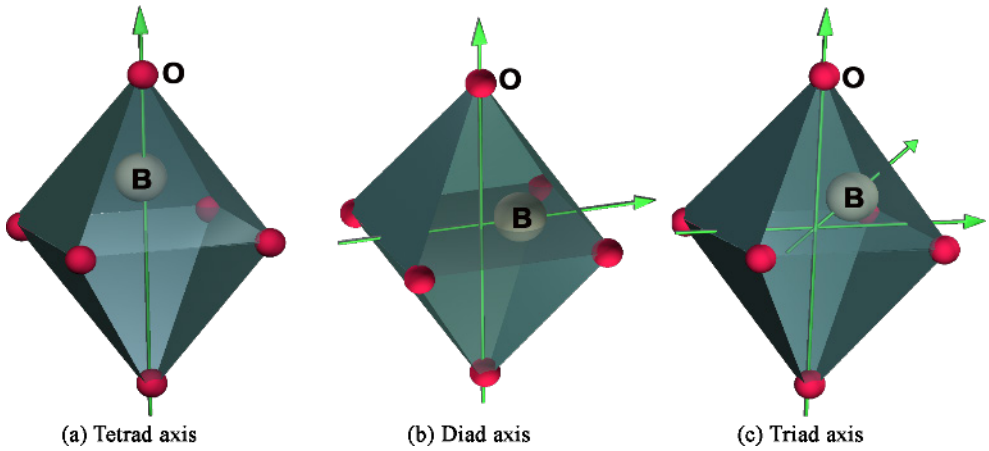

Figure 1.4. The potential shifts of B-site cation along three symmetry axes of an octahedral cage.

1.3 Manipulation of Perovskite Structures

The perovskite functionalities are mostly ascribed to the corner-sharing BO_6 octahedral unit. The distortion of the octahedral unit in form of rotation angles (varying B-O-B bonding angle), BO_6 size and shape (B-O bond lengths), and its connectivity can modify the chemical bonds and orbital hybridization via altering the transition metal (B-site) *d*-orbitals and oxygen 2*p*-orbitals overlap, thereby impacting perovskite properties. This section, therefore, provides details on perovskite structural manipulation via employing the epitaxial thin films approach. The epitaxial-strain engineering route to control and manipulate the perovskite oxides is explained. Besides, the interfacial-octahedral coupling route as an additional parameter to modify octahedra near the hetero-interface is discussed.

1.3.1 Epitaxial Strain Engineering

Thin-film epitaxy is the development of a single crystal material on a single crystal surface. The epitaxial approach is categorized into two types: (1) homoepitaxy, where both film and substrate belong to similar material, and (2) heteroepitaxy - when two are different. In

epitaxial film growth, because of lattice mismatch, the film undergoes strain given as $\varepsilon_{xx} = \frac{a_{sub} - a_{bulk}}{a_{bulk}}$. Here, a_{sub} and a_{bulk} are pseudo-cubic lattice parameter of substrate and the film (material to be deposited), respectively.

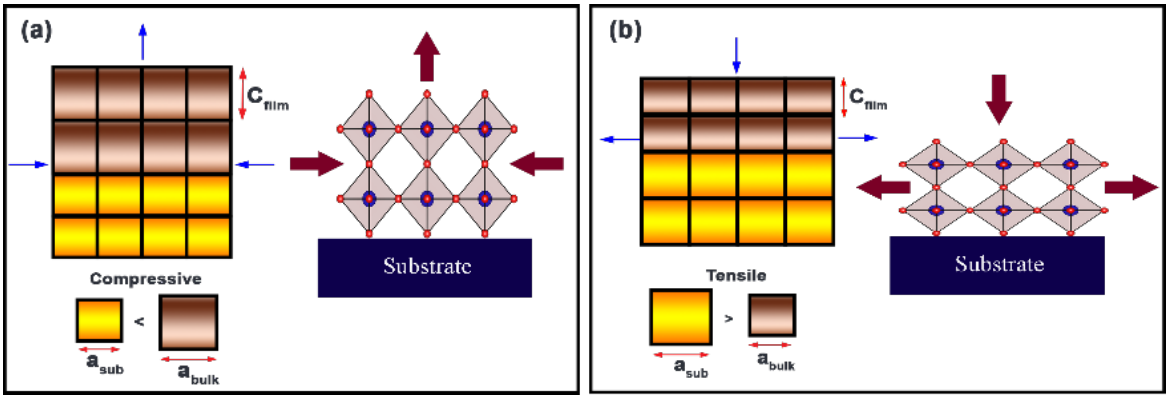

Figure 1.5. Illustration of (a) compressive, and (b) tensile strain.

If the lattice spacing of the material to be deposited (a_{bulk}) is greater than the substrate lattice spacing (a_{sub}), the film experiences compressive strain [Figure 1.5(a)]. However, if the lattice spacing a_{bulk} of the material to be deposited is smaller than the lattice spacing of the substrate a_{sub}, the film undergoes tensile strain [see Figure 1.5(b)]. The epitaxial film growth enforces the growing thin-film material to have an identical in-plane lattice constant. In the situation of dissimilar lattice constants, the thin film attempts to have the similar in-plane lattice parameter, thereby initiating structural modifications in form of unit cell parameters. The modified in-plane film lattice parameter outcomes in a unit-cell distortion in such a way that the out-of-plane lattice parameter is modified to conserve the unit-cell volume. Thus, in the compressive strain case, the film inplane parameter undergoes compression, while the out-of-plane parameter elongates. In contrast, tensile strain results in the in-plane parameter expansion and compression of the out-of-plane lattice parameter. Such modification in lattice parameters directly proposes that the structural symmetry of the film is changed from its bulk counterpart.

A considerable portion of modification in the film unit cell induced by epitaxial stresses

is accommodated via changing the octahedral size, and shape (B-O bond lengths are altered). At the same time or otherwise, the octahedra unit can accommodate the changes via changing the octahedral rotation/tilt pattern. The underlying substrate plays a pivotal part in defining the octahedral rotations/tilt pattern of the film. For example; the orthorhombic $SrRuO_3$ as a result of compressive strain displays a distorted orthorhombic structure (monoclinic) with $a^+a^-c^-$ tilt system [4,5]. In contrast, orthorhombic $SrRuO_3$ under tensile strain on $DyScO_3$ (orthorhombic) changes to a unit cell with $a^+a^-c^0$ tilt system [4,5]. Therefore, the orthorhombic perovskites with controlled epitaxy provide an efficient engineering platform to tune the lattice structure, which in turn modifies the bandwidths and electro-magnetic interactions.

1.3.2 Interfacial Octahedral Coupling

Besides providing an epitaxial strain, the perovskite substrate enforces a certain constraint that octahedral should preserve the corner connectivity. Therefore, the octahedral corner-connectivity constraint permits the octahedral rotations/tilts existing in the substrate or buffer layer to be transported across the interfaces [6–8]. In other words, at the heteroepitaxial interface between two perovskite oxides, the octahedral tilt patterns must match to preserve octahedral connectivity. Therefore, the hetero-interfacial octahedral coupling in conjunction with strain offers a systematic approach to tune the octahedral connectivity, and tilt/rotations. In this regard, an important parameter is the distance over which octahedral rotations/tilt patterns penetrate, normally 7-8-unit cells, though it is material dependent. Nevertheless, the interface engineering approach enforces the octahedra to distort, and modify rotation/tilt patterns, while maintaining corner connectivity near substrate-film heterojunction, thereby offering the opportunity to tune the octahedral behavior and achieve new functionalities.

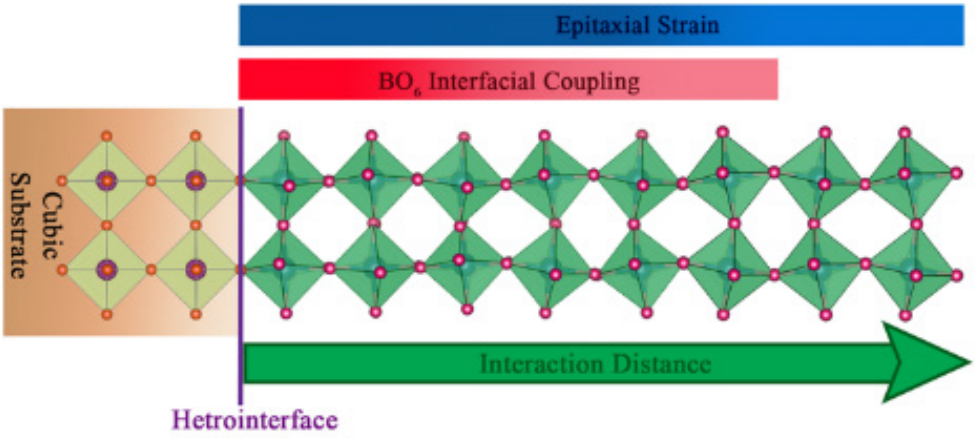

Figure 1.6. Schematic representation of interfacial octahedral coupling for decreased symmetry film on a cubic substrate.

1.4 Materials of Interest

Electro-magnetic interaction coupling to lattice structure is one of the most complicated subjects in condensed matter and perovskite ruthenates: $ARuO_3$ (A = Ba, Cr, or Sr) are an example of such intricacy. In this thesis research, I will exploit thin films of the ruthenates since they display various facets of electronic and magnetic behavior.

1.4.1 Strontium Ruthenate

The 4*d* transition metal oxide-$SrRuO_3$ (SRO) is a 4*d* mixed itinerant ferromagnet [9] having a bulk $T_C \sim 160$ K and orthorhombic structure [see Figure 1.7(a)], driven via ionic $[\mathrm{Sr}\ (1.18\ \text{Å}), \mathrm{Ru}\ (0.62\ \text{Å})]$ radii mismatch, leading to octahedral rotations. The orthorhombic SRO lattice parameters are: $a = 5.56$ Å, $b = 5.53$ Å, and $c = 7.84$ Å with a pseudocubic lattice parameter of $a_{pc} = 3.93$ Å [10]. The orthorhombic unit-cell $a_o \neq b_o \neq c_o$ and $\alpha = \beta = \gamma$ is related to pseudocubic unit cell as $a_o = \sqrt{2}\, a_c, b_o = \sqrt{2}\, a_c$, and $a_o = 2\, a_c$.

In Glazer notation, the tilt system $a^+b^-c^-$ (*Pbnm* space group) can define the octahedral rotation patterns of bulk SRO. For bulk, the tilting angle is defined as $(180° - \phi)/2$, where ϕ represents Ru-O-Ru bond angle along the longer orthorhombic-cell *c*-axis. The SRO holds a Ru-

O-Ru bond angle of 163°, which corresponds to a tilt angle of 8.5°, while averaged rotation angle is ~5°. It should be emphasized that if we increase the temperature to 550°, then the octahedral RuO_6 distortion decreases, leading to a tetragonal structure, where now the octahedra rotate only about [001] as described by $a^0\ a^0\ c^-$. Additionally, at 680°, the remaining octahedral rotations completely vanish, leading to an ideal cubic perovskite [11,12].

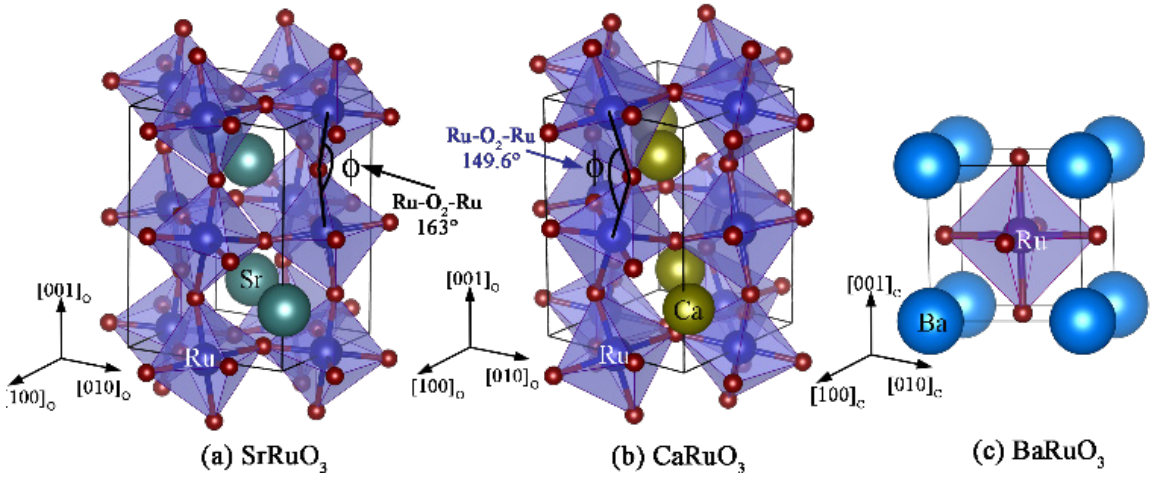

Figure 1.7. Crystal structure of (a) $SrRuO_3$, (b) $CaRuO_3$, and (c) $BaRuO_3$.

In discussing the electronic structure, we start with a localized *d*-electron picture, where SRO possess Ru^{4+} ions. The five degenerate *d* orbitals undergo octahedral ligand field splitting as the Ru-4*d* states split into three-fold degenerate t_{2g} manifolds (lowered energy) and two-fold degenerate e_g manifolds (higher energy). In presence of a crystal field, the t_{2g} state is lower than the e_g, leading to a low spin configuration having ($4d^4$: $t_{2g}^{3\uparrow,1\downarrow}\ e_g^0; S = 1$). The energy gap between t_{2g} and e_g is approximately ~3-4 eV, thereby a large crystal field energy stops e_g from occupancy. This, seems reasonable, since low spin magnetization outcomes in 2 μ_B per Ru. However, the experimental magnetic moment is ~1.6 μ_B/Ru [12]. The decreased magnetic moment is attributed to the extremely stretched Ru 4*d* orbitals, leading to substantial O (2*p*)-Ru (4*d*) hybridization. The hybridization of Ru(4*d*)-O(2*p*) is corroborated as approximately ~70% of

net ordered moments originate from the Ru-site and rest from O site [13–15].

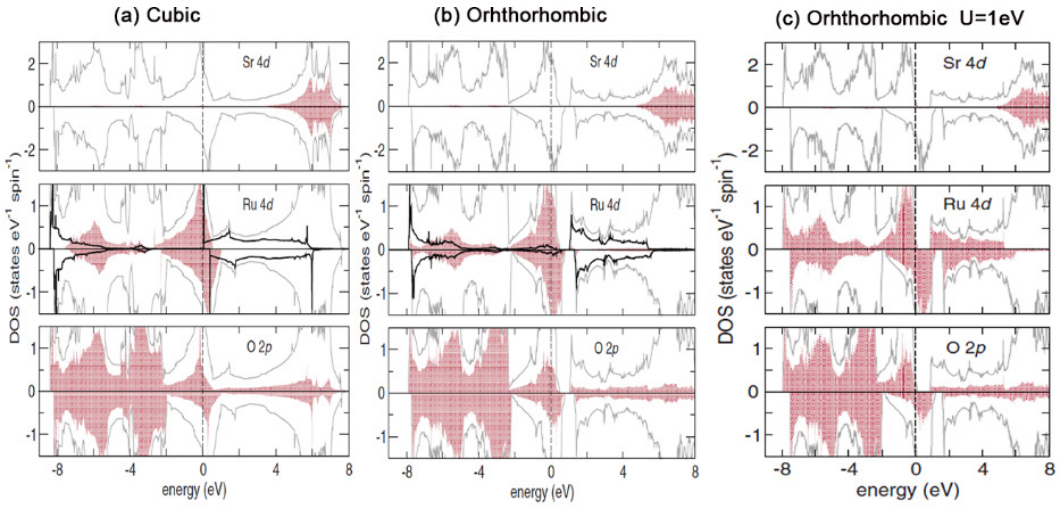

Figure 1.8. The total (gray line) and partial (shaded) spin-resolved densities of states for cubic SRO. (a) Cubic and (b) Orthorhombic, and (d) (c) orthorhombic SRO calculate with U=1eV. Sr 4*d* states (top), Ru 4*d* states (middle) [t_{2g} and e_g (unshaded bold line) symmetries are represented], and O 2*p* states (lower). The dashed line at 0 eV denotes the Fermi level (Reproduced from reference [13]).

The ground state of SRO is explained via the so-called Stoner criterion $U\ \mathrm{D}(\mathrm{E}_F) \geq 1$, where U is the intra-site Coulomb repulsion and $\mathrm{D}(\mathrm{E}_F)$ the Fermi-level density of states. In the Stoner framework, for SRO in an idealized cubic crystal structure, a van Hove singularity peak arises in the density of states exactly at the Fermi energy mainly from flat Ru 4*d* t_{2g} bands hybridized with O 2*p* states [Figure 1.8(a)]. While the e_g orbitals are formed at the lowest section of the valence/conduction bands [Figure 1.8(a)], and above the fermi energy at 5 eV, the Sr 4*d* states originate. Though, a structural distortion to its actual orthorhombic structure lifts the degeneracy from Ru 4*d* t_{2g} levels, consequently a small splitting of the van Hove peak. However, the $\mathrm{D}(\mathrm{E}_F)$ remains large [see Figure 1.9], thereby so called Stoner criterion: $\mathrm{U\ D}(\mathrm{E}_F) > 1$ is fulfilled [13,14].

The octahedral distortions result in a decrease in Ru 4*d*-O 2*p* overlap, but also narrows the bandwidths to some extent [Figure 1.8(b)]. The SRO, being the 4*d*-based transition metal

oxide is supposed to have an intermediate U and spin-orbit coupling in comparison to 3*d* and 5*d* counterparts, which display robust U and spin-orbit coupling. As per Rondinelli *et al*. [13], the Hubbard term $\mathrm{U} = 0.6$ eV best describes bulk SRO electronic structure. Though, if effective strength is $U = 1$ eV, the bands become narrow possessing energy gaps in both spin-up and spin-down channels. The presence of electronic correlations outcomes in a ~70% reduction in the total Fermi-level DOS in LSDA+U in comparison to LSDA. With LSDS+U, the Ru 4*d* states contribution is completely triggered by the minority spin electrons, and the system is almost half-metallic, though for U > 2 eV, majority-spin t_{2g} becomes insulating, while one-third filled minority t_{2g} is conducting, consequently SRO becomes a half-metal.

In the bulk perovskite oxide system, the oxygen octahedral environment is generally controlled via chemical substitution, hydrostatic pressure, and temperature. Yet, the challenge to engineer perovskite functionalities stimulates finding innovative synthesis routes to manipulate the crystal structure. Along this line, the artificial heterostructures approach provides additional freedom to engineer the octahedral unit and lattice structure [6–8]. The epitaxial strain engineering approach is extensively employed in SRO to manipulate the octahedral environment; however, the strain is a long-range effect, thereby atomic-scale control octahedral modification is difficult [4,5]. The epitaxial strain engineering studies have revealed that SRO film on $SrTiO_3$ (001) (compressive strain) shows a distorted orthorhombic unit cell (monoclinic), however on $DyScO_3$ (compressive strain, orthorhombic substrate) changes to tetragonal, respectively. Epitaxial strain engineering introduces freedom to manipulate the structural distortion due to elastic strain energy accommodation because of structural mismatch between film and substrate. It is widely supposed that strain-induced octahedral modifications are the cause of emergent properties arising in the heterostructures.

Recently, innovative studies have shown that via a so-called interfacial octahedral

coupling effect, where due to the preservation of octahedral corner-connectivity at the hetero-interface, the octahedral tilts from the substrate or buffer layer could be transported into the film [6–8]. The studies have revealed that a capping layer modifies the octahedral rotation of SRO, leading to T_c enhancement [16]. Likewise, via a buffer layer, the magnetic functionality of SRO could be tuned due to the modified Ru-O-Ru angle [6]. Therefore, the heterostructure engineering approach enforces the octahedra to distort (B-O bond length), and modify rotation/tilt patterns (B-O-B bond angle), while maintaining corner connectivity at or near the substrate-film heterojunction, thereby offering the opportunity to tune the octahedral behavior and achieve new functionalities. The aforementioned methods are though efficacious for Ru-O-Ru bond angle and crystal symmetry modification, yet the understanding of octahedral geometry and its relation to ruthenates electronic and magnetic properties is far from clear.

1.4.2 Calcium Ruthenate

The $CaRuO_3$ (CRO) is iso-structural (orthorhombic), iso-valent, and iso-electronic with SRO, however, CRO does not display ferromagnetism, rather it is paramagnetic metal [17]. Structurally speaking, CRO has orthorhombic symmetry having a = 5.36 Å, b = 5.54 Å, c = 7.68 Å, and a_{pc} = 3.84 Å, with octahedral-rotation pattern $a^+b^-c^-$ (*Pbnm* space group). As per the phase diagram, CRO resides close to the quantum critical region [18]. Given its proximity to the magnetic quantum critical point [19], CRO is contended to possess ferromagnetism by means such as chemical doping [20–22], disorder/defects [23], and epitaxial strain [24–26]. These findings suggest that ferromagnetic behavior in CRO is non-intrinsic.

Although, both CRO and SRO are orthorhombic, yet different sized ion (Sr, Ca being smaller) placement results in distinct Ru-O-Ru angles of SRO (163°) and CRO (148°). The contrasting magnetic ground state of SRO and CRO are considered to root in their different structural distortion. The significant difference in Ru-O-Ru bond angle of SRO (163°) and CRO

(148°) can have drastic effects on the Fermi-level DOS. The electronic band structure calculation of CRO establishes that the splitting of the van Hove peak in $D(E_F)$ is comparatively large [see Figure 1.9], leading to a smaller $D(E_F)$, even though total t_{2g} band width is smaller [13,14]. Furthermore, the peaked density of state location is below the Fermi energy, consequently, the Stoner criterion is no longer met.

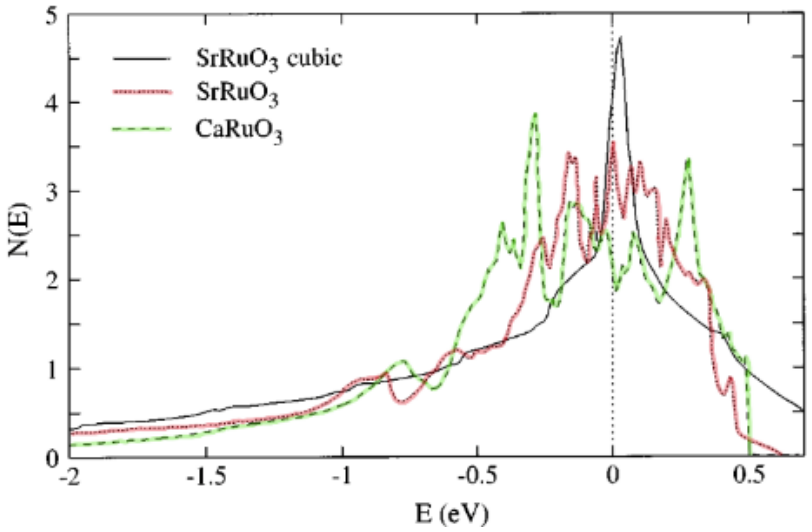

Figure 1.9. Densities of states in the t_{2g} band for $SrRuO_3$ in the cubic and orthorhombic structure, and of $CaRuO_3$ (adapted from reference [14]).

As per Mukuda *et al*. [27], a Stoner factor of 0.98 is found for CRO, implying its nearly ferromagnetic. Furthermore, it is worth noting that the t_{2g} band width of CRO is nearly 10% smaller (total band width of ~2.4 eV with d_{xy}, d_{yz}, d_{xz} band width ranging between ~2.3-2.4 eV) as compare to SRO (total band width of ~3 eV with d_{xy}, d_{yz}, d_{xz} having similar band width ~2.7 eV) [28]. Qualitatively, the bandwidth is defined as $W \propto \frac{\cos\Phi}{\zeta^{3.5}}$, where $\Phi = \frac{\pi-\theta}{2}$ is a deviation from ideal B-O-B angle i.e., $\theta = 180°$ and ζ is B-O bond length. Therefore, a larger deviation in CRO from 180° in comparison to SRO should lead to reduced bandwidth. Moreover, Ru-O-Ru angle also impacts the electron hopping ($t \propto w$), since it is maximized for 180° and decreases otherwise. Moreover, the electron correlation strength given as the ratio U/W , where U is

Coulomb repulsion is expected to be larger for CRO, making CRO more correlated.

In $Sr_{1-x}Ca_xRuO_3$, the ferromagnetic interaction gradually diminishes with increasing x [Figure 1.10]. The suppression of ferromagnetism as per Jin *et al.* [29] is associated so-called Griffith phase (GP) as evidenced by anomalous behavior in magnetic susceptibility. Since the nominal electron counting is not changing, the evolution of the structure or bonding nature of dopants appears to be the primary cause. Therefore, accurate determination of bond geometry is vital. Therefore, the robust coupling among crystal structure and physical properties stresses on the ability to control the octahedral distortions to enhance material functionalities and address the role of structure in the spin configuration in ruthenates.

1.4.3 Barium Ruthenate

In the band magnetism picture $\left(W \propto \frac{\cos\Phi}{\zeta^{3.5}}\right)$ for a cubic symmetry because of enlarged $D(E_F)$ existing exactly at the Fermi level, a maximized T_c is anticipated. Though, the validity of this model is controversial for the ruthenates. As reported by Jin *et al*. [29] placement of larger Ba atom at A-site though increases the structural symmetry to idealized cubic structure: $BaRuO_3$ (Ru-O-Ru =180°), yet BRO is ferromagnetic metal having a lowered T_C = 60 K [see Figure 1.10]. It is worth noting the BRO T_C is much smaller than SRO counterpart (T_C ~ 160 K). Moreover, the hypothesis that high distortion triggers smaller bandwidth, thereby favoring bad electron itinerant nature (enlarged electrical resistivity; ρ) and vanishing ferromagnetism is neither applicable to electrical resistivity (ρ), since SRO has smallest ρ than BRO. From the series of $Sr_{1-x}Ba_xRuO_3$ [right side of Figure 1.10] and $Sr_{1-x}Ca_xRuO_3$ [left side Figure 1.10], the reduction of T_c is very obvious, though the decrease is caused by different mechanisms.

In the series of $Sr_{1-x}Ba_xRuO_3$, a typical Curie-Weiss behavior is maintained $T > T_c$ [see inset of Figure 1.10]. In ruthenates, there exists a strong competition between the A-O and B-O bonds for the O-2p electron, whereas the electronegativity reduces: Ca > Sr > Ba. It is

conjectured that due Ba-cation stronger ionic character, the Ba-O bond does not compete very strongly for the shared O-2p electron, hence strengthening the Ru-O bond and broadens the bandwidth, which reduces the ferromagnetic transition temperature. The underlying results imply that a comprehensive understanding of electro-magnetic functionalities coupling to crystal structure in ruthenates remains incomplete due to convoluted twinning of octahedral tilt (Ru-O-Ru angle), A-O and Ru-O bond-length variation, and covalency (A-O and Ru-O).

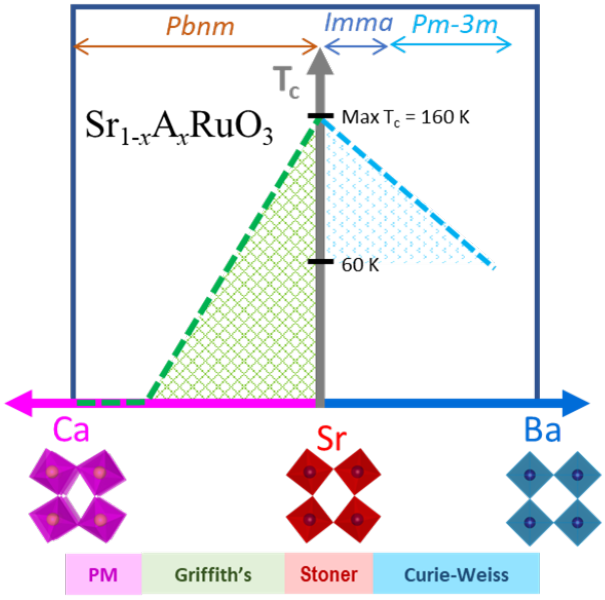

Figure 1.10. Phase drawing of the transition temperatures for bulk $Sr_{1-x}A_xRuO_3$ (A = Ca or Ba). The green shaded area represents the characteristic of Griffiths' phase.

1.5 Dissertation Organization

Chapter 1 provides a brief introduction to perovskite oxides and manipulation of perovskite functionalities by employing thin-film epitaxy. The thin film engineering routes for example; epitaxial strain engineering, and interfacial octahedral coupling are presented. This chapter also describes the research motivation and a summary of the materials used in the project.

Chapter 2 is devoted to the theoretical background of magnetism to deliver essential contextual information and conceptual understanding.

Chapter 3 provides a detailed overview of the experimental techniques employed in this work. This chapter is divided into the following: perovskites film growth kinetics, structural, magnetic, and electron-transport characterization.

Chapter 4 focuses on ultra-thin complex-metal oxide $SrRuO_3$ confined in heterostructure form between $SrTiO_3$ (STO) i.e., STO^5-SRO^n-STO^5 with n = 1- and 2-unit cells, and the corresponding impact on electro-magnetic properties. I found that with heterostructure engineering, the electric and magnetic properties of monolayer $SrRuO_3$ are profoundly affected by interfacial-intermixture. The results highlight the role of B-site non-stoichiometry and interface-induced intermixture in determining the electro-magnetic functionalities of spatially confined materials.

Chapter 5 details the emergence of unusual, thickness-dependent electro-magnetic properties in ultrathin $CaRuO_3$ films by unique δ-doping heterostructure engineering i.e., insertion of a single isovalent SrO layer. It is revealed that pristine $CaRuO_3$ films while retaining non-magnetic character become insulting when confined to a thickness of ~15-unit cells (u.c.). However, the novel δ-doping induces an insulator-to-metal transition and unusual ferromagnetism. The results highlight the delicate nature of magnetic ordering in $CaRuO_3$ and the subtle effects that can alter it, especially the role of A-site cation in electronic and magnetic structure in addition to lattice distortion in ruthenates.

Chapter 6 focuses exploitation of epitaxial strain engineering to stabilize a robust cubic-ferromagnetic perovskites system in $SrRuO_3$. We show that using strain stabilized Ba implantation in $SrRuO_3$, the crystal symmetry could be continuously transmuted from bulk-like orthorhombic to cubic-like phase. The cubical perovskite epitaxial film exhibits robust ferromagnetic ordering (T_c = 145 K) with a strong perpendicular magnetic anisotropy. The present observations advocate prospect of octahedral engineering in emergent functionalities .

Chapter 2. Magnetism Overview

This chapter is focused on a detailed conceptual background theory of magnetism.

2.1 Magnetic Orders

A magnetic material comprises larger number of atoms with magnetic moments. Hence, the total magnetic moment in a volume of material is the summation of all magnetic moments within the associated volume, The average magnetic moment of electrons is usually described by the magnetization density

$$M = \sum \frac{m}{V} \qquad 2.1$$

Here, V is material volume. In free space there is no magnetization. Hence $\mathbf{B} = \mu_0 \mathbf{H}$, where μ_0 is free space permeability. Moreover, considering that an external magnetic field $\boldsymbol{H}$ interacts with materials, thus, in special case (linear media) the relationship between the induced magnetization **M** and the applied field is:

$$\mathbf{M} = \chi \mathbf{H} \qquad 2.2$$

Where, χ is magnetic susceptibility (dimensionless) of the material. Moreover, it is useful to define the material permeability, μ, degree to which a material magnetic flux density **B** responds to a magnetic field **H**. Hence, $\mathbf{B} = \mu \mathbf{H}$, and thus, $\mathbf{B} = \mu_0(\mathbf{H} + \mathbf{M})$, where μ_0 free space permeability, a large susceptibility. Hence, we have, $\mu = \mu_0(\chi + \mathbf{1})$. Materials with $\chi > 0$ are called paramagnetic and $\chi < 0$ are diamagnetic. Materials with a spontaneous magnetization (possessing magnetization even without application of a magnetic field) generally have much larger χ and could be ferromagnetic, antiferromagnetic or ferrimagnetic.

2.1.1 Diamagnetism

Diamagnetism is a magnetic phenomenon that is exhibited by all materials holding a weak and negative $\chi < 0$ magnetic susceptibility [30,31]. In most materials, electrons are paired

in the orbitals, and whenever, two electrons are paired together in the same orbital (one spin up +1/2 and the other being spin down -1/2) usually have their spin and orbital moments oriented such that the atom as a whole null net magnetic moment. A diamagnetic substance, even though comprises atoms having a null net magnetic moment, reacts in a specific mode to an external field. Under an external magnetic field the orbital motion of electrons (precession) changes (affecting the angular momentum **L**), and induces an opposite magnetic moment because of back electromotive force (lens law) [32]. Diamagnetism does not display any temperature dependence and hence is not affected by thermal fluctuations present in the material. Generally, a linear and negative magnetization with magnetic field is expected. However, magnetization and susceptibility versus temperature show a constant behavior.

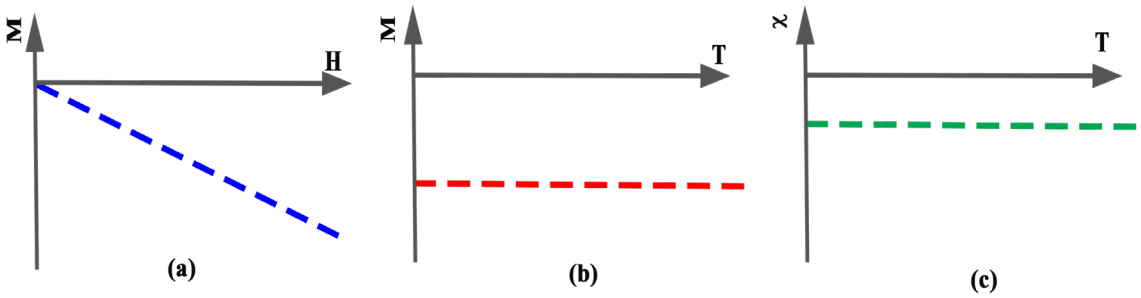

Figure 2.1. For diamagnetic material: (a) Magnetization as a function of field, (b) Magnetization versus temperature, and (c) Magnetic susceptibility against temperature.

2.1.2 Paramagnetism

Paramagnetism arises from a material holding an atom with at least one unpaired electron or if the atomic orbitals are incompletely occupied. In Paramagnetic materials, the atoms or molecules have net orbital or spin magnetic moments which tend to align parallel to the applied field, hence having $\chi > 0$. Paramagnetism results from the presence of at least one unpaired electron spin in a material's atoms or molecules. In valance shells, whenever an atom has free and unpaired electrons, a non-zero net magnetic moment exists. In this scenario, individual atom holds a net magnetic moment, though, the magnetic moments cannot couple together, because of

the thermal fluctuations k_BT (k_B is Boltzmann constant and T is the temperature) in the material predominantly break any coupling between dipoles, because the moments are very weak. Hence, the moments could be assumed independent and point in random directions. However, an external magnetic field aligns the moments parallel to the field [see Figure 2.2(a)] and at high fields, the magnetization might achieve its saturation. The degree of aligning and hence induced magnetization is dependent on applied field strength. Though upon removal of external field, the spins attain randomized alignment. Moreover, for a certain value of the applied magnetic field, and decreasing temperature, magnetic moments alignment is stimulated, resulting in amplification of the magnetization and, at 0 K, the magnetization achieves its maximum value as in Figure 2.2(b).

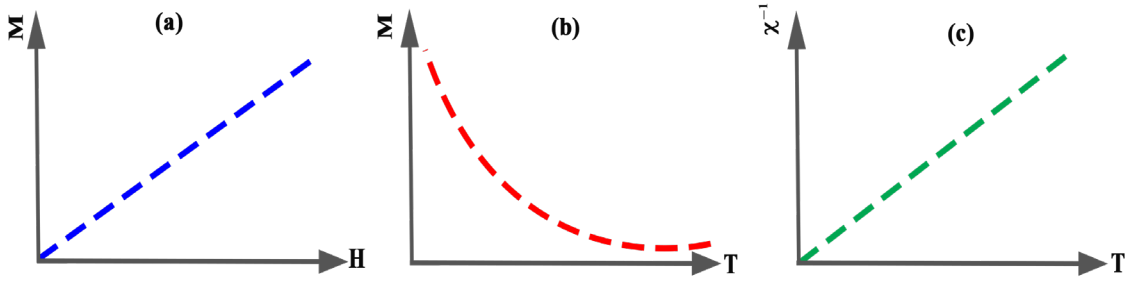

Figure 2.2. (a) Magnetization versus the field, (b) Magnetization against temperature, and (c) inverse magnetic susceptibility versus temperature for paramagnetic materials.

2.1.3 Ferromagnetism

Ferromagnetism is the phenomenon of spontaneous magnetization and belongs to cooperatively ordered systems. Normally ferromagnetism is characterized by two parameters: (1) Curie temperature T_c, below which material possesses spontaneous magnetizations (finite magnetization even for zero applied magnetic field). Whereas, above T_c material behaves like paramagnetic and the magnetization vanishes when the field is removed (zero magnetization for a zero-value magnetic field) as in Figure 2.3(b). (2) Saturation magnetization M_s measures the sum of all of the parallel magnetic moments. Additionally, unlike a paramagnetic system whose

susceptibility diverges only at absolute zero, the susceptibility of a ferromagnetic system diverges at the finite T_c. Moreover, concerning the magnetization versus magnetic field (below T_c), the system has a spontaneous magnetization, which implies that magnetization is non-zero. A comprehensive understanding of ferromagnetism could be collected from the magnetic hysteresis loop. In the hysteresis the magnetization is plotted verses increasing/decreasing fields as shown in Figure 2.3(a). The maximum possible magnetization state is *saturation magnetization* (M_S). Another parameter is the *coercivity* (H_c), which is the magnetic field strength desired to demolish system's magnetization state back to zero.

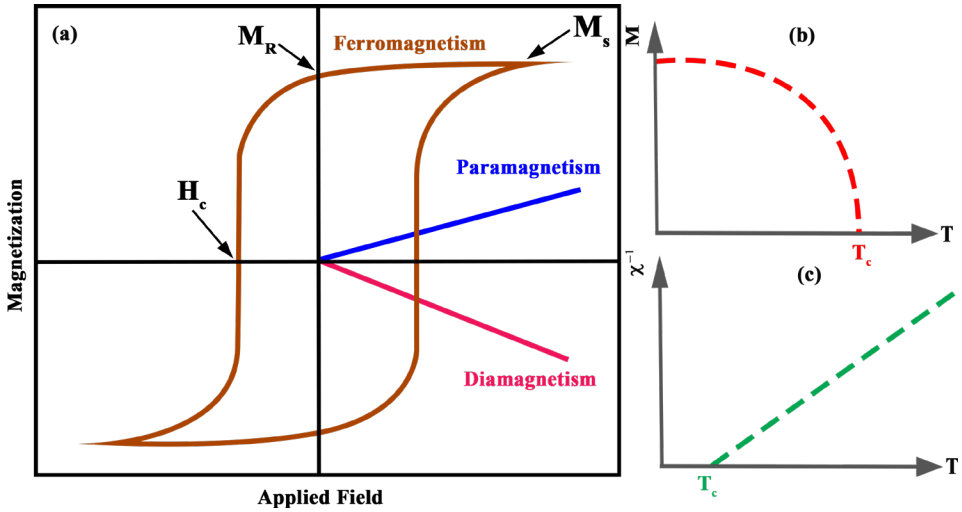

Figure 2.3. Characteristic of ferromagnetic materials: (a) Magnetization against field, (b) Magnetization function of temperature, and (c) inverse magnetic susceptibility with temperature.

2.1.4 Antiferromagnetism

Antiferromagnetic systems are analogous to ferromagnetics since individual localized region holds a non-zero moment. Though, for Antiferromagnetism, the adjacent moments align antiparallel (on different sublattices), leading to zero magnetization. Generally, antiferromagnetic order could occur at a characteristic temperature, termed as Neel temperature (T_N).

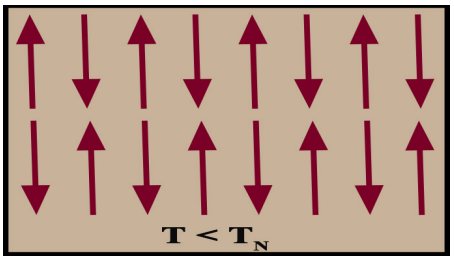

Figure 2.4. Schematics of Antiferromagnetism.

2.1.5 Ferrimagnetism

Ferrimagnetism is an exclusive kind of antiferromagnets. In ferrimagnetic systems, much like antiferromagnets, below T_N, nearest neighboring magnetic moments are aligned antiparallel to each other, though due to different sublattices sizes, the magnetic moments will not be equal as shown in Figure 2.5. As a result, the magnetization will not cancel out.

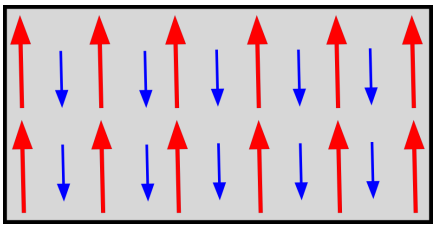

Figure 2.5. Depiction of ferrimagnetism.

2.2 Magnetic Interactions

In this section, different types of magnetic interaction will be explained. The occurrence of magnetic ordering demands that there should exist some coupling among the localized or delocalized moments which should lead to different magnetic orders.

2.2.1 Dipole-Dipole Interactions

Magnetic dipole-dipole interaction, also named dipolar coupling, refers to the interaction among two magnetic-dipoles. From electromagnetism, the magnetic field of a dipole is:

$$\mathbf{B}_{\text{dipole}}(\mathbf{r}) = \frac{\mu_0}{4\pi}\frac{1}{\mathbf{r}^3}[3(\mathbf{m}.\hat{\mathbf{r}})\hat{\mathbf{r}} - \mathbf{m}] \qquad 2.3$$

Whereas, the energy of a magnetic dipole in a magnetic field is $U = -\boldsymbol{m}.\boldsymbol{B}$, hence

interaction energy of two magnetic dipoles $\boldsymbol{m}_1$ and $\boldsymbol{m}_2$ separated by $\boldsymbol{r}$ is given by:

$$\mathrm{U} = \frac{\mu_0}{4\pi}\frac{1}{\boldsymbol{r}^3}[\boldsymbol{m}_1.\boldsymbol{m}_2 - 3(\boldsymbol{m}_1.\hat{\boldsymbol{r}})(\boldsymbol{m}_2.\hat{\boldsymbol{r}})] \tag{2.4}$$

In general, the interaction strength depends on magnetic moments relative orientation, distance between interacting dipoles, and magnitudes of individual interacting dipoles. For approximation, assuming $m_1 = m_2 = \boldsymbol{\mu_B}$ and $r = 1$ Å gives $\approx 10^{-23}\,J$ or 0.1 meV [31]. This energy is insignificant compared to energy at room temperature. Numerous systems achieve magnetic ordering (even around 1000 K), this implies that dipolar interactions are weak and cannot lead to magnetic ordering for most materials.

2.2.2 Exchange Interactions

In a material, each atom interacts with neighboring atoms, where, the underlying interactions are not only magnetic dipole-dipole interaction. Generally, dipole-dipole are normally very tiny, and hence not sufficient enough to cause magnetic ordering. To achieve the high internal fields, an electrostatic interaction must be introduced, where such an interaction arises through exchange effects. These interactions are termed *exchange interactions*. The exchange was initially presented in the interpretation of helium atom (Z=2). The Hamiltonian for He atom is

$$\mathrm{H} = \left(-\frac{\hbar^2}{2m}\nabla_1^2 - \frac{1}{4\pi\varepsilon_0}\frac{Ze^2}{|r_1|}\right) + \left(-\frac{\hbar^2}{2m}\nabla_2^2 - \frac{1}{4\pi\varepsilon_0}\frac{Ze^2}{|r_2|}\right) + \frac{1}{4\pi\varepsilon_0}\frac{e^2}{|r_1 - r_2|} \tag{2.5}$$

$$\mathrm{H} = \mathrm{H}_0(1) + \mathrm{H}_0(2) + \mathrm{H}_{e-e} \tag{2.6}$$

Here, one for electron 1 and two for electron 2. The last term is written for the electrostatic interaction between the two electrons. Therefore, we have

$$\mathrm{H}_0(1) = \left(-\frac{\hbar^2}{2m}\nabla_1^2 - \frac{1}{4\pi\varepsilon_0}\frac{Ze^2}{|r_1|}\right) \tag{2.7}$$

$$\mathrm{H}_0(1) = \left(-\frac{\hbar^2}{2m}\nabla_2^2 - \frac{1}{4\pi\varepsilon_0}\frac{Ze^2}{|r_2|}\right) \quad 2.8$$

$$\mathrm{H}_{e-e} = \frac{1}{4\pi\varepsilon_0}\frac{e^2}{|r_1 - r_2|} \quad 2.9$$

If the electrostatic term is neglected, then $\mathrm{H} = \mathrm{H}_0(1) + \mathrm{H}_0(2) = \mathrm{H}_0$ where this is the sum of two hydrogen atom Hamiltonians. As electronic interactions are ignored, therefore, the Schrodinger equation for a single electron is

$$\left(-\frac{\hbar^2}{2m}\nabla_1^2 - \frac{1}{4\pi\varepsilon_0}\frac{Ze^2}{|r_1|}\right)\psi_{nlm}(r_1) = E\,\psi_{nlm}(r_1) \quad 2.10$$

Since it is like a hydrogen atom (here Z=2), the wavefunction solution for the ground state is

$$\psi_{100}(r_1) = \frac{\sqrt{Z^3}}{\sqrt{\pi a^3}}e^{-Zr_1/a} \quad 2.11$$

Here a is Bohr radius. Similarly, for the 2nd electron, we have

$$\psi_{100}(r_2) = \frac{\sqrt{Z^3}}{\sqrt{\pi a^3}}e^{-Zr_2/a} \quad 2.12$$

Now, $\mathrm{H}_0(1) + \mathrm{H}_0(2) = \mathrm{H}_0$, therefore we expect the solution of H_0 is of the form:

$$\psi(r_1, r_2) = \psi_{100}(r_1)\,\psi_{100}(r_2) \quad 2.13$$

Therefore, we get

$$\psi(r_1, r_2) = \frac{Z^3}{\pi a^3}e^{-Z(r_2+r_2)/a} \quad 2.14$$

Thus, the total wavefunction with both spatial and spin parts is

$$\psi(r_1, s_1; r_2, s_2) = \psi(r_1, r_2).\chi_{as}(s_1, s_2) = -\psi(r_2, s_2; r_1, s_1) \quad 2.15$$

This implies that under exchange the total wavefunction should be antisymmetric. Thus, we have two possibilities, which are:

$$\psi(r_1, s_1; r_2, s_2) = \begin{cases} \psi_{sym}(r_1, r_2\,).\,\chi_{as}(s_1, s_2) \\ or \\ \psi_{as}(r_1, r_2\,).\,\chi_{sym}(s_1, s_2) \end{cases} \quad 2.16$$

The spin state is either singlet or triplet. For a more general case, we can write the space part of the wave function for an electron in the ground state $n = 1, l = 0, m = 0$, and the other being in an excited state as labeled by n, l, m.

$$\psi^S(r_1, s_1; r_2, s_2) = \frac{1}{\sqrt{2}}\{\,\psi_{100}(r_1)\,\psi_{nlm}(r_2) + \,\psi_{100}(r_2)\,\psi_{nlm}(r_1)\}\,\chi_{as}(s_1, s_2) \quad 2.17$$

$$\psi^T(r_1, s_1; r_2, s_2) = \frac{1}{\sqrt{2}}\{\,\psi_{100}(r_1)\,\psi_{nlm}(r_2) - \psi_{100}(r_2)\,\psi_{nlm}(r_1)\}\chi_{sym}(s_1, s_2) \quad 2.18$$

Where, the labels denote; S = singlet and T = triplet. First, let's consider the ground state, where both electrons are in 1s orbital. In this scenario, electrons occupy the identical orbitals and can have quantum numbers: $n = 1, l = 0, m = 0$. Moreover, the spatial wave function must be symmetrical, and spin singlet is only permissible, thus we have

$$\psi_G^S(r_1, s_1; r_2, s_2) = \frac{1}{\sqrt{2}}\{\,\psi_{100}(r_1)\,\psi_{100}(r_2) + \,\psi_{100}(r_2)\,\psi_{100}(r_1)\}\,\chi_{as}(s_1, s_2) \quad 2.19$$

Here, S = singlet, and G represents ground state wavefunction. The solution to equation:

$$\mathrm{H}_0\psi_G^S(r_1, s_1; r_2, s_2) = E_0\psi_G^S(r_1, s_1; r_2, s_2) \quad 2.20$$

Here, we have:

$$\psi_G^S(r_1, s_1; r_2, s_2) = \frac{Z^3}{\pi a^3}e^{-Z(r_2+r_2)/a}\chi_{as}(s_1, s_2) \quad 2.21$$

Hence, one gets the ground state energy for 2 electrons;

$$E_0 = -2\frac{m}{2\hbar^2}\left(\frac{Ze^2}{4\pi\varepsilon_0}\right)^2 \quad 2.22$$

Since Bohr radius is: $a = \frac{4\pi\varepsilon_0\hbar^2}{me^2}$, and Z=2 we get:

$$E_0 = -\frac{4e^2}{4\pi\varepsilon_0 a} \quad 2.23$$

On calculation, we get $E_0 = -108\ eV$. The experimental ionization energy (energy

needed to remove an electron) is 24.63 eV. Thus, upon one electron removal, the energy of ionized He is $-Z^2.13.6 = -54.6\ eV$. Therefore, the ground state energy of Helium is $-54.6-24.63 = -79.03\ eV$. Thus, obtained energy is not close. However, by introducing the electronic repulsion, one can achieve a better approximation. Then, treating the e-e interaction as a perturbative term, we find:

$$E_1 = \langle \psi_G^S(r_1, s_1; r_2, s_2) | \mathrm{H}_{e-e} | \psi_G^S(r_1, s_1; r_2, s_2) \rangle \tag{2.24}$$

Upon calculation, one can neglect the spin wavefunction. In our calculation, the spin term is introduced through the prerequisite that the total wavefunction should be antisymmetric. Also realizing that wavefunction is real, one gets:

$$E_1 = \int dr_1\, dr_2 \left| \psi_G^S(r_1, s_1; r_2, s_2) \right|^2 \tag{2.25}$$

$$E_1 = \int d^3r_1\, d^3r_2 \frac{1}{4\pi\varepsilon_0} \frac{e^2}{|r_1 - r_2|} \left\{ \frac{Z^3}{\pi a^3} e^{-Z(r_2+r_2)/a} \right\}^2 \tag{2.26}$$

Thus, we get finally

$$E_1 = \frac{5e^2}{4(4\pi\varepsilon_0 a)} \tag{2.27}$$

Thus, to first order, the ground state is

$$E = -\frac{4e^2}{4\pi\varepsilon_0 a} + \frac{5e^2}{4(4\pi\varepsilon_0 a)} = -\frac{11e^2}{4(4\pi\varepsilon_0 a)} \tag{2.28}$$

Therefore, to get closer to the experimental value (79.01 eV), both H_0 and H_{e-e} have to be considered. Now assume that one of the electrons in the 1s orbital hence states $n = 1, l = 0, m = 0$, and the other in an excited state as labeled by n, l, m. Hence, the wave functions are

$$\psi^S(r_1, s_1; r_2, s_2) = \frac{1}{\sqrt{2}} \{ \psi_{100}(r_1)\, \psi_{nlm}(r_2) + \psi_{100}(r_2)\, \psi_{nlm}(r_1) \}\, \chi_{as}(s_1, s_2) \tag{2.29}$$

$$\psi^T(r_1, s_1; r_2, s_2) = \frac{1}{\sqrt{2}} \{ \psi_{100}(r_1)\, \psi_{nlm}(r_2) - \psi_{100}(r_2)\, \psi_{nlm}(r_1) \} \chi_{sym}(s_1, s_2) \tag{2.30}$$

Where, the labels denote; S = singlet and T = triplet. If we assess the Schrodinger

equation for the central potential $\mathrm{H}_0 = \mathrm{H}_0(1) + \mathrm{H}_0(2)$, we have same energy for both wavefunctions. So, we have to calculate

$$E^T = \langle \psi^S(r_1, s_1; r_2, s_2) | \mathrm{H}_0(1) + \mathrm{H}_0(2) + \mathrm{H}_{e-e} | \psi^S(r_1, s_1; r_2, s_2) \rangle \quad 2.31$$

$$E^T = \langle \psi^T(r_1, s_1; r_2, s_2) | \mathrm{H}_0(1) + \mathrm{H}_0(2) + \mathrm{H}_{e-e} | \psi^T(r_1, s_1; r_2, s_2) \rangle \quad 2.32$$

Here, the labels denote; S = singlet and T = triplet. Thus, we have:

$$E^{S,T} = \int d^3r_1\, d^3r_2 \left(\psi^*{}_{100}(r_1)\, \psi^*{}_{nlm}(r_2) \pm (1) \psi_{100}(r_1)\, \psi_{nlm}(r_2) \right) [\mathrm{H}_0(1) + \mathrm{H}_0(2) + \mathrm{H}_{e-e}] \left(\psi_{100}(r_1)\, \psi_{nlm}(r_2) \pm \psi_{100}(r_2)\, \psi_{nlm}(r_1) \right) \quad 2.33$$

Finally, we get the following

$$\begin{aligned} E^{S,T} = & \frac{1}{2} \int d^3r_1 \left(\psi^*{}_{100}(r_1) \mathrm{H}_0(1) \psi_{100}(r_1) \right) \\ & + \frac{1}{2} \int d^3r_2 \left(\psi^*{}_{nlm}(r_1) \mathrm{H}_0(1) \psi^*{}_{nlm}(r_1) \right) \\ & + \frac{1}{2} \int d^3r_2 \left(\psi^*{}_{100}(r_2) \mathrm{H}_0(2) \psi^*{}_{100}(r_2) \right) \\ & + \frac{1}{2} \int d^3r_2 \left(\psi^*{}_{nlm}(r_2) \mathrm{H}_0(2) \psi^*{}_{nlm}(r_2) \right) \\ & + \frac{1}{2} \int d^3r_1\, d^3r_2\, \psi^*{}_{100}(r_1)\, \psi^*{}_{nlm}(r_2) \mathrm{H}_{e-e} \psi_{100}(r_1)\, \psi_{nlm}(r_2) \\ & + \frac{1}{2} \int d^3r_1\, d^3r_2\, \psi^*{}_{nlm}(r_1)\, \psi^*{}_{100}(r_2) \mathrm{H}_{e-e} \psi_{nlm}(r_1)\, \psi_{100}(r_2) \\ & \pm \frac{1}{2} \int d^3r_1\, d^3r_2\, \psi^*{}_{100}(r_1)\, \psi^*{}_{nlm}(r_2) \mathrm{H}_{e-e} \psi_{nlm}(r_1)\, \psi_{100}(r_2) \\ & \pm \frac{1}{2} \int d^3r_1\, d^3r_2\, \psi^*{}_{nlm}(r_1)\, \psi^*{}_{100}(r_2) \mathrm{H}_{e-e} \psi_{100}(r_1)\, \psi_{nlm}(r_2) \end{aligned} \quad 2.34$$

Thus, via defining the following, we can write

$$E_{100} = \int d^3r_1\ \psi^*{}_{100}(r_1) \mathrm{H}_0(1) \psi_{100}(r_1) \quad 2.35$$

$$E_{nlm} = \int d^3r_2\, \psi^*{}_{100}(r_2)\mathrm{H}_0(2)\psi^*{}_{100}(r_2) \tag{2.36}$$

$$C = \int d^3r_1\, d^3r_2 \left|\psi_{100}(r_1)\right|^2 \mathrm{H}_{e-e} \left|\, \psi_{nlm}(r_2)\right|^2 \tag{2.37}$$

$$J = \int d^3r_1\, d^3r_2\, \psi^*{}_{100}(r_1)\, \psi^*{}_{nlm}(r_2)\mathrm{H}_{e-e}\psi_{100}(r_1)\, \psi_{nlm}(r_2) \tag{2.38}$$

The sign is + for the symmetric function (S = Singlet) and – is antisymmetric function (T = Triplet). Then, we have the:

$$E^S = E_{100} + E_{nlm} + C + J \tag{2.39}$$

$$E^T = E_{100} + E_{nlm} + C - J \tag{2.40}$$

Here, E_{100} and E_{nlm} are the energies of electrons 1 and 2, respectively. The Coulomb integral C signifies the electrostatic coulomb repulsion between two electrons and it has a positive sign. The quantity J signifies the energy produced by the exchange of electrons between two orbits and is termed as exchange integral. In the singlet state, the spatial function is symmetric and the electrons tend to get close to each other. Whereas in triplet state the spatial part is antisymmetric and electrons tend to evade each-other. Consequently, the electrostatic repulsion phenomenon is large in singlet state and it holds a higher energy. Now, the difference among two eigenvalues (singlet-triplet splitting) is

$$E_{Singlet} - E_{Triplet} = E^S - E^T = 2J \tag{2.41}$$

The exchange energy 2J is the singlet-triplet splitting. The exchange interaction arises from the Coulomb interaction between two electrons and the total antisymmetric wavefunction requirement (symmetrization postulate). The symmetrization postulate results in either parallel or antiparallel alignment depending on the sign of J. In case, when J is positive, the spins are aligned parallel, though J is negative for antiparallel spins.

2.2.3 Heisenberg Model of Exchange

Heisenberg employed the ideas of parallel/antiparallel spins arrangement to construct a Hamiltonian of form

$$\mathrm{H} = \mathrm{H}_0 + \mathrm{H}_C + \mathrm{H}_J \tag{2.42}$$

Here, $E_0 = E_{100} + E_{nlm}$ is the expectation value central field Hamiltonian H_0. The Coulomb energy C is the expectation value of H_C. The exchange energies $\pm J$ are expectation values of the exchange Hamiltonian H_J. Therefore, the spin-dependent model Hamiltonian could be written in a form

$$\mathbf{H_J} = A\,\boldsymbol{S_1}.\boldsymbol{S_2} \tag{2.43}$$

Here, A is a constant. Now, recall for a single spin-1/2 particle, we write:

$$S_z|s, m_s\rangle = m_s\hbar\,|s, m_s\rangle \tag{2.44}$$

$$S^2|s, m_s\rangle = \hbar^2\, s(s+1)\,|s, m_s\rangle \tag{2.45}$$

Here, $s = \frac{1}{2}$ and $m_s = \pm\frac{1}{2}$. Thus, the eigenvalues of S^2 and S_z are

$$S_z\left|\frac{1}{2}, \pm\frac{1}{2}\right\rangle = \pm\frac{\hbar}{2}\left|s, \pm\frac{1}{2}\right\rangle \tag{2.46}$$

$$S^2\left|\frac{1}{2}, \pm\frac{1}{2}\right\rangle = \frac{3}{4}\hbar^2\left|\frac{1}{2}, \pm\frac{1}{2}\right\rangle \tag{2.47}$$

We now consider the case in which our system features two spin one-half particles. The spins $s_1 = \frac{1}{2}$ and $s_2 = \frac{1}{2}$, and hence a total coupled spin is

$$S_{Total} = s_1 + s_2 \tag{2.48}$$

This implies that we have $S = 0, 1$. Additionally, we have

$$S_{Total}^2 = (s_1 + s_2).(s_1 + s_2) = s_1^2 + s_2^2 + 2s_1.s_2 \tag{2.49}$$

$$2s_1.s_2 = S_{Total}^2 - s_1^2 - s_2^2 \tag{2.50}$$

$$2s_1.s_2 = \hbar^2 S_{Total}(S_{Total}+1) - \hbar^2 s_1(s_1+1) - \hbar^2 s_2(s_2+1) \tag{2.51}$$

$$2s_1.s_2 = \hbar^2 S_{Total}(S_{Total}+1) - \hbar^2 \frac{1}{2}\left(\frac{1}{2}+1\right) - \hbar^2 \frac{1}{2}\left(\frac{1}{2}+1\right) \tag{2.52}$$

$$2s_1.s_2 = \hbar^2 S_{Total}(S_{Total}+1) - \frac{6}{4}\hbar^2 \tag{2.53}$$

Now, finally $S_{Total} = 0$ for singlet and $S_{Total} = 1$ for triplet, we get

$$s_1.s_2 = \begin{cases} -\frac{3}{4}\hbar^2 & Singlet \\ \frac{1}{4}\hbar^2 & Triplet \end{cases} \tag{2.54}$$

These are the eigenvalues of $\mathbf{H_J} = A\,\boldsymbol{S_1}.\boldsymbol{S_2}$. Therefore, we can write

$$E_{S,T} = \begin{cases} -\frac{3A\hbar^2}{4} & Singlet \\ \frac{A\hbar^2}{4} & Triplet \end{cases} \tag{2.55}$$

This leads to the implication that if we take a difference, we get

$$E_S - E_T = -\frac{3A\hbar^2}{4} - \frac{A\hbar^2}{4} = -A\hbar^2 \tag{2.56}$$

Initially, in the He atom calculation, we have the result

$$E_{Singlet} - E_{Triplet} = E^S - E^T = 2J \tag{2.57}$$

This implies that $A = -2J$. The $\hbar^2$ has been absorbed into the exchange constant $\boldsymbol{J}$ as it has energy-units. It is often expressed in Kelvins by dividing it by k_B.Therefore, the spin-dependent part effective Hamiltonian is

$$\mathbf{H_J} = -2J\,\boldsymbol{S_1}.\boldsymbol{S_2} \tag{2.58}$$

For $J > 0$, the triplet state is favored $E_{Singlet} > E_{Triplet}$ (Ferromagnetism, which aligns the two spins parallel). On other hand, for $J < 0$, then $E_{Singlet} < E_{Triplet}$, hence singlet state

(S=0) is preferred (Anti-Ferromagnetism, tends to align the two spins antiparallel). The two-spin Hamiltonian could be generalized for a many-electrons by summing over all pairs of atoms on lattice sites i, j

$$\widehat{\boldsymbol{H}}_{\boldsymbol{Spin}} = -2 \sum_{i>j} \boldsymbol{J_{ij}}\, \boldsymbol{S_i}.\boldsymbol{S_j} \qquad 2.59$$

Here, $i > j$ to prevent double counting. Moreover, $\boldsymbol{J_{ij}}$ is the exchange constant between i^{th} and j^{th} spins. Generally, it is possible to take $\boldsymbol{J_{ij}}$ equal to a single exchange constant $\boldsymbol{J}$ for nearest neighbor interactions, and zero otherwise.

2.3 Itinerant Magnetism

The Heisenberg model (1928) considers the presence of permanent localized magnetic moments, which due to either direct or indirect exchange interactions order cooperatively. However, this model is not appropriate for metallic systems such as Fe, Co, and Ni, where magnetic moments transpire due to the angular momentum of unpaired electrons in unfilled shells, which are relatively free to move through the material (itinerant electrons). Moreover, we know that spin and orbital moments are multiple of Bohr magneton $m = -\frac{\mu_B}{\hbar}[g_s \mathrm{S} + g_l \mathrm{L}]$. For Fe with six 3*d* and two 4*s* electrons, and according to Hund's rule, the 4 unpaired electrons give a spin magnetic moment of $m_s = 4\mu_B$. If the orbital moment is included one would estimate the moment to be $6\mu_B$. However, for Fe, if we experimentally measure the spontaneous magnetization $M_S(T = 0)$ and divides it by the number of atoms n , we get $m_{eff}\mu_B = \frac{M_S(T=0)}{n}$. The corresponding experimental effective moment is $2.216\ \mu_B$, implying that the atomic moment is a non-integral multiple of μ_B. The higher value of moment due to orbital moment inclusion in comparison to experimental value and only spin moment scenario overestimates the orbital moments. Henceforth, a different approach is necessary, as the underlying results could not be described via localized moments. The discrepancy in Bohr magnetons was resolved via the band

theory of magnetism.

2.3.1 Band Theory

We will start with the free electronic structure picture, where the atoms are positioned at large distances from each other. Consider two hydrogen atoms are well separated from each other, where each atom with an electron is in 1s ground state, where the wavefunctions of atom A is Ψ_A and of B is Ψ_B as in Figure 2.6(a). When the two atoms are brought in proximity to each other their atomic wavefunctions start to overlap leading to molecular orbitals. The resulting overlap outcomes in two new wavefunctions possessing different energies and henceforth changed quantum numbers. As the atomic orbitals are wavefunctions, they can either interfere constructively or destructively ($\Psi_A \pm \Psi_B$). The molecular orbital is the wavefunction of a molecule, similar to that of the atomic orbital, (electronic wave function in an atom). The molecular may expand over two or a large number of atoms. This is sometimes called the Linear Combination of Atomic Orbitals or Tight binding model.

In-phase addition (constructive interference) of the two atomic orbitals results in the formation of a bonding orbital $\Psi_{sy} = \Psi_A + \Psi_B$ (lower energy), thus strengthening wave intensity and enhancement of electron probability density [Figure 2.6(b)]. In $\Psi_A + \Psi_B$ the electron spends chunk of the time in the space among two nuclei, where it is under the influence of an attractive potential of both protons, which leads to the amplified binding energy. On other hand, the antibonding molecular orbital $\Psi_{as} = \Psi_A - \Psi_B$ (higher energy) is shaped by the summation of two atomic orbitals of opposite phases (destructive interference), leading to a reduction of wave intensity and hence causing the probability density to die out in the region between the nuclei [Figure 2.6(c)].

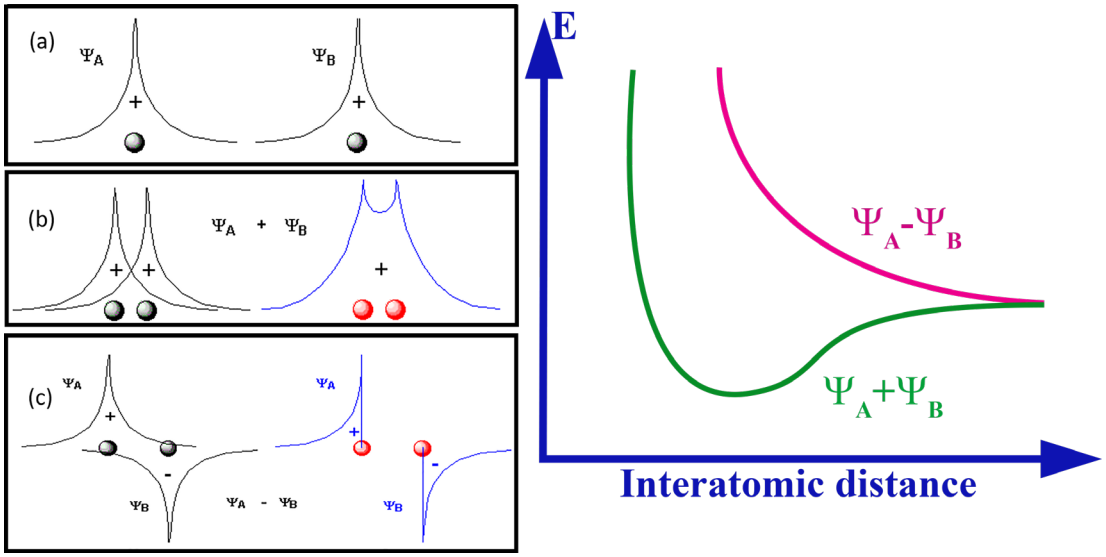

Figure 2.6. (a) Representation of two separated hydrogen atom wavefunctions of electrons. The wavefunction at closer separation is (b) bonding, (c) antibonding, and (d) Energy versus atomic separation.

When atoms come within proximity, the distinct atomic state may be divided into a sequence of closely spaced states. Hence, there exists a quasi-continuum of states among lowest and highest levels. This quasi quantum is called the energy band as shown in Figure 2.7. The energy band is half-filled as marked by dark green in Figure 2.7 and half-empty (marked by light green in Figure 2.7.). The degree of splitting rests on the interatomic separation and initiates with perturbation of the outermost electron shells as the atoms combine.

Let us now apply the concept to solid materials. Consider, that a large number of atoms, which are initially detached from one other are subsequently brought together to form the ordered atomic arrangement. For example, in two iron atoms, the 1s levels with each having two electrons well separated possess the same energy. However, when the atoms come close to each other, their electronic clouds start to overlap, and now the Pauli principle is applied to the two atoms. Hence, the Pauli principle stops two atoms from possessing a single 1s level comprising 4 electrons, rather, the 1s level has to splits into two levels, where each split level accommodates two electrons. Likewise, when N atoms are fetched close to each other, then individual level

splits into N levels. Thus, when free atoms are brought close together, the Coulomb interactions among atoms outcomes in energy splitting, distributing them into bands. It should be noted that each state of a free atom spreads into a band of energies. The bandwidth is proportional to the strength of the overlap interaction among neighboring atoms. Similarly, bands are formed from *p*, *d*, . . . states, however, the splitting degree is different.

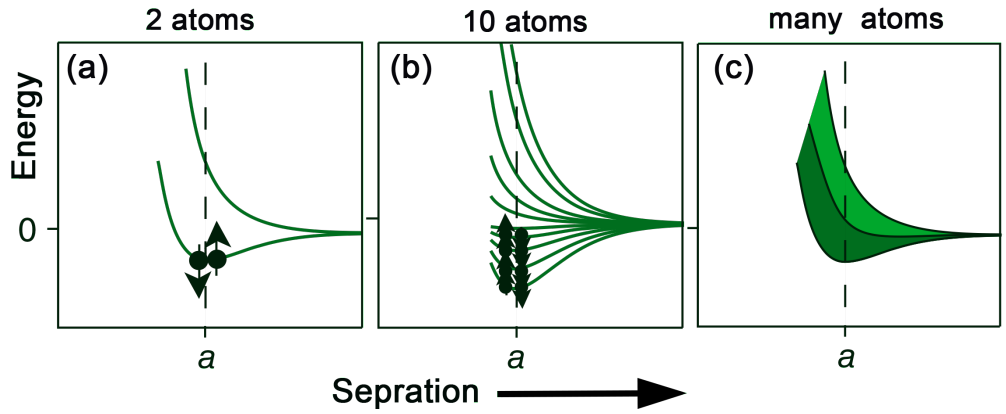

Figure 2.7. Energy levels as a function of distance for 1s levels for (a) 2 atoms, (b) 10 atoms, and (c) many atoms.

2.3.2 Pauli Paramagnetism

In addition to unpaired electrons in atoms, an important contribution to magnetism could be found from conduction electrons in metals. In metals, the conducting electrons are all delocalized, implying the model of the free electron gas is valid. For free electron gas in 3-dimensions energy levels are

$$\mathrm{E} = \frac{2\pi^2\hbar^2}{\mathrm{m_e L^2}}\left(\mathrm{n_x^2} + \mathrm{n_y^2} + \mathrm{n_z^2}\right) \qquad 2.60$$

Here, $k_x = \frac{2\pi}{\mathrm{L}} n_x \; ; k_y = \frac{2\pi}{\mathrm{L}} n_y ; k_z = \frac{2\pi}{\mathrm{L}} n_z$ and $n_x = n_y = n_z = 0, 1, 2, 3 \ldots\ldots$..Hence, the energy is quantized; only certain values are permitted. For finite sizes L, the energy levels are discrete. Conceptually, increasing the width of the potential well would cause the discrete points to move close together. Thus, for L = ∞, we have dispersion relation $E = \frac{\hbar^2 k^2}{2m_e}$ between energy

and wavenumber. For plane waves, it is a parabolic curve. The wavevector *k* is not restricted and goes from $-\infty$ to $+\infty$, then discrete points would form a band of energy levels. Thus, the electrons reside within a certain band of energies.

Now consider, that we want to accommodate N electrons at T = 0 K. As an electron could be either spin up ($\uparrow$) or spin down ($\downarrow$), therefore only two electrons can occupy each electron energy level – one spin-up electron and the other spin down, thereby having different spin quantum numbers, even though they have some energy. Thus, if we have N electrons, we can place two electrons in the lowest energy level, two electrons in the next lowest level, and stacking goes on until all the electrons have been accounted. The uppermost filled level is recognized as the *Fermi level.* The corresponding energy of the last filled (or half-filled) level at T = 0 K is called the Fermi energy E_F. Thus, E_F is the maximum energy of the topmost energy level. The situation is similar to a glass of water, where the water level corresponds to the Fermi level, and the total volume of water resembles electrons total. To find the total volume of water, we should find a glass cross-sectional area at each level. Corresponding to this quantity, we describe the density of states, D(E), the number of various electronic states at specific energy that electrons can dwell. In 3-dimensional electron gas

$$\mathrm{D(E)} = \frac{L^3}{2\pi^2}\left(\frac{2m_\mathrm{e}}{\hbar^2}\right)^{3/2} E^{1/2} \qquad 2.61$$

The density of states at the Fermi level $E = E_F$ is written as

$$\mathrm{D}(\mathrm{E}_F) = \frac{3}{2}\frac{N}{E_F} \qquad 2.62$$

We split the density of states D(E) of the electrons into two parts $\mathrm{D(E)} = \mathrm{D}_{\uparrow}(\mathrm{E}) + \mathrm{D}_{\downarrow}(\mathrm{E})$. In normal configuration both the densities of states are equal and equally occupied, hence $\mathrm{D}_{\uparrow}(\mathrm{E}) = \mathrm{D}_{\downarrow}(\mathrm{E}) = \frac{\mathrm{D(E)}}{2}$. This implies that the system has the similar number of spin-up electrons and spin-down electrons, and all the energy levels up to the Fermi energy are occupied

[Figure 2.8(a)]. Thereby the magnetization is zero as $M = \mu_B\{n_\uparrow(E) - n_\downarrow(E)\}$.

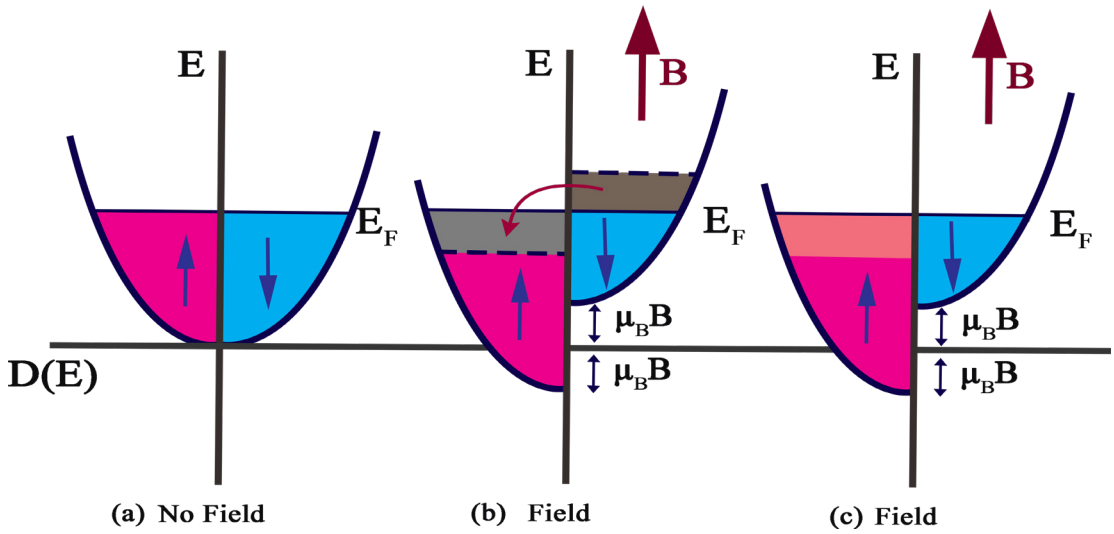

Figure 2.8. Pauli paramagnetism; (a) the model of spin-up/spin-down band in zero field (b) (b-c) Under application of magnetic field the spin-up and spin-down electrons undergo spin-splitting.

Now suppose, we apply a magnetic field **B** along z-direction $\boldsymbol{B} = B\hat{z}$. Consequently, both subbands change energy, where now potential energy of spin up (parallel to B) is $E_\uparrow = -\mu_B B$, and spin down (antiparallel to B) $E_\downarrow = +\mu_B B$. Hence, the energy difference is $2\mu_B B$. In other words, electrons with spin-up are lowered in energy, and thereby the effect is simply to move the spin-up electrons $D_\uparrow(E)$ relative to spin-down electrons $D_\downarrow(E)$ as in Figure 2.8(b).

Under the magnetic field, Fermi energy should be equal for both bands, this implies that from the spin-down band, some electrons are tossed into the spin-up band [Figure 2.8(b)]. Thus, the spin-up band is occupied by a larger number of electrons in comparison to the spin-down band as shown in Figure 2.8(c). As a result of the variance in the number of spin-up and spin-down electrons, the total magnetization is non-zero. For the gas of free electrons, Pauli derived the susceptibility:

$$\chi_{\text{Pauli}} = \mu_0 \mu_B^2 D(E_F) \qquad 2.63$$

The above result is the well-known Pauli paramagnetic susceptibility. When the magnetic

susceptibility is written as above, it depends directly on the density of state at the Fermi level. The larger the density of states, the higher the susceptibility and the magnetization under an external field. The above equation applies not only to free electrons but also to metals with arbitrary densities of states.

2.3.3 Magnetism of Transition Metals

For transition metals, the outermost electrons are 3*d* and 4*s*, and hence as the atoms are brought close to each other, the aforementioned electronic clouds will overlap and undergo splitting. If the interatomic distance *d* has decreased some distance d_0, the 3*d* levels form a band (B to C), while 4*s* levels form a relativity broader band (A to D) [Figure 2.9(a)]. The closing distance between atoms defines the overlap. At a similar spacing, the inner electrons (1*s* and 2*s*) are closer to the nucleus (distant from each other to have an impact on each other), thereby energy levels display insignificant splitting. However, if atoms are further fetched close to each other, (distances lesser than d_0), then 1*s* and 2*s* will undergo significant broadening. There exist numerous energy levels inside a band, for example, 1 mg of iron comprises of 10^{19} atoms and the Pauli principle necessitates those individual levels in the free atom must split into 10^{19} levels. This implies that a band level is closely spaced, thereby forming a quasi-continuum or energy band. An important aspect of the band theory is to compute energy bands shape, i.e., the shape of D(E) vs E. The DOS of 3*d* and 4*s* bands is shown in Figure 2.9(b). Since there are five-3*d* levels with room for 10 electrons, hence DOS of 3*d* levels is far bigger, whereas there is one 4*s* level with room for 2 electrons. The area under each D(E) vs E graph yields the total number of levels inside a band.

The 3*d* band can have 10 electrons per atom, and the level to which it is filled is shown by line Figure 2.9(b), where the topmost filled level is the Fermi level. Nickel has 10 (3*d* + 4*s*) electrons, however, the experiment designates that 9.4 belong to the 3*d* band, while the

remaining 0.6 to 4s. The Fermi level is therefore underneath the maximum of 3*d*. While, Copper possesses one additional electron, and hence its 3*d* is filled, whereas 4*s* is half full. The electrons belonging to the 4s band are expected not to influence magnetism. The 4*s* band density of states is low implying energy levels are widely spaced. The filled energy levels do not contribute to magnetism, since two electrons within each level possess opposite spins, leading to a null net moment.

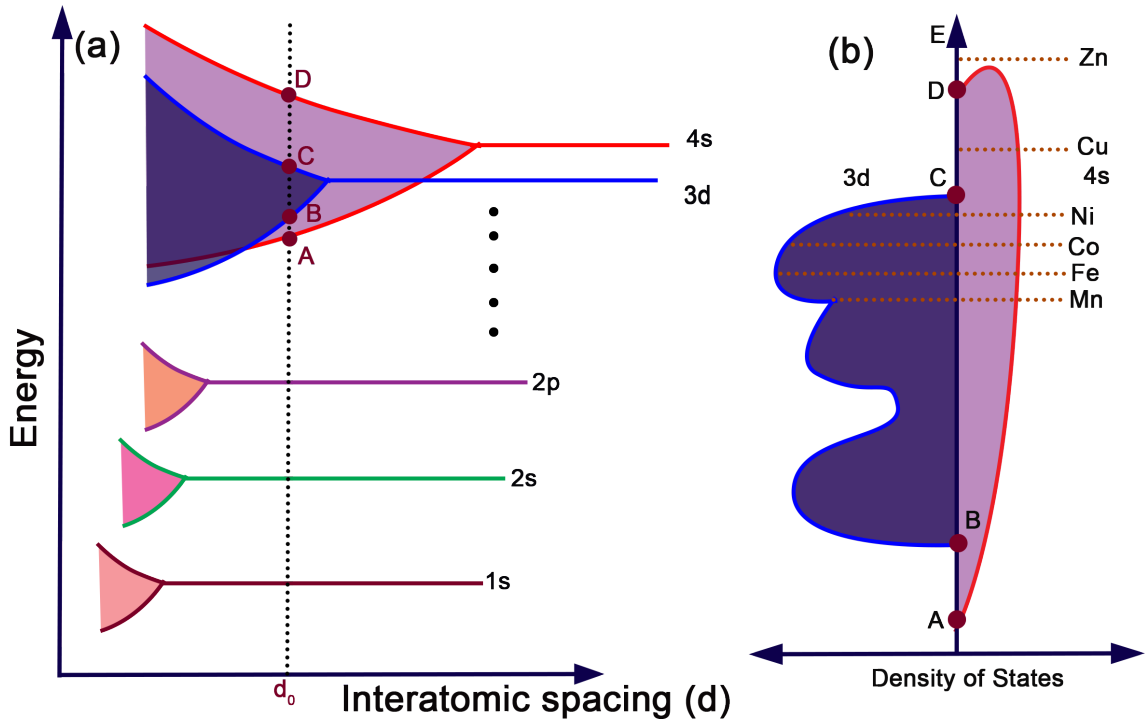

Figure 2.9. (a) Electronic energy levels splitting versus the inter-atomic separation, (b) Schematics of the density of states in 3*d* and 4*s* bands.

For effective number of Bohr magnetons, consider n = number of (3*d*+4*s*) electrons per atom, and x = number of 4*s* electrons per atom, then $n-x = 3d$ electrons per atom. At saturation magnetization, five 3*d* electrons will spin up and $n-x-5$ are spin down. Thus, the magnetic moment per atom is $m_{eff} = [5-(n-x-5)]\mu_B$, therefore one gets

$$m_{eff} = [10-(n-x)]\ \mu_B \qquad 2.64$$

This equation illustrates that the maximum spin unbalance is equivalent to the number of

unfilled electronic states. Now, for Ni with $n = 10$ and experimental $m_{eff} = 0.6\ \mu_B$, thus using these values in the above equation we get $x = 0.6$. This is proportional to the area bounded by the 4*s* N(E) curve underneath the fermi level as in Figure 2.9(b). This is the number of 4s electrons below Fermi level and hence implies that 9.4 electrons reside in the 3*d*, and 0.6 in the 4*s*. This almost explains ferromagnetic moment of Ni.

2.3.4 Hubbard Model

The Hubbard model is a model of interacting itinerant electrons. The so-called Hubbard Hamiltonian is beneficial for explaining the electronic nature of transition metal oxides. The Hamiltonian explains the Mott insulating state, but also successfully enlightens the presence of magnetic ordering in transition metals. For the explanation of Coulombic interactions, there is proposed Hubbard Hamiltonian

$$H = -t \sum_{<i,j>,\sigma} (C_{i,\sigma}^{\dagger} C_{j,\sigma} + C_{j,\sigma}^{\dagger} C_{i,\sigma}) + U \sum_{i=1}^{N} n_{i\uparrow} n_{i\downarrow} \qquad 2.65$$

$< \mathrm{i}, \mathrm{j} >$ is a summation over nearest-neighbor lattice sites and it emphasizes that hopping is only permitted between two adjacent lattice sites. $C_{i,\sigma}^{\dagger}$ and $C_{j,\sigma}$ are creation and annihilation operators of electrons having a spin σ on their respective site i, j. The number operator is $n_{i\sigma} = C_{i\sigma}^{\dagger} C_{i\sigma}$, and *U* is Coulomb interaction energy. *t* is hopping integral or transfer integral, where it suggests the kinetic energy of electron hopping between *i* and *j* sites (*t* is directly linked to orbital overlap and bandwidth W).

The first term of the above Hamiltonian explains the hopping scenario by the annihilation of a fermion with spin σ on-site i and formation of this fermion on a site j. The second term signifies the Coulomb repulsion between electrons, where on a single site, the interaction strength for two electrons is U.

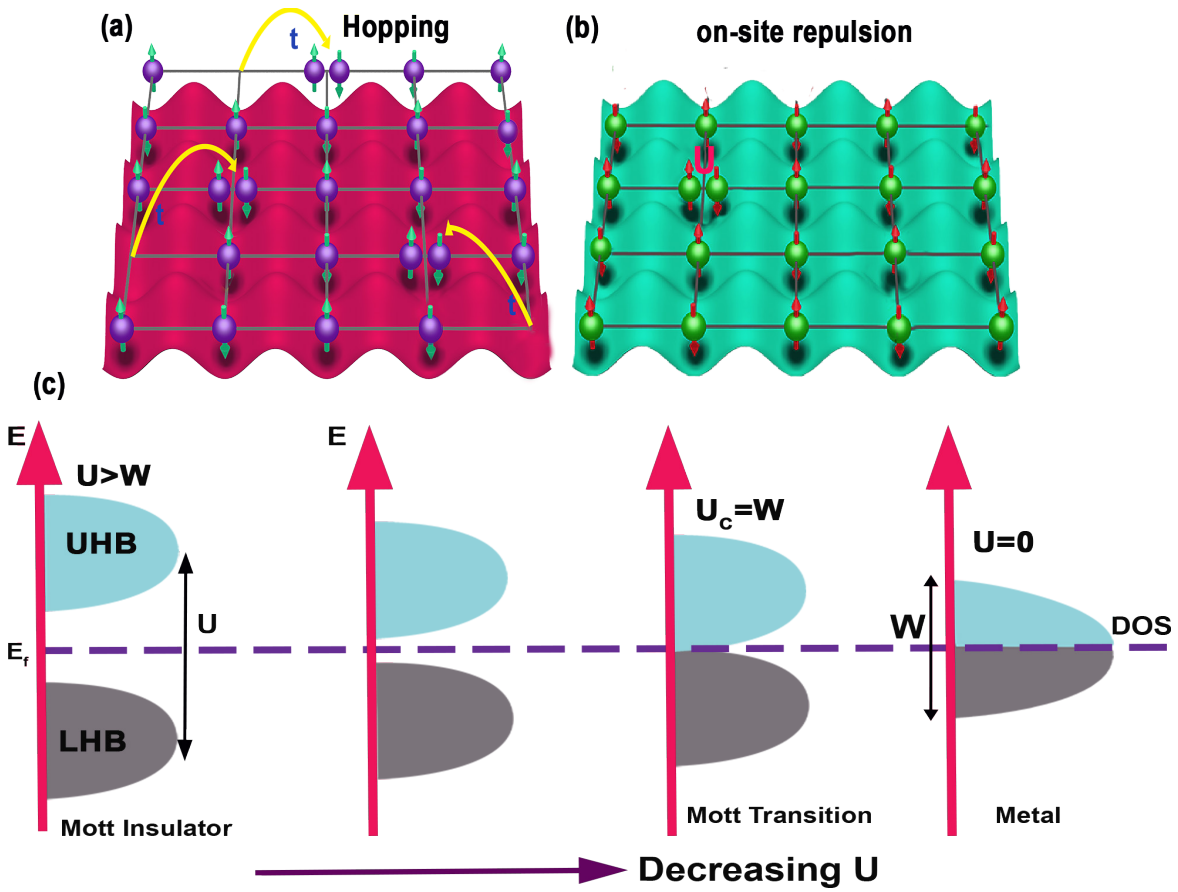

Figure 2.10. (a) Schematic illustration explaining (a) hopping of electron, and (b) on-site repulsion U. (c) Depiction of Mott Transitions by band-schematics.

When the e-e correlations are negligible, then $U = 0$ ($band\ width\ W \propto t\ = \infty$), the second term from Hamiltonian is neglected, thus yielding tight-binding Hamiltonian, where, the electrons will hop between the sites without any interruptions and the material will show a metallic behavior [33,34]. On other hand, the U tends to localize the electrons on sites. For $U\ > > t$, implying in presence of strong coulombic interactions, the half-filled band ruptures in two parts; Lower Hubbard Band (LHB) and Upper Hubbard Band (UHB) [34]. The LHB is filled and formed by the electrons that are dwelling in a vacant lattice site, and in contrast, an unfilled UHB is established by the electrons which are trying to reside in a site that has previously been booked by another electron.

Hence, an increase in Coulomb repulsion with respect to bandwidth W will outcome in

the rise of the bandgap between LHB and UHB. Hence, in the governance of strong e-e correlations $U >>> t$, the second term of Hamiltonian cannot be neglected, and electron localization dominates; leading to an insulating state, which is called *Mott insulator* [33,34]. However, if U decreases gradually then at some critical value of $U_c \sim W$ (finite U), the LHB and UHB meet each other (no band gap), where this transition at finite U_c is termed the Bandwidth-controlled metal to insulator transition. According to Mott, the condition for metal-insulator transition is $a_B n_c^{1/3} = 0.22$ where a_B is effective Bohr's radius of electrons and n_c is critical carrier density.

2.3.5 Stoner Model of Ferromagnetism

The Stoner model takes into consideration the valence band, where the density of states of the free electron is assumed to have two separates, and each band is populated by spin-up or spin-down electrons respectively i.e., $\mathrm{D(E)} = \mathrm{D}_{\uparrow}\mathrm{(E)} + \mathrm{D}_{\downarrow}\mathrm{(E)}$. To stabilize ferromagnetism, the spin-up and spin-down bands necessarily undergo splitting (ΔE). In other words, assume a slice of thickness ΔE from the spin-down side with energies from $E_F - \Delta E$ to E_F is transferred to the unoccupied spin-up states at energies $E_F + \Delta E$ from E_F. Hence, we are transferring $n_{\uparrow} - n_{\downarrow} = \frac{\mathrm{D}(\mathrm{E}_F)\,\Delta E}{2}$ electrons from one split band to the other, where $\mathrm{D}(\mathrm{E}_F)$ is Fermi-level density of states as shown in Figure 2.11. There is kinetic energy cost for the promotion of electronic state from one spin band to the other. The kinetic energy of system increases by

$$\mathrm{E}_K = \frac{1}{2}\int_0^{E_F+\Delta E} E\ D(\mathrm{E})\ dE + \frac{1}{2}\int_0^{E_F-\Delta E} E\ D(\mathrm{E})\ dE \qquad 2.66$$

Rearranging the integrals, we have

$$\mathrm{E}_K = \int_0^{E_F} E\ D(\mathrm{E})\ dE + \int_{E_F}^{E_F+\Delta E} E\ D(\mathrm{E})\ dE + \int_0^{E_F} E\ D(\mathrm{E})\ dE - \int_{E_F-\Delta E}^{E_F} E\ D(\mathrm{E})\ dE \qquad 2.67$$

Here, 1st and 3rd integral represent the kinetic energy when magnetization is zero $E_K|_{M=0}$. Moreover, when ΔE is small, then $D(E) = D(E_F)$. Thus, we have

$$E_K|_M = E_K|_{M=0} + \frac{1}{2}D(E_F)\,[(E_F + \Delta E)^2 - E_F^2] - \frac{1}{2}D(E_F)\,[E_F^2 - (E_F - \Delta E)^2] \qquad 2.68$$

Hence, finally, we have

$$E_K|_M = E_K|_{M=0} + D(E_F)(\Delta E)^2 \qquad 2.69$$

So, for the magnetized sample, the kinetic energy increases.

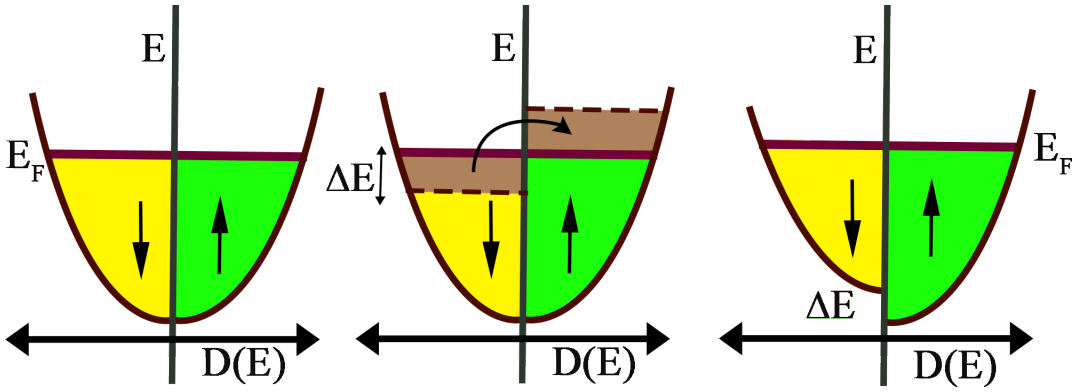

Figure 2.11. The schematic spin-split density of states with exchange splitting ΔE.

Therefore, for ferromagnetism to exist the electrons inside the band must have parallel spins, however as per the Pauli principle, the two electrons with identical spins cannot inhabit the identical electronic state (if two electrons occupy the same site, then they need to have opposite spins). Hence, to have a parallel spin, one electron should be promoted to a higher energy level (different k-state). Therefore, raising the kinetic energy of the system, which implies ferromagnetism is an unfavorable process.

In contrast, the presence of Coulomb interactions favors those two electrons can accommodate the identical energy though the direction of electronic spin should be antiparallel to another electron. If the decline of coulombic interactions energy exceeds the increase in kinetic energy, then spins parallel alignment is energetically favored, thereby spontaneous ferromagnetism transpires. Now, the number density of up-spins and down spins could be

$$n_{\uparrow} = \frac{n}{2} + \Delta E\ D(E_F) \tag{2.70}$$

$$n_{\downarrow} = \frac{n}{2} - \Delta E\ D(E_F) \tag{2.71}$$

Consequently, Hubbard's energy $E_u = Un_{\uparrow}n_{\downarrow}$ of the system is

$$E_u = U\left[\frac{n}{2} + \Delta E\ D(E_F)\right]\left[\frac{n}{2} - \Delta E\ D(E_F)\right] \tag{2.72}$$

$$E_u = U\left[\frac{n^2}{4} - \Delta E^{\,2}\,\{\mathrm{D(E}_F)\}^2\right] \tag{2.73}$$

Here, U is the repulsion between electrons. Normally, it is very difficult to evaluate, and in practice, U is adjusted to fit experimental data. Now the total energy in presence of magnetism

$$E_T = \mathrm{E}_K|_{M=0} + D(E_F)(\Delta E)^2 + U\left[\frac{n^2}{4} - \Delta E^{\,2}\,\{\mathrm{D(E}_F)\}^2\right] \tag{2.74}$$

Since total energy in absence of magnetism is

$$\mathrm{E}_T|_{M=0} = \mathrm{E}_K|_{M=0} + U\frac{n^2}{4} \tag{2.75}$$

This term represents the total energy of a system without magnetization, there we can have the total change in the energy in presence of magnetization as

$$\Delta E_T = \mathrm{D(E}_F)\ (\Delta E)^2 - U\ \{\mathrm{D(E}_F)\}^2\ (\Delta E)^2 \tag{2.76}$$

Therefore, we finally get the following result

$$\Delta E_T = \mathrm{D(E}_F)\ (\Delta E)^2[1 - U\ \mathrm{D(E}_F)] \tag{2.77}$$

Consequently, spontaneous ferromagnetism occurs if $\Delta E_T < 0$, which is satisfied if

$$U\ \mathrm{D(E}_F) \geq 1 \tag{2.78}$$

This is recognized as the Stoner criterion. From the Stoner criterion it is clear that for spontaneous ferromagnetism, the spin-down and spin-up band splitting is favored, only if the Coulombic interactions are robust (Hubbard U is larger) and Fermi-level density of states $\mathrm{D(E}_F)$ is large, thereby the stoner criterion is fulfilled. The density of states of the *s* and *p* bands is considerably smaller than the *d* band, and hence only the *d* band favors spontaneous

magnetization as per the Stoner framework.

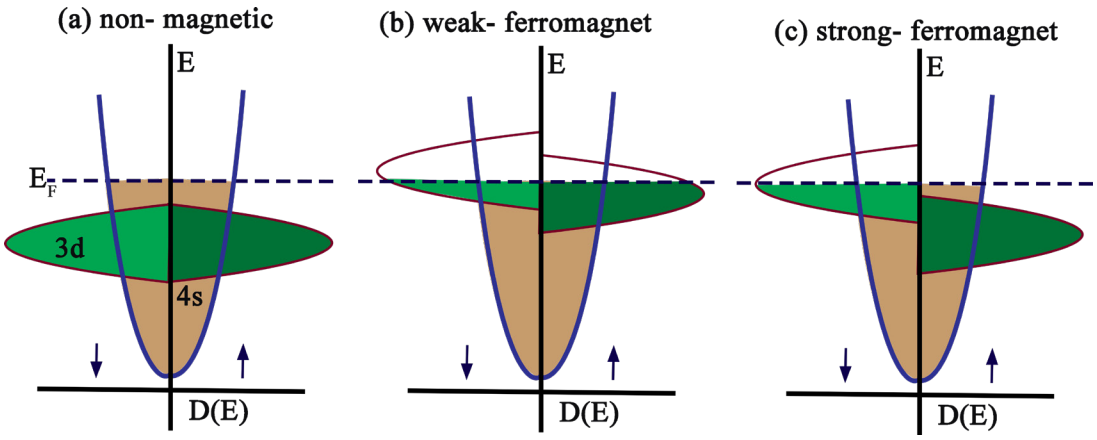

Figure 2.12. Representation of density of states (DOS) of non-magnetic, weak-ferromagnetic, and strong-ferromagnetic materials.

In Ni, Fe, and Co the Fermi energy crosses the 3*d* bands resulting in a large $D(E_F)$ and hence the Stoner criterion is satisfied [see Figure 2.9(b)], whereas in copper, the 3d band is complete, hence located well below the Fermi level and consequently the Stoner criterion is not satisfied. Moreover, if the majority spin channel is completely filled, it is a strong magnet, else it is a weak magnet. In Fe, the majority spin is not completely filled, so it is a weak ferromagnet, whereas in Co and Ni it is, so they are strong ferromagnets as shown in Figure 2.12.

Chapter 3. Experimental Methods

This chapter provides details on the perovskites thin-films epitaxy and characterization techniques such as structural and physical properties.

3.1 Perovskite Thin Films Growth

Thin-film fabrication is performed via atomistic deposition (atom by atom) of a certain material over a required substrate, thereby, depending on the deposition settings one can have a single crystalline, polycrystalline, or amorphous structure. The thin film deposition techniques could be categorized into two sets: (1) Physical vapor deposition (PVD), and (2) Chemical vapor deposition (CVD). The PVD method involves the material vaporization from a target via either thermal or athermal processes. The thermal process involves the target material sublimation or evaporation via supplying thermal energy. On other hand, in the athermal method the vaporization occurs upon the physical impingement of ionized gaseous molecules onto the target. In the CVD, a chemical reaction of a material to be deposited (volatile compound) with supplementary gases results in the production of a non-volatile solid, which is then deposited onto the substrate.

3.1.1 Pulsed Laser Deposition of Perovskites

Pulsed laser deposition (PLD) is a physical vapor deposition (PVD) method, In PLD, the material evaporation from the target takes place via means of an intense laser beam. PLD is a usually utilized for complex oxides thin films growth. A typical PLD system as portrayed in Figure 3.1, contains two main components: (1) an external laser source and (2) a vacuum chamber. A vacuum chamber includes vacuum pumps, pressure gauges, a target carousel, a substrate heater, and Reflection high-energy electron diffraction (RHEED). Moreover, PLD scheme is normally equipped with optical instruments such as attenuators, lenses, apertures, and mirrors, thereby properly focusing the laser beam on the target with the exact energy density.

Most PLD systems commonly utilize excimer lasers with a lasing medium comprises a blend of reactive gases (fluorine, krypton, and neon). The laser operating frequencies are generally 1-100 Hz. Film growth is performed in a reactive environment, such as for perovskite oxides, oxygen is utilized.

In PLD process, extremely intense laser-pulse is focused on the material target, leading to ablation (massive ejection of particles) of the target material. The laser pulse and target interaction strongly depend on laser beam intensity, where typically it is between 108 - 109 W/cm^2 with a nanoseconds pulse duration. The mechanisms via which energy is transferred to a target are:

Electronic sputtering. This is the principal mechanism in laser pulse and target interaction [35]. Upon photons impingement onto a target, the electron-hole pairs as well as electronic excitations are generated. Within picoseconds, the electronic excitations energy is shifted to the lattice ions through electron-phonon coupling [36]. Consequently, the lattice is heated, and, with sustained irradiation, an enormous number of particles start to eject from the target surface.

Collisional sputtering. In this, incident beam momentum is shifted to the target, thereby producing a particle expulsion from the target surface. In the case of the photon, the energy transfer is almost insignificant, however, if the incoming beam comprises huge particles (e.g., ions), then this mechanism becomes significant.

Thermal sputtering. In this, the incident laser beam gets absorbed into a small target area, hence partly melting the target surface and ultimately vaporizing the corresponding tiny area [35].

Hydrodynamic sputtering. This refers to target surface melting, thereby creating tiny droplets, though they are ultimately ejected from the surface.

Exfoliation sputtering. This occurs when fluence on the target is amply higher. Henceforth, the sustained and strong laser bombardment results in thermal shocks, and the target surface becomes cracked. This arises since there is no time for the thermal stresses to relieve via melting mode, thereby leading to an uneven target surface having elongated cone-shaped topographies [35,37].

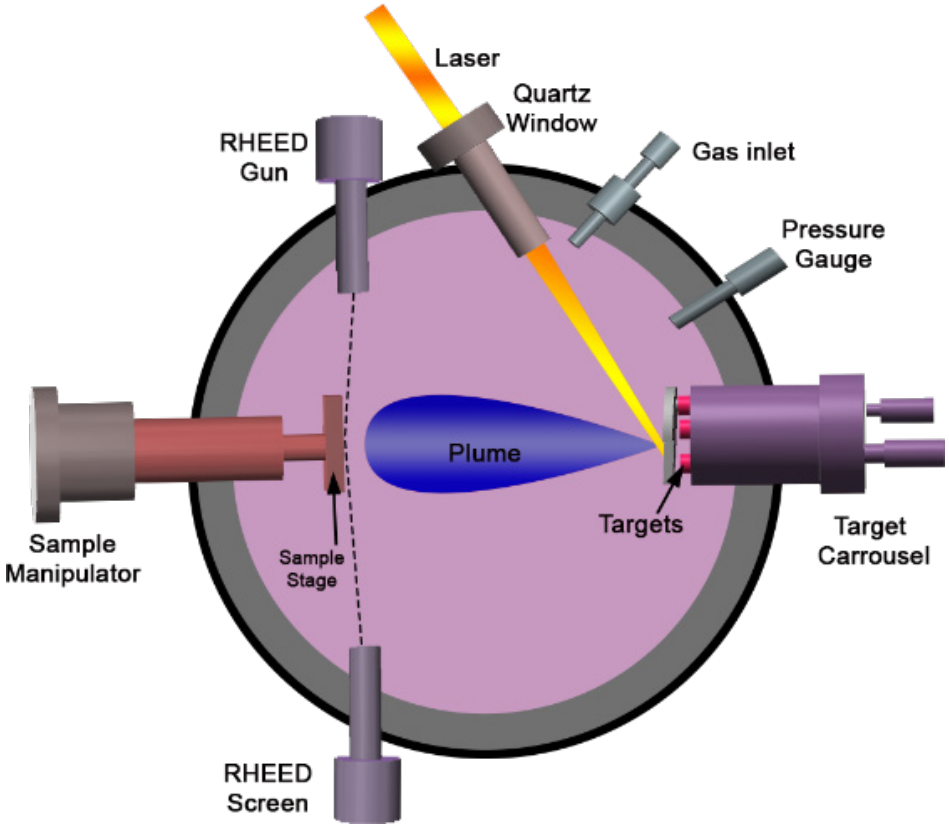

Figure 3.1. Illustration of pulsed laser deposition.

Nevertheless, ejected or evaporated species from the target material are relatively hot, and thereby some atoms are ionized. The underlying cloud of particles absorbs additional energy coming from the laser, leading to further ionization, ultimately resulting in an entirely ionized plasma in the target vicinity of 50 μm. Afterward, the so-called plasma plume magnifies away from the target surface [see Figure 3.1]. Plume particle species (atoms, molecules, ions, charged particles) then arrive at the substrate, resulting in the growth of the thin film.

Several parameters; for example, laser pulse wavelength, energy, duration as well as absorption coefficient and the material target reflectivity all can have an impact on the laser beam-target material interactions. Moreover, the plume behavior in a vacuum is not the same as in comparison to the environment of the ambient background gas. The plume expansion in a vacuum is not unidirectional, rather because of enlarged plasma density there exists a backward velocity component. However, the presence of background gas results in a decrease of the kinetic energy of plume species, leading to an increase in chemical reactions between gas and plume species. Moreover, laser fluence posts a substantial impact on the plume shape, and size. If the spot size formed by the laser on target is decreased while retaining a constant fluence, then material ejection decreases and subsequent plume would become shorter but wider. In contrast, if fluence is amplified, then an elongated plume shape is formed since the initial particles have a larger velocity.

3.1.2 Growth Kinetics

The process of thin-film deposition starts with production of the material flux atom species and their arrival onto the surface of substrate. If the vaporized species are not immediately reflected by the substrate surface, they condense onto substrate surface via kinetic energy transfer. The adsorbed atoms are referred to as *adatoms* (atoms on the substrate surface). Among adatoms, some undergo re-evaporation, because their energy could not overcome the energy of attachment. While for others, if the substrate surface is spatially uniform, then the diffusion of adatoms occurs, whereas the mobility is dependent on thermal energy and the substrate-adatoms interaction strength. The diffusion of adatoms outcomes in either adatom-adatom binding, thus forming a small nucleus (i.e., cluster), or adatoms may also diffuse and become attached to existing nuclei [see Figure 3.2(a)]. Since the newly developed small nuclei are not stable, re-evaporation could transpire unless a smaller nucleus attains a certain size. Upon

attainment of critical size, the adatom attachment and disassembling rates are balanced and the nucleus becomes stable. As the nucleus captures more atoms, either by direct condensation of incoming material or via diffusive bonding of adatoms, its enlargement is elucidated by following one of the following growth mechanisms: (1) Volmer Weber (Island Growth) [38] (2) Frank–van der Merwe (Layer Growth) [39] or (3) Stranski–Krastanov (Layer + Island Growth) [40].

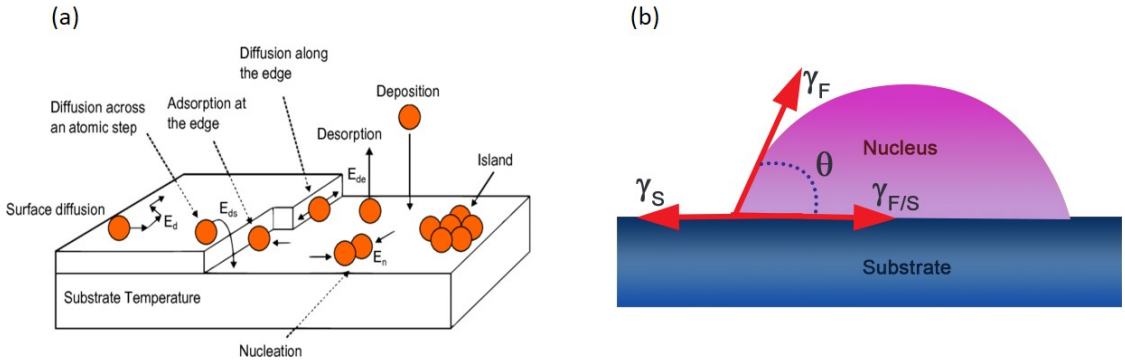

Figure 3.2. (a) Depiction of adatoms behaviors at the substrate surface, and (b) simplified depiction of a cluster of a deposited film.

In 1958, Ernst Bauer introduced a classification of epitaxial film growth modes based on thermodynamic considerations. Three film growth modes: Frank–van der Merwe (FM), Volmer-Weber (VW), and Stranski-Krastanov (SK) are typically observed depending upon surface energies or interface energy (γ). Remember, that tension is the work that should be done to construct a surface. Also, it is worth noting that γ is the force per unit length. Now, taking into consideration the film-island contact point with the underlying substrate [see Figure 3.2(b)], if the island wetting angle is θ, then the force at the substrate-nucleus clusters interaction location is [41]

$$\gamma_s = \gamma_{S/F} + \gamma_F \cos\theta \qquad 3.1$$

Where, γ_S, γ_F and $\gamma_{S/F}$ are surface tensions of substrate, film surface, and film-substrate interface, respectively.

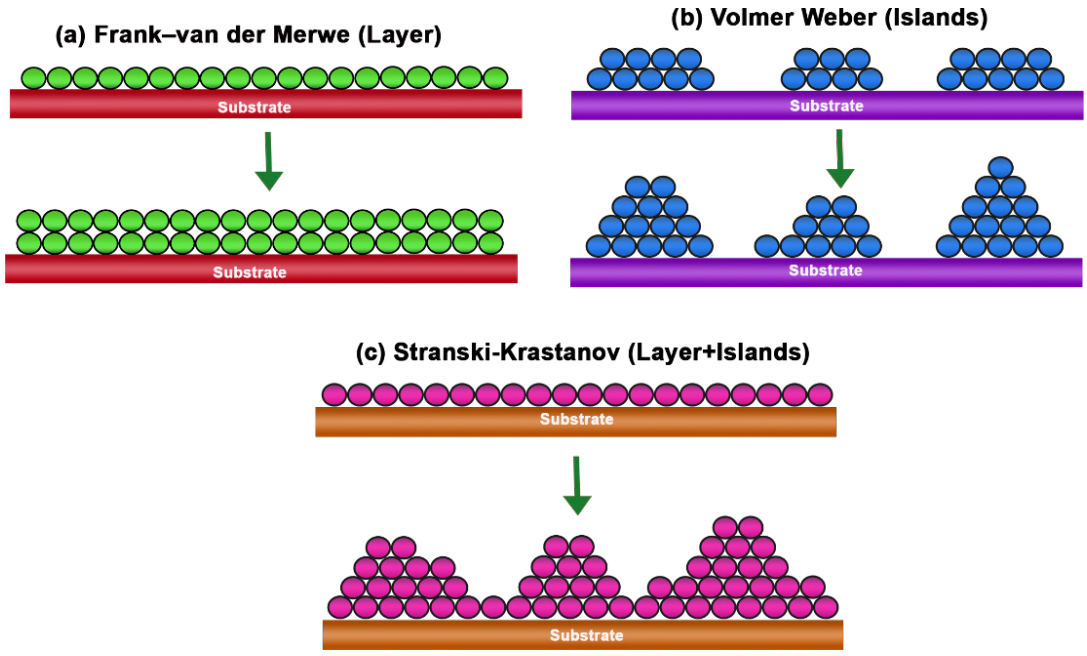

Figure 3.3. Schematics of film growth modes; (a) Frank–van der Merwe, (b) Volmer Weber, and (c) Stranski–Krastanov.

For idealized smooth as well as coherent growth, the film will completely wet the substrate, hence, $\theta = 0$, which can lead to Frank–van der Merwe (FM) growth also known as two-dimensional growth model [see Figure 3.3(a)]. In this case, the adatoms are strongly bonded to the substrate surface. The stable nucleus growth ensues in two-dimensions, leading to a formation of a continuous monolayer on the substrate surface. The first monolayer layer is then covered by a second layer, but the subsequent layer is less tightly bound. The layer-by-layer growth persists if bonding energy keeps on declining toward bulk-like value.

For Volmer-Weber (VW) growth mechanism [see Figure 3.3(b)], the adatoms-adatoms are more powerfully bonded as compared to substrate surface, resulting in development of three-dimensional island growth. For VW growth, with $\theta = 0$, we have $\gamma_s < \gamma_{S/F} + \gamma_F$. This kind of growth mode is shown when metals are deposited onto insulating substrates, graphite, alkali halides, and mica. The third kind, the Stranski-Krastanov (SK) thin film growth as shown in Figure 3.3(c), combines FM growth (layer-by-layer) and VW growth (islands). Initially, the

nucleation of adatoms outcomes in a two-dimensional monolayer development (FM-mode), followed by growth of three-dimensional islands (VW-mode). The change in the growth model from FM to VW emerges at a critical thickness and is associated with the strain build-up that can generally arise due to a very large film-substrate lattice mismatch. In SK growth, we have $\gamma_s > \gamma_{S/F} + \gamma_F$.

The three growth modes discussed above are valid if the thin film growth mechanism is near thermodynamic equilibrium, implying high substrate temperatures and low vapor flux. However, in PLD, film growth is not in equilibrium, thereby the growth kinetics rather than thermodynamics dictate the film morphology. In other words, the adatom diffusivity on the substrate surface in comparison to the deposition rate controlled via several parameters such as gas pressures, laser spot-size, laser energy, and laser fluence. regulates the film growth. The important kinetic parameters are; adatom diffusion constant D, adatom sticking probability at terrace edge, and energy barrier required to tumble over to a lower substrate-terrace. Among the aforementioned parameters, the diffusion coefficient is very important and is given as [37,42]

$$\mathrm{D} = \mathrm{a}^2 \nu_0 \exp\left(\frac{-\mathrm{E_D}}{\mathrm{k_B T_s}}\right) \tag{3.2}$$

Here k_B is the Boltzmann constant, T_s the substrate temperature, E_D be diffusion barrier, ν_0 is attempt frequency of adatom migration, and a is adatom characteristic hopping distance from one site to another. The diffusion coefficient is the most vital kinetic parameter since it governs the average distance known as diffusion length that an adatom might travel on a substrate surface, before becoming immobile

$$\mathrm{L} = \sqrt{D\ \tau} \tag{3.3}$$

Here, τ is lifetime of an adatom, and D the diffusion coefficient. Moreover, the diffusion is related to constant deposition flux as

$$L = \left[\frac{D}{F}\right]^{1/6} \quad 3.4$$

To understand the 2D growth, the following diffusion processes are considered: (1) adatom diffusion on the terrace, and (2) adatom diffusion to a lower terrace. Now, since a realistic substrate surface will display step terraces, which are spaced on average at $w = a/\varsigma$, here ς is the substrate miscut angle (radians) and a be lattice parameter of material. If the adatom diffusion length L (i.e., for large values of D/F) is greater in comparison to terrace width $L > w$, then adatoms at the substrate surface remain mobile until it reaches a step edge, where it gets their nucleated. Since all adatoms might effortlessly arrive at the terrace edge, thereby no island formation arises. Thus, instead of forming new nuclei on the terrace, the adatoms become attached to the step edges leading to the advancement of the step edge along the terraces. This is termed a step-flow growth mode. On other hand, if width of terrace (w) is bigger as compared to adatom diffusion length $L < w$, then nucleation of adatoms will occur on the terraces. In this case, the film could evolve on the terraces either in the Frank–van der Merwe (layer by layer), or Stranski–Krastanov (Layer+Island) growth mode.

3.1.3 Reflection High Energy Electron Diffraction

Reflection high-energy electron diffraction (RHEED) is an instrument that allows us to monitor and analyze the in-situ growth processes of thin films in ultra-high vacuum systems. RHEED utilizes a very fine collimated electron beam. First, the electrons produced in a filament followed by beam production having electronic accelerating energies of nearly 10-100 keV. The generated electron beam is focused onto a specimen at an angle of less than ~3°, leading to diffraction. The diffracted electron beam from the sample surface reaches a fluorescence screen. Consequently, an RHEED pattern is formed and could be recorded by utilizing a CCD or photo camera, just outside the viewport of the vacuum chamber. Generally, the Ewald sphere construction is employed for the understanding of the RHEED diffraction pattern [see Figure

3.4(a)].

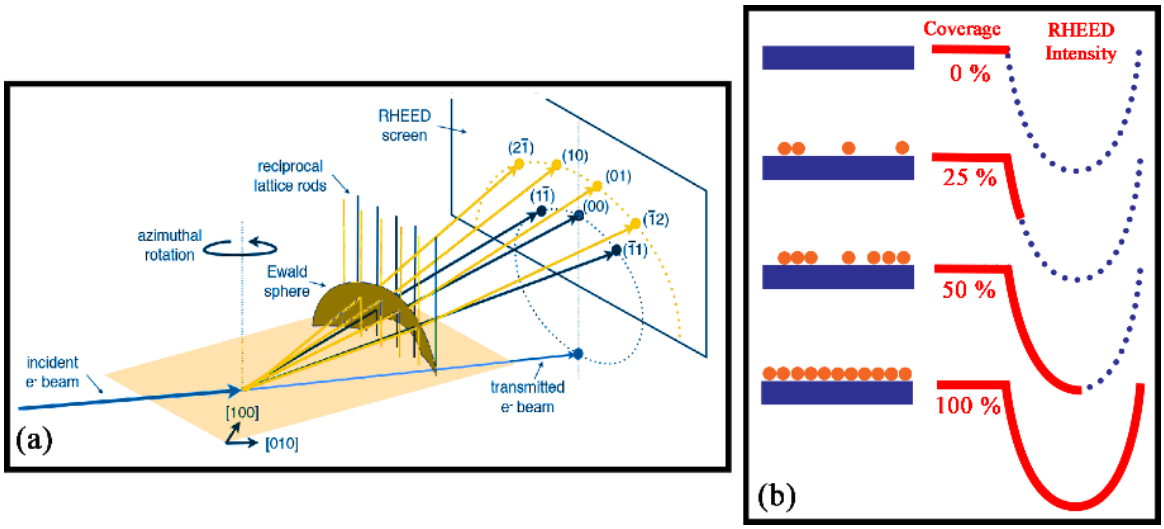

Figure 3.4. Geometrical setup of RHEED. (b) RHEED oscillations, where initial nucleation introduces the surface roughness and damping of RHEED intensity, through after filling of gaps, the intensity increases and achieves its maximum values upon completion of one smooth monolayer.

In three dimensions, the reciprocal lattice comprises a set of points. However, in RHEED, for a smooth single crystal surface, electrons are reflected from the surface. In this case, the electrons merely interact with the topmost film-layers, and hence diffraction comes only from the uppermost layers of the material. Thus, no diffraction condition exists in the third dimension, which is normal to surface of sample. Consequently, because of absence of a third diffracting condition, in 2D, the reciprocal lattice is not signified by points, rather it consists of a series of infinite rods or lines along the surface normal. In the presence of surface imperfections or finite response of the RHEED system, these rods are often expanded and possess a finite width. The diffraction condition will be satisfied if these lines or rods in the reciprocal space intersect the Ewald sphere. The Ewald sphere intersection with individual reciprocal rods results in a reflected beam, which is stretched out in form of a specular streak or spots. The streaks reside on the so-called Laue circles. The diffraction pattern, therefore, comprises a series of streaks or spots as shown in Figure 3.4(a). The smallest circle is a zeroth-order Laue circle and others are called

higher-order Laue circles. Thus, the RHEED pattern is a group of points on the so-called Laue circles (concentric) around the center point.

The growth of thin films in PLD could be monitored by an in-situ RHEED. In pulse laser deposition, the specular-spots intensity is logged as function of time The diffraction intensity is maximum if the sample surface is smooth [see Figure 3.4(b)]. Though upon adatoms nucleation, the surface roughness is transformed, leading to decrease in diffraction and specular spots intensity [see Figure 3.4(b)]. This tendency endures until approximately 40% of the surface is covered with the deposited material. Afterward, the incoming material fills in the remaining gaps, increasing the specular intensity. Once a smooth film-layer covers the substrate surface, the diffraction intensity retains back maximized value. Hence, via monitoring the intensity oscillations, the exact film thickness and termination could be deterministically controlled.

3.1.4 PLD Deposition System

The experimental PLD thin film growth chamber is revealed in Figure 3.5. Thin-film deposition via employing a pulsed laser deposition process (PLD) occurs in a vacuum chamber. The vacuum is maintained via a combination of roughing and Turbomolecular pumps. The deposition chamber is equipped with a rotating carousel, where six material targets could be mounted, and a sample stage (which could be heated ~1000°C). The High-Pressure Reflection High Energy Electron Diffraction (HP-RHEED) permits in-situ thin film growth monitoring. In the experiments described here, a KrF excimer laser (Lambda Physic, Compex) with a wavelength of 248 nm and frequency of 10 Hz is utilized.

The base pressure in the chamber is ~10^{-9} mbar, where a vacuum is attained via a combination of mechanical and turbo-molecular pumps. The PLD growth chamber is isolated by gate valves from the load-lock chamber, and the main chamber (consisting of Low energy electrons diffraction-LEED, X-ray Photoemission Spectroscopy-XPS, and Scanning Tunnel

Microscopy). For deposition, the substrate is placed on the sample holder, then it could be heated to a specific temperature. The substrate heating is performed via resistive heating, where a Pt-wire is wounded around the ceramic plate, which sits on a holder. With this specially designed heater, uniform heat distribution could be achieved. A pyrometer is used to read the deposition temperature. In the PLD chamber gasses such as oxygen could be introduced during the deposition process, where typical pressures range from 10^{-6} to 10^{-4} Torr.

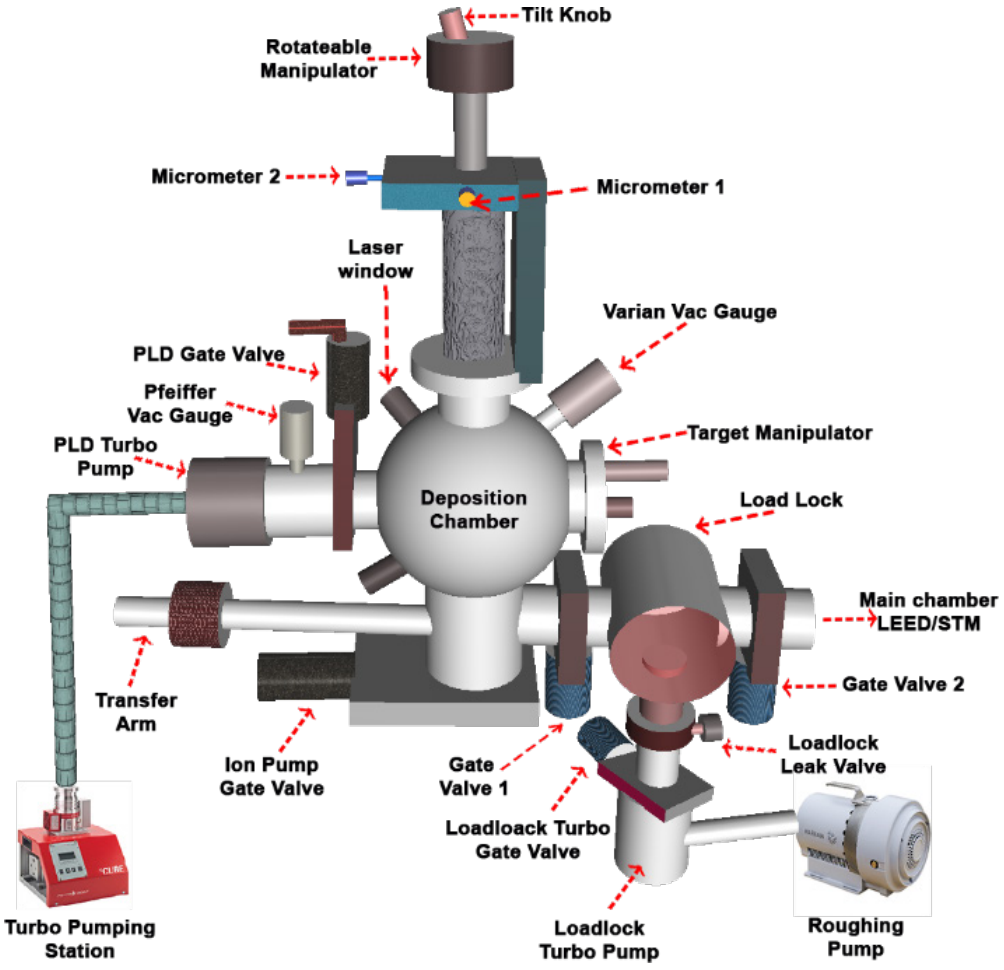

Figure 3.5. Schematic depiction of the pulsed laser deposition chamber.

3.2 Perovskites Heterostructures Characterization

This section provides details about the characterization techniques employed for the structural and physical properties of perovskite oxide heterostructures. The perovskite structural analysis is mainly characterized X-ray diffraction and scanning transmission electron microscope. For the electrical transport and magnetization measurements, the quantum design physical property measurement system (PPMS) and Magnetic Properties Measurement System (MPMS) are utilized, hence the working principles of SQUID and PPMS are described.

3.2.1 Scanning Transmission Electron Microscope

An electron microscope is a scientific instrument that utilizes a highly accelerated electron beam to scrutinize objects. There are three microscopes available: (1) Scanning Electron microscope (SEM), (2) Transmission electron microscope (TEM), and (3) Scanning Transmission Electron Microscope (STEM).

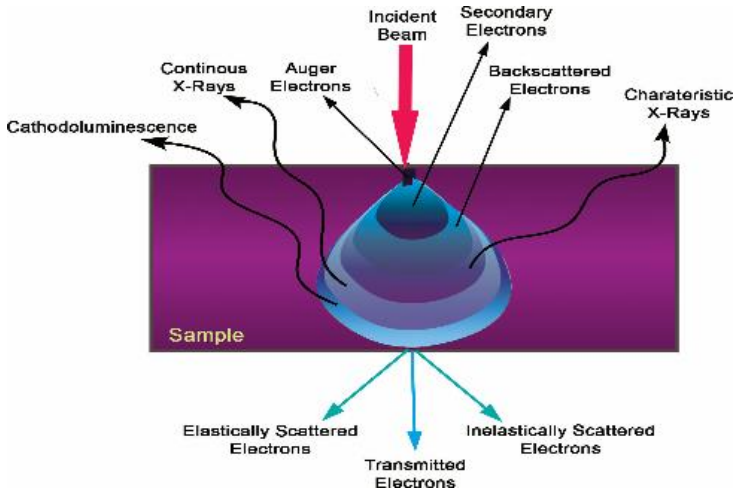

Figure 3.6. Illustration of electronic interactions a sample.

In SEM, the sample images are formed via scanning the specimen surface with an electron beam in a raster scanning pattern. The interaction of electrons with the specimen atoms outcomes in several signals that encompass details regarding the samples such as surface morphology, topography, and chemical composition. In TEM, a focused electrons beam

undergoes transmission, since samples are very thin. The electron beam interaction with the specimen outcomes in several signals, as represented in Figure 3.6. In SEM, the secondary and backscattered electrons are used for imaging. While in the STEM, the beam of electrons is focused on a fine location (0.05 – 0.2 nm), and could be scanned in a raster pattern. In TEM, coherently elastically scattered electrons are collected to produce the images.

The schematic illustration of a TEM column is depicted in Figure 3.7. The electron gun emanates an electron beam into an evacuated column via thermionic guns or field-emission gun. Here, the electron beam is accelerated, where the accelerating voltage is about 60 to 1000kV. In the TEM column, the electron beam path is controlled and collimated via utilizing the condenser lenses. An aperture is inserted to remove the widely scattered electron. The fine-tuning of the condenser lens system yields a collimated (parallel) or convergent incident mode having different spot sizes while interacting with the sample. In the TEM, the specimen is located between the condenser aperture and objective lenses. Here, the beam-specimen interactions take place, thereby various images and diffraction patterns are subsequently magnified for viewing. The electron beam transmits through specimen and is incident onto an objective lens. The objective lens is utilized primarily for the focusing and initial magnification of the image. The objective lens carries a magnification of ~20-50 times. The objective aperture filters transmitted beams that originate from the specimen in a specific range of angles. Next, the projector lens further magnifies the image coming from the objective aperture and then projects the signal onto a phosphor viewing screen. The signals generated are detected using numerous devices. The final image is observed via projection onto a phosphorescent screen, where photons are emitted when illuminated by the electron beam. A film camera is located underneath the phosphorescent screen. Nevertheless, a substitute for photographic film involves a computer digitizing and archiving camera.

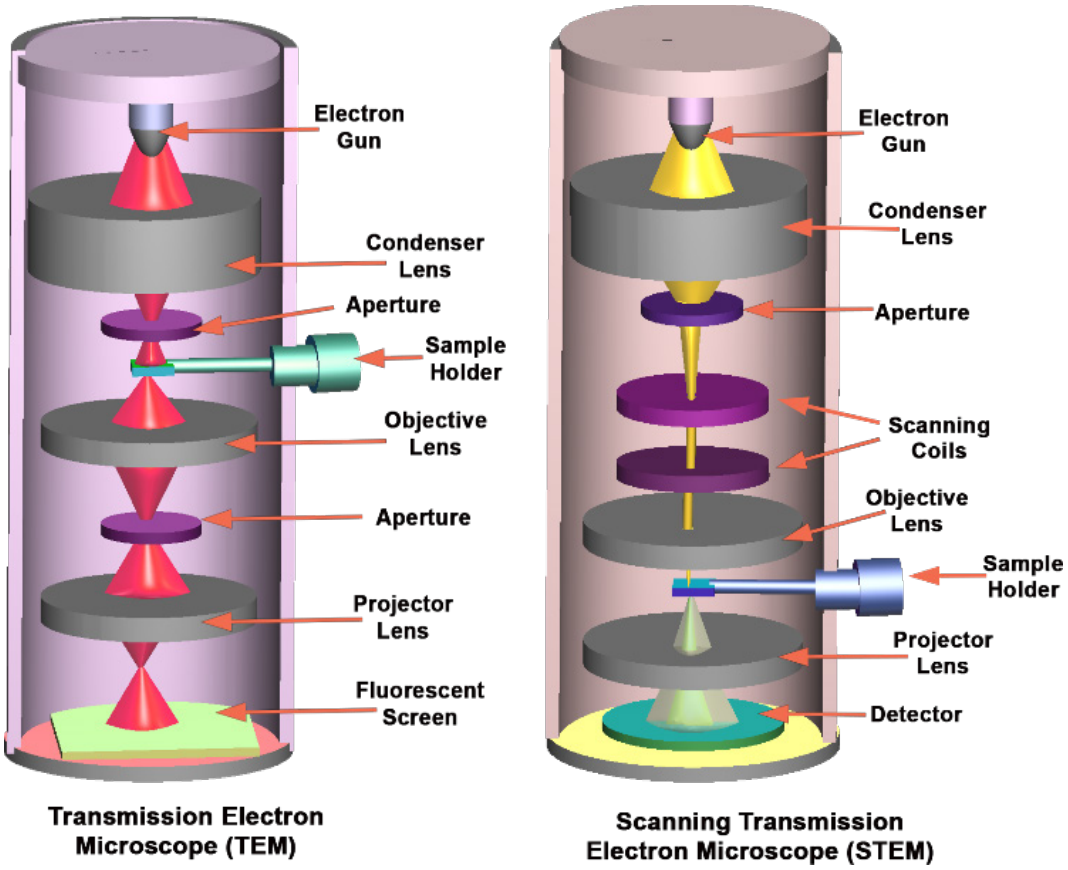

Figure 3.7. Schematics of TEM and STEM.

The method of image development for STEM microscope mode is comparatively different from the TEM. In a STEM, the beam of the electron is focused on a very small location of the specimen surface, thereby scanning the beam in a raster pattern over the specimen. In a STEM as depicted in Figure 3.7, the emanated electron beam passes through the condenser lens and aperture, which is then manipulated via scanning coils. The purpose of the scanning coils is to decrease the beam diameter and control the beam position, while the beam raster scans across the specimen. After the fine collimation of the beam via scanning coils, the beam passes through the objective lens and is projected onto the sample, and finally, the different signals are detected. The dispersed electrons are gathered via a series of detectors that cover different angular ranges. The detectors include a bright field (BF) detector, an Annular Dark Field (ADF) detector, High Angle Annular Dark Field (HAADF) detector as shown in Figure 3.8.

The bright-field signal is produced via detecting the transmitted beam on a bright-field detector. Bright-field mode is the traditional imaging mode for TEM where the transmitted electrons without much deflection are utilized to produce the image. Since the transmitted beam is collected by the BF detector, thus vacuum appears bright, while crystalline or high mass materials will appear dark. The BF gathers elastically scattered electrons with a scattering angle of less than 10 mrad.

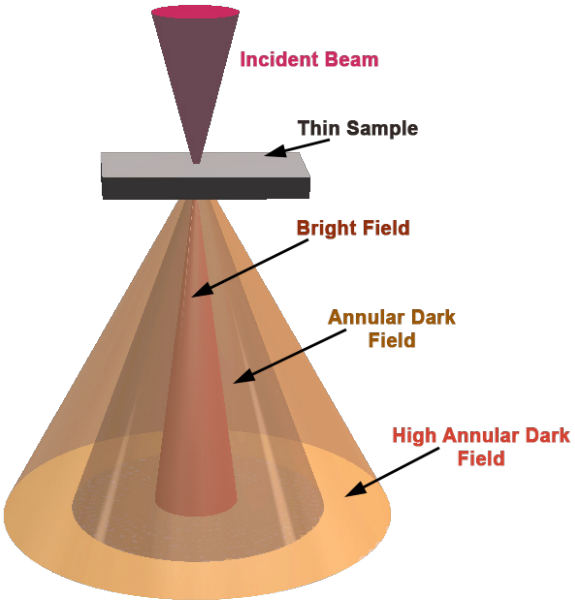

Figure 3.8. Depiction of the bright-field (BF), annular dark-field (ADF), and high-angle annular dark-field (HAADF) detectors of a STEM.

The annular dark-field detector (ADF) gather signals from the scattered electrons. In the dark field mode, the transmitted beam is omitted, while the dispersed electron beam is selected. Therefore, the parts with material presence look bright, while the areas where no electron scattering occurs, appear black (dark) [see Figure 3.9]. In the underlying cause, the heavier the atom, the larger the scattering, which leads to an atomic number (Z) contrast in the image. Hence, in ADF, the regions with heavier regions are brighter, while in the bright field the regions with heavier atoms are darker as shown in Figure 3.9.

If incident electron is nearby atomic nucleus, then electron will be elastically scattered at higher angles and are gathered by the HAADF detector, forming a HAADF image. The ADF gathers the electrons with angles in 10-50 mrad, While, HAADF collects the incoherent electron scattered at angles higher than 50 mrad. In case of HAADF imaging, brighter spots generally characterize the heavier atoms, and the darker regions signify the light elements.

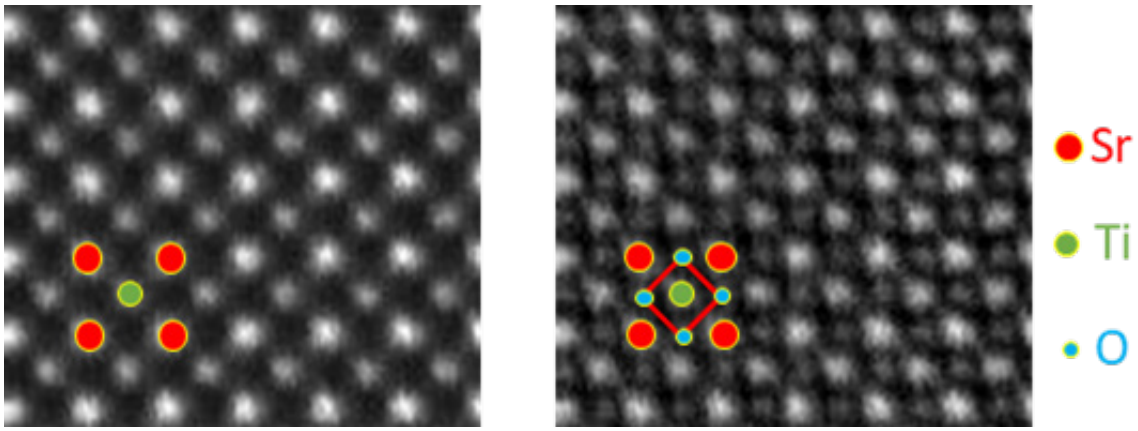

Figure 3.9. Annular dark-field (left panel) and inversed-annular bright-field (right panel) imaging of $SrTiO_3$.

3.2.2 X-ray Diffraction

X-ray diffraction (XRD) is a systematic instrument to detect and quantitatively determine crystallographic forms, orientation, lattice parameters, texture, crystallite size, phases, etc. X-rays are electromagnetic radiations analogous to light, though possess a smaller wavelength. In an X-rays tube, electrons are generated via heating of a tungsten filament cathode, where this cathode is held at a large negative potential. The emitted electrons are accelerated via high potential 20-60 KV toward a metal target (anode). The collision with the target (water-cooled anode) results in an energy loss of electrons, which manifests itself as X-rays. If incident electrons colliding with the target possess large enough energy, then it might remove an electron from the atom's inner shell (target), leading to an excited atomic state. Thus, to lower the overall energy, a higher-shell electron jumps to lower shell [see Figure 3.10]. Consequently, an X-ray

photon emission has energy equivalent to difference between lower-and higher-energy shells. The emitted radiation thus possesses a unique wavelength signature of the target element. The X-rays emit in all possible directions, however, a narrow beam with a tiny angle is permitted to come out of the evacuated tube, which is then collimated and directed onto the sample.

Consider, that an X-ray beam is focused onto a crystal having collection of atoms positioned in particular parallel planes. The crystallographic planes designated as Miller indices (hkl) are parallel atomic planes bisecting the unit cell, and these are utilized to define crystallographic directions. The X-ray diffraction techniques are grounded on the reflection of x-rays from these parallel atomic planes. It should be noted that x-rays are not being reflected, rather they are scattered, however, it is convenient to picture them as being reflected.

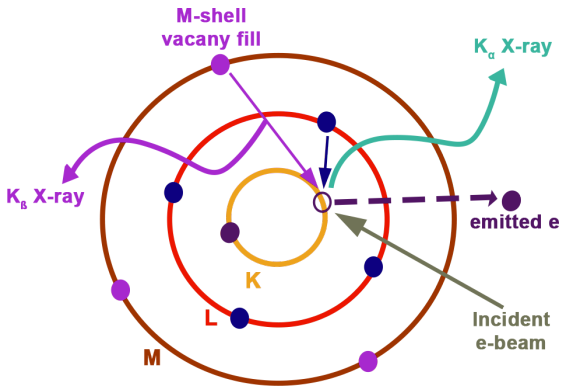

Figure 3.10. Representation of X-ray's emission.

As revealed in Figure 3.11, assume an X-ray beam is directed (making an angle θ with crystal planes) onto a crystal possessing periodically arranged atoms on a set of parallel miller planes. When X-rays interact, then individual atoms can scatter incident X-rays, and if we have several atoms, then the X-ray beam scatters in all possible directions. However, here we take into consideration that scattering happens with angle θ as in Figure 3.11. Because of the periodic atomic arrangement, the X-rays scattered could be in phase and thereby interferes constructively. According to Figure 3.11, the distance between the planes is *d*, and path difference among

incident and reflected beams is $2d\sin\theta$. The constructive interference occurs only if path difference is an integer multiple of X-rays wavelength: $n\lambda = 2d\sin\theta$. This condition is Bragg's law. Where λ is the incident X-ray wavelength, n is an integer, d the inter-planer spacing, and θ the incidence and reflection angle. Thus via, using a monochromatic X-rays beam of known wavelength λ and measuring the θ, the plane spacing d could be determined.

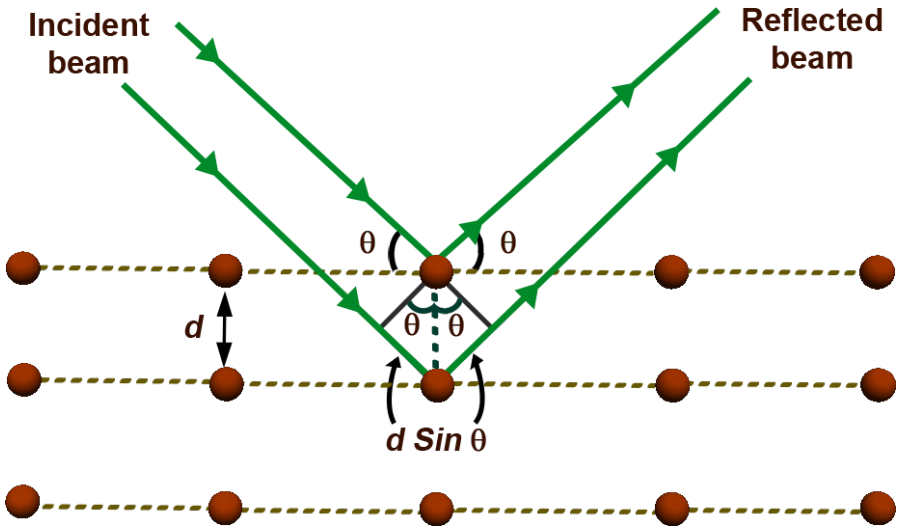

Figure 3.11. Bragg diffraction condition.

Generally, the X-ray diffraction technique involves measurement of the diffraction angle 2θ, rather than θ. Thus, by simultaneously, altering the incident wave packet angle and detection angle to equivalent θ values, the reflected wave packet intensity could graph versus the 2θ value. From the diffraction measurements via Bragg's law, the inter-planer spacing d is obtained, and then lattice parameter a is obtained, since, the interplanar spacing d is related to (a) and hkl in cubic systems as follows [43,44]

$$d = \frac{a}{\sqrt{h^2 + k^2 + l^2}} \qquad 3.5$$

The X-ray diffraction in reciprocal space is described via a geometrical construction identified as the Ewald sphere.

To construct the Ewald's sphere in k-space proceed as follows: Draw an incident beam

having wave vector $\boldsymbol{k}$ with length 1/λ. In our case, the origin of reciprocal space lies at the end point of wavevector $\boldsymbol{k}$. A sphere (circle in 2D) of radius 2π/λ is then drawn. This sphere is identified as the Ewald sphere or the sphere of reflection. When any reciprocal lattice point (hkl) lies on Ewald sphere, then diffraction emerges.

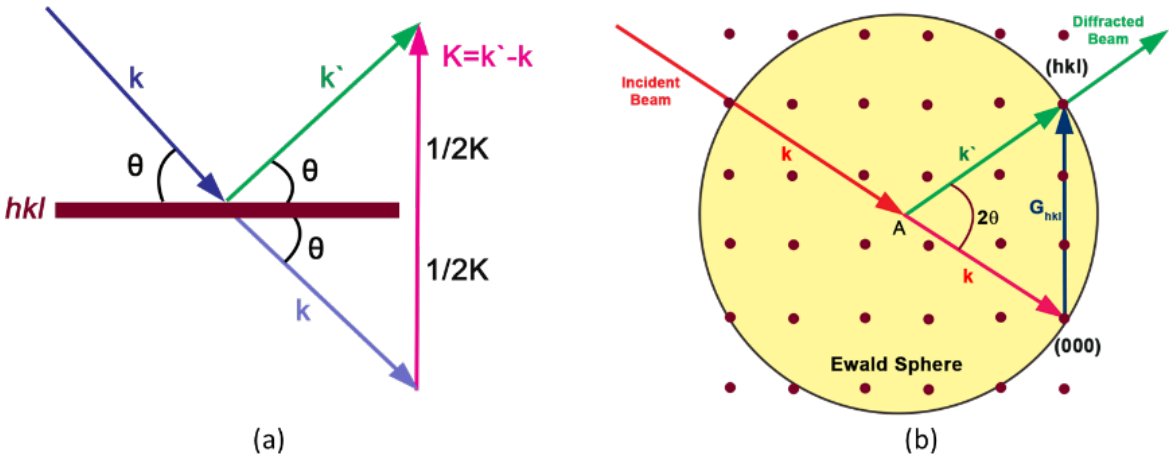

Figure 3.12. (a) Depiction of the Laue condition and Bragg plane. (b) Ewald's sphere.

The diffracted beam with wave vector $\boldsymbol{k}'$ and length 1/λ is drawn from the sphere origin to the intersecting point (hkl). Since, $\boldsymbol{k}$ and $\boldsymbol{k}'$ have the same magnitude, the endpoints of both vectors are located on a circle, and hence the scattering vector is $\boldsymbol{K} = \boldsymbol{k}' - \boldsymbol{k}$ must lie on the surface of a sphere. Moreover, it follows that both $\boldsymbol{k}$ and $\boldsymbol{k}'$ make the same angle θ with a plane perpendicular to $\boldsymbol{K}$, thus an angle between $\boldsymbol{k}$ and $\boldsymbol{k}'$ is 2 θ. In reciprocal space, a constructive interference transpires, if the change in wave vector $\boldsymbol{K}$ equals a reciprocal lattice vector $\boldsymbol{G}$. This is Laue condition. The Laue condition is satisfied if the tip of the incident and diffracted wave vectors must have to lie Ewald's sphere surface. The condition $\boldsymbol{K} = \boldsymbol{G}$ is satisfied whenever the surface of the sphere coincides with the point of the reciprocal lattice. At these points, the diffraction beams are produced and they are labeled with indices (hkl) corresponding to the relevant reciprocal lattice point. Thus, Bragg reflection occurs with a Bragg angle θ, from the real lattice planes that are perpendicular to the reciprocal lattice vector.

In epitaxial films, the lattice constant and substrate are very close, hence, special experimental equipment is necessary that could determine closely spaced peaks (normally 0.001° apart) of the substrate and film. This is performed via high-resolution X-ray diffraction (HRXRD). Figure 3.13 depicts the set-up of a typical HRXRD.

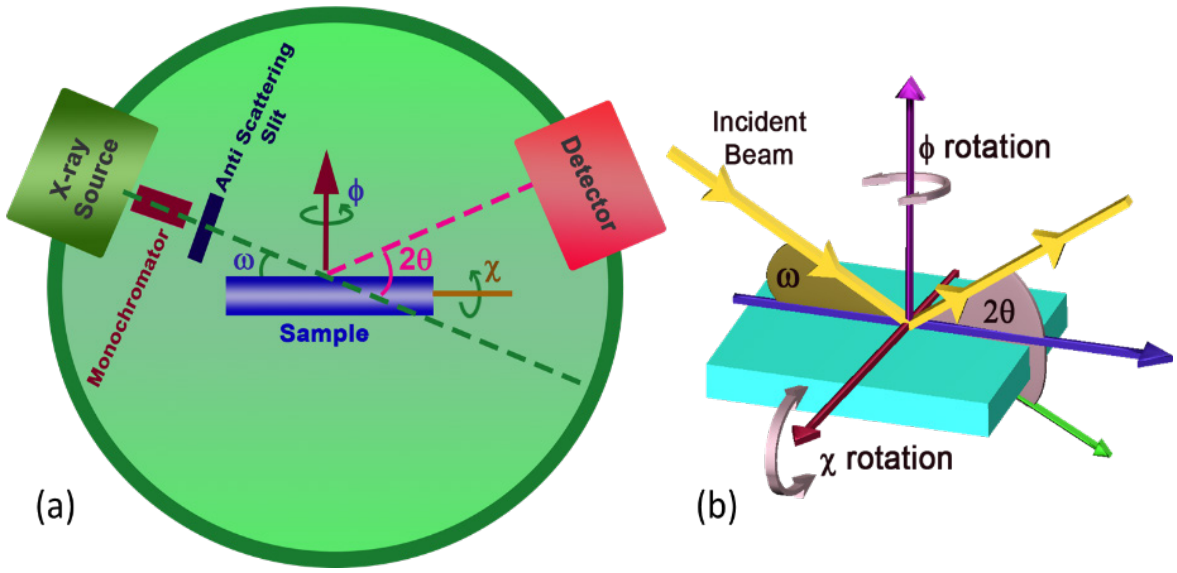

Figure 3.13. Graphics of (a) High-resolution XRD diffractometer, and (b) sample stage.

To attain the necessary high resolution, monochromatic X-rays and an analyzer are required. The monochromator comprises two parallel Ge (220) crystals and a mirror to focus X-rays. On other hand, analyzer assists in the reduction of beam divergence. There are four angles ω, 2θ, φ, and χ of diffractometer. The incidence angle is ω (angle between the incoming X-ray and the specimen holder), while a reflection angle is 2θ (angle between an extended incident X-ray and reflected beam). Moreover, the sample holder undergoes 360° rotation around its surface normal axis, whereas this rotation angle is φ. Additionally, the specimen holder could either tilt up or down 180°, whereas χ signifies the tilting angle. Moreover, x and y correspond to the horizontal and vertical positions, respectively, and z the sample height.

θ-2θ scan. In this case, both sample holder and detector are rotated, while keeping ω = θ, hence, called symmetric scan. During the scan, the incoming and reflected X-ray beam angle is

changed simultaneously. Thus, in the θ-2θ scan, a scattering vector $\vec{s}$ is perpendicular to film plane. This θ-2θ scan permits planes that are parallel to the specimen surface to produce diffraction, while others cannot since the reciprocal vector of the other planes resides in a different direction from $\vec{s}$, implying no Bragg's diffraction. In the symmetric θ-2θ scan, the reflection befalls from parallel crystal planes aligned parallel to the specimen surface, therefore, this scan yields an information only about out-of-plane film orientation. The symmetric scan (θ-2θ) is utilized for measurements such as lattice constant, crystallinity, and thin films phase. Figure 3.14(a) depicts an example of symmetric θ-2θ scan. The most intense peak generally corresponds to the substrate, while the film peak can appear either right or left of the substrate peak, depending on the tensile or compressive strain, respectively. As an example, the film peak in Figure 3.14(a) is at a higher angle as compared to the substrate peak, thus it shows that film is under tensile strain. Moreover, thickness fringes, are the result of interference for beams originating from the substrate-film interface and film surface. Normally, presence of fringes demonstrates the crystallinity of thin-film, as for the manifestation of interference fringes, the film interface and surface have to be well-defined.

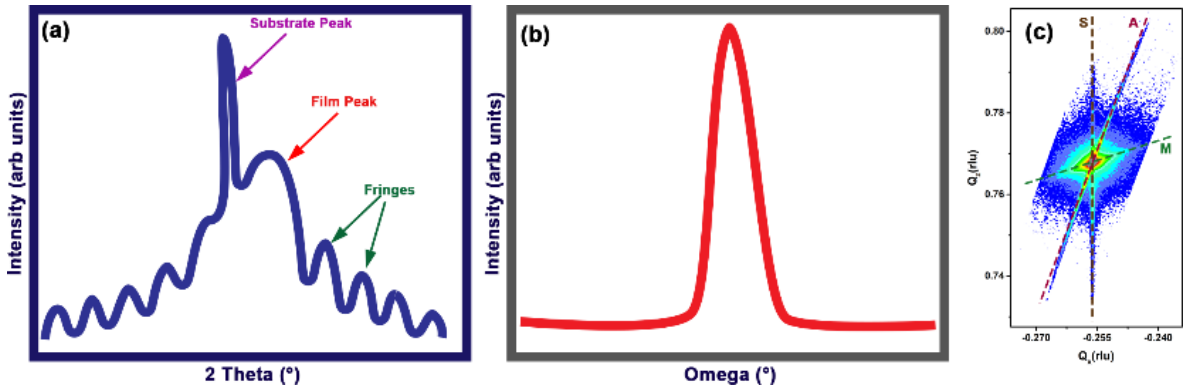

Figure 3.14. Depiction of (a) θ-2θ scan, (b) rocking curve (omega scan), and (c) reciprocal space map.

ω-scan. In this scan, detector and X-ray source are stationary, while the specimen is rotated or "rocked", hence only ω changes. Thus, the scan is termed a rocking curve (intensity vs

omega). In a rocking curve scan, detector is at a specific Bragg angle $2\theta_{hkl}$, while the sample is rocked at a small angle (varying ω). The ω scan is utilized to measure orientation and spread of a film (mosaicity), imperfections, dislocations, misorientation, and inhomogeneity. An example of intensity vs omega is shown in Figure 3.14(b). We often use full width at half maximum (FWHM) to define broadening of peak. If the peak is wider, the greater the material volume possesses an orientation slanted from the normal of the substrate. As the mosaicity and curvature often result in absence of perfectly parallel planes, consequently, some of the planes are tilted and the sample needs to rock at certain angles to fit the diffraction vector, which causes the broadening of the rocking curve.

χ scan. In χ scan, the specimen holder is tilted either up or down, while 2θ and ω are kept static at specific values or in other words, the sample plane is rotated with respect to the incoming beam.

φ scan. In case of φ scan, specimen holder undergoes a rotation by 360° about the sample holder's normal, whereas the other three circles are kept the same.

Reciprocal Space Mapping. Additional information about the inter-planar spacing and defects could be attained from reciprocal space maps (RSM). RSM is a 2D section in reciprocal space, in which both ω and 2θ are scanned. RSM is gained via a sequence of ω-2θ scans at successive ω-values, thereby resulting in a mapping pattern. The mapping provides information about the film epitaxy, i.e., strained, relaxed, or if there are any periodicities in the film.

3.2.3 Magnetic Properties Measurement System

The magnetization measurements were completed via the Magnetic Properties Measurement System (MPMS). The MPMS is a very sensitive magnetometer, which utilizes a liquid Helium cooled superconducting quantum interference device (SQUID). The SQUID is made from superconducting loops comprising Josephson junctions. The measurements could be

done in the temperature range 1.9-400 K. Liquid helium and liquid nitrogen are utilized to cool the magnet and control the temperature inside the sample space. The highly homogeneous superconducting magnet provides a magnetic field strength of 8 Tesla having uniformity of nearly 0.01% at a distance of 4 cm. The Reciprocating Sample Option (RSO) included in MPMS can measure DC magnetization in range of 1×10^{-8} emu to 5 emu.

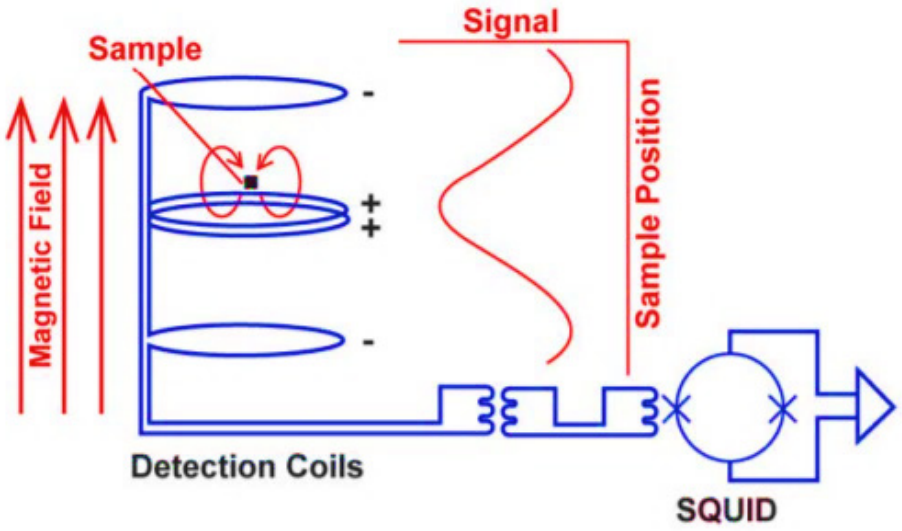

Figure 3.15. Schematic representation of SQUID detection.

MPMS utilizes a DC scan technique to measure magnetic flux in a superconducting loop as a function specimen position as shown in Figure 3.15, the sample is mounted such that it can move through the superconducting detection coils. For the measurements, the sample moves slowly parallel to the applied magnetic field between superconducting detection coil. As a result, the magnetic flux changes, thereby inducing an electric current in detection coils. The induced current is inductively attached to current-to-voltage converter (SQUID region). After the sample has moved through a certain range (~4 cm), the measured signal is fitted and then converted into a magnetic moment value in emu. It should be noted that as the detection coil and the SQUID input coil arrangement create a closed superconducting loop through the connecting wires, any

current modification in the detection coil results in a subsequent change in the SQUID output voltage. Hence, the specimen magnetic moment could be converted to the output voltage, which the system measures.

3.2.4 Physical Property Measurement System

The Quantum Design Physical Property Measurement System (PPMS) is versatile characterization instrument capable to perform various measurements such as electronic transport, DC/AC magnetization, and torque magnetization, etc. The PPMS could accomplish measurements in 1.75-400 K and external magnetic fields of 14 Tesla. The PPMS major components are (1) Dewar, (2) Probe, (3) Model 6000 PPMS Controller, (4) Vacuum Pump, and (5) Electronic cabinet [45].

Dewar is constructed from aluminum metal; consisting of superconducting magnet and contains liquid helium. The Dewar outer layer possesses a reflective superinsulation to minimize helium loss. Moreover, the Dewar is enclosed by a jacket space that comprises liquid nitrogen. The Dewar cools down the elements contained inside the probe assembly. The schematic illustration of the Dewar is portrayed in Figure 3.16(a).

The Probe is constructed from several stainless tubes. The probe comprises numerous tools such as temperature sensing, electronic interfaces, superconducting coils, and helium gas impedance tubes. To avoid the radiative power loss into helium, the probe assembly between its inner and outer vacuum tubes is made in such a way that it possesses an extremely insulated vacuum section. The experimental apparatus is positioned inside a vacuum tube, which goes through the center of the probe [see Figure 3.16(b)-(c)]. With the assistance of a 12-pin connection, the experimental device could be connected to the Model 6000 Controller.

The Model 6000 PPMS Controller is a user interface that comprises a CPU, motherboard, system bridgeboard, and gas-control valves. The CPU regulates the system processing, while the

motherboard administers the system integrations. The function of the bridgeboard is to supply the temperature of the system information, where the combination of gas valves inside Model 6000 is utilized to regulate the temperature.

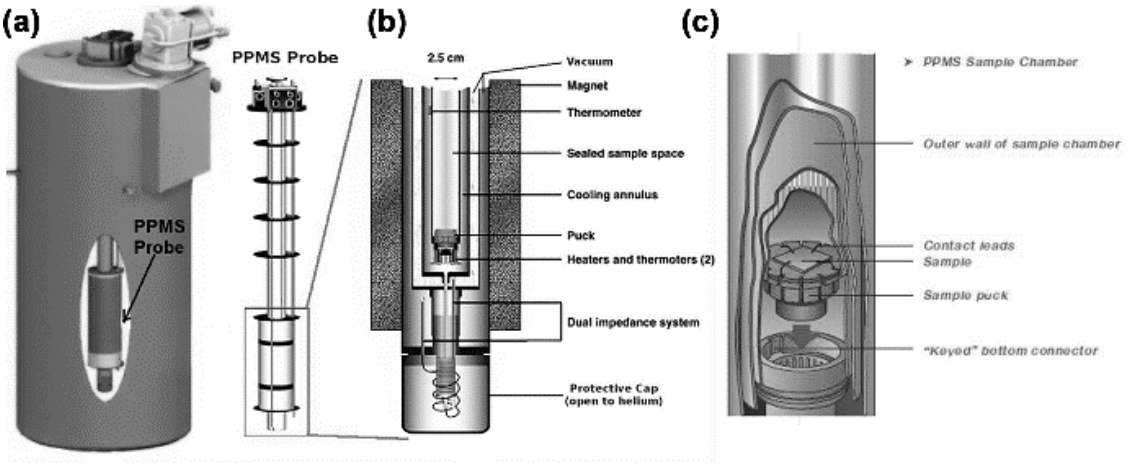

Figure 3.16. Physical property measurement system (a) Dewar, (b) probe, and (c) sample chamber. Adapted from [46].

Furthermore, the operation of the vacuum pump is to regulate the sample chamber pressure and with that, it also assists in thermal control. This pump is installed below the electronic cabinet. The electronic cabinet houses several configurations such as a model 6000 controller, vacuum pump, and power supplies. Moreover, the power cables are attached to the electronic cabinet. Additionally, the electronic cabinet is related with the MultiVu programming interface. MultiVu is Windows-based software, which holds the essentials to run the measurements. With this interface, the measurement sequences along with other control parameters necessary for measurement operations are developed and controlled.

Chapter 4. Origin of Insulating and Non-ferromagnetic $SrRuO_3$ Monolayers

The electro-magnetic properties of ultrathin epitaxial ruthenate films have long been the subject of debate. Here we combine experimental with theoretical investigations of $(SrTiO_3)^5$-$(SrRuO_3)^n$-$(SrTiO_3)^5$ (STO^5-SRO^n-STO^5) heterostructures with n = 1- and 2-unit cells, including extensive atomic-resolution scanning-transmission-electron-microscopy imaging, electron-energy-loss-spectroscopy chemical mapping, as well as transport and magneto-transport measurements. The experimental data demonstrate that the STO^5-SRO^2-STO^5 heterostructure is nearly stoichiometric, metallic, and ferromagnetic with $T_C \sim 128$ K, even though it lacks the characteristic bulk-SRO octahedral tilts and matches the cubic STO structure. In contrast, the STO^5-SRO^1-STO^5 heterostructure features Ru-Ti intermixing in the RuO_2 layer, also without octahedral tilts, but is accompanied by a loss of metallicity and ferromagnetism. Density-functional-theory calculations show that stoichiometric n = 1 and n = 2 heterostructures are metallic and ferromagnetic with no octahedral tilts, while non-stoichiometry in the Ru sublattice in the n = 1 case opens an energy gap and induces antiferromagnetic ordering. Thus, the results indicate that the observed non-stoichiometry is the cause of the observed loss of metallicity and ferromagnetism in the n = 1 case.[1]

4.1 Introduction

Complex-oxide heterostructures have generated significant interest because of their diverse emergent phenomena, including ferromagnetism [47–49], ferroelectricity [50], interfacial 2D electron gas [51], topological spin texture [52], strain-induced superconductivity [53], etc. However, one limitation in the design of thin-film-based oxide heterostructures is the occurrence

[1] This work is published as: Ali, Zeeshan, Zhen Wang, Andrew O'Hara, Mohammad Saghayezhian, Donghan Shin, Yimei Zhu, Sokrates T. Pantelides, and Jiandi Zhang. "Origin of insulating and nonferromagnetic $SrRuO_3$ monolayers." *Physical Review B.* 105, 054429 (2022).

of dead layers exhibiting insulating and non-ferromagnetic (FM) behavior below a certain film thickness [54–56]. As a prototype example, bulk 4*d* transition-metal oxide $SrRuO_3$ (SRO) has an orthorhombic perovskite lattice structure and a FM-metallic ground state with a Curie temperature of ~160 K [9]. However, ultrathin films of SRO grown on substrates such as $SrTiO_3$ (STO) exhibit intriguing properties that are different from bulk counterparts [57], including the occurrence of metal-insulator transition (MIT) and non-FM state [56,58].

Historically, the earliest experimental investigation by Toyota et al. [59,60] initiated interest in thickness-dependent properties of SRO, where MIT is observed to arise at a film thickness of 4-5 unit-cells (u.c.). Nonetheless, different values have since been reported for the MIT critical thickness, from 2 u.c. [56], to 3 u.c. [58,61,62], and 4 u.c. [63], with the variance usually attributed to the degree of disorder existing in films. Numerous theoretical studies have explored the origin of MIT, while remaining inconclusive regarding the critical thickness and nature of the ground state, i.e., whether FM or antiferromagnetic (AFM) insulator [13,64–66]. Several authors suggested that reducing film thickness may enhance electronic correlations [67–69] and result in a structural transition [70]. Rondinelli et al. [13], however, reported a comprehensive theoretical investigation of these effects and found that neither enhanced electronic correlations nor structural transitions could reproduce the experimentally observed MIT, leading to a suggestion that extrinsic effects (such as surface disorder and defects) or dynamic spin correlations may be the dominant factor. To overcome the surface-induced disorder, single-unit SRO in the form of $(SRO)^1$-$(STO)^5$ superlattice geometry has been examined experimentally. However, different ground states of single-u.c. SRO superlattices are obtained, from a non-FM insulator [71,72] to FM insulator [73] to borderline FM metal [74]. They are in contrast to the theoretically suggested half-metallic state for 1 u.c. SRO layer confined within STO lattice [68].

In this thesis, we report a combined experimental and theoretical investigation on $(SrTiO_3)^5$-$(SrRuO_3)^n$-$(SrTiO_3)^5$ (STO^5-SRO^n-STO^5) heterostructures (n = 1, 2 u.c.). Electric- and magneto-transport measurements demonstrate that STO^5-SRO^1-STO^5 is insulating and non-FM, whereas STO^5-SRO^2-STO^5 is FM-metallic with a Curie temperature of ~128 K. Atomically resolved structural analysis reveals that octahedral tilts are absent in both heterostructures, thus ruling out such structural changes as a controlling factor for such drastic property differences. On the other hand, atomically resolved electron-energy-loss-spectroscopy (EELS) chemical maps show that STO^5-SRO^1-STO^5 is nonstoichiometric with substantial interface induced Ti-Ru intermixture, while STO^5-SRO^2-STO^5 is nearly stoichiometric. Density functional theory (DFT) calculations find that stoichiometric STO^5-SRO^n-STO^5 (n = 1, 2 u.c.) are still FM-metallic without SRO octahedral tilts. Ru deficiency caused by Ti-Ru intermixing leads to the stabilization of AFM ordering and insulating behavior in the monolayer SRO indicating that the experimentally observed intermixing is indeed responsible for the observed loss of metallicity and ferromagnetism.

4.2 Heterostructure Fabrication and Characterization

Film Epitaxy. Heterostructures of the form STO^5-SRO^n-STO^5 with n = 1, 2 u.c. were fabricated via pulsed laser deposition (PLD) on $SrTiO_3$ (STO) substrates oriented with a (001) surface. Both STO^5-SRO^1-STO^5 and STO^5-SRO^2-STO^5 heterostructures have two repetitions of SRO/STO building blocks [see Figure 4.1(a)]. The STO substrates were first sonicated in deionized water and then treated for 30 seconds in buffered hydrogen fluoride, followed by annealing at 950° C in an oxygen atmosphere to produce atomically smooth surfaces. The SRO and STO films were grown at 650° C with an oxygen pressure of 100 mTorr and 10 mTorr, respectively. A KrF excimer laser (λ = 248 nm) laser repetition with a rate of 10 Hz (SRO) and 5 Hz (STO), and energy of 300 mJ (SRO) and 260 mJ (STO) was used. Post deposition, the

samples were cooled down at ~12°/min to room temperature in 100 mTorr oxygen.

The film thickness was monitored by an in-situ reflection high-energy electron diffraction (RHEED). Figure 4.1(b) and Figure 4.1(c) show *in situ* RHEED results. Time dependent RHEED oscillations show stabilized layer-by-layer film-growth mode throughout the deposition process. Moreover, the RHEED pattern of SRO and STO sublayers indicates an atomically smooth film surface.

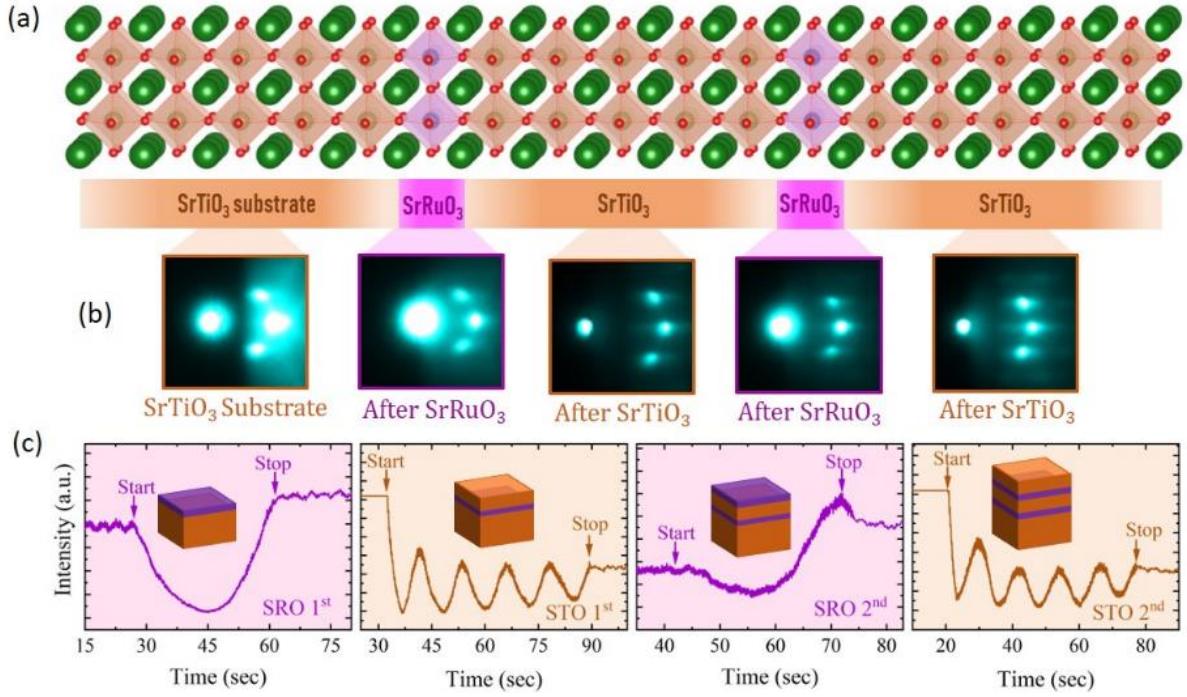

Figure 4.1. STO^5-SRO^1-STO^5 heterostructure: (a) schematic sketch, and (b) *In-situ* RHEED patterns of STO substrate, SRO, and STO sublayers. (c) Time-dependent RHEED intensity profile.

Electrical transport measurements. Electron transport measurements were performed via a Quantum Design Physical Property measurement system in a four-probe configuration. The magnetoresistance (MR) was measured at different temperatures by applying an external magnetic field along film normal.

Magnetometry. The samples magnetization was studied by using a Quantum Design Superconducting Quantum Interference Device Reciprocating Sample Option. The

magnetization as a function of temperature M(T) measurement was obtained via first cooling the samples down to 5 K under the 0.2 T field, and then while warming in presence of 0.01 T, the M(T) data was collected.

Scanning transmission electron microscopy (STEM) and electron energy loss spectroscopy (EELS). The structure and composition of the samples were investigated via atomic-resolution HAADF/ABF- STEM imaging and EELS mapping. STEM and EELS experiments were performed on a 200 kV JEOL ARM electron microscope at Brookhaven National Library equipped with double aberration correctors, a dual energy-loss spectrometer, and a cold field-emission source. TEM samples were prepared using a focused ion beam with Ga^+ ions followed by Ar^+ ions milling to a thickness of ~30 nm. The atomic-resolution STEM images were collected with a 21 mrad convergent angle (30 μm condenser aperture) and a collection angle of 67 – 275 mrad for high-angle annular dark-field (HAADF) and 11 – 23 mrad for annular bright-field (ABF) imaging. The atomic positions were obtained using two-dimensional Gaussian fitting following the maximum intensity.

The microscope conditions were optimized for EELS acquisition with a probe size of 0.8 Å, a convergence semi-angle of 20 mrad, and a collection semi-angle of 88 mrad. Dual EELS mode was used to collect low-loss and core-loss spectra simultaneously for energy drift calibration in the collecting process. EELS mapping was obtained across the whole film with a step size of 0.2 Å and a dwell time of 0.05 s/pixel. The EELS background was subtracted using a power-law function, and multiple scattering was removed by a Fourier deconvolution method.

4.3 Results and Discussions

4.3.1 Structure and Composition

The intensity in the HAADF image is roughly proportional to $Z^{\sim 2}$ (Z is an atomic number), depicting directly heavy-atom positions, whereas ABF imaging is useful for

visualization of lighter atoms such as oxygen. The STEM images of STO^5-SRO^1-STO^5 with two repeating blocks of single-u.c. SRO are shown in Figure 4.2.

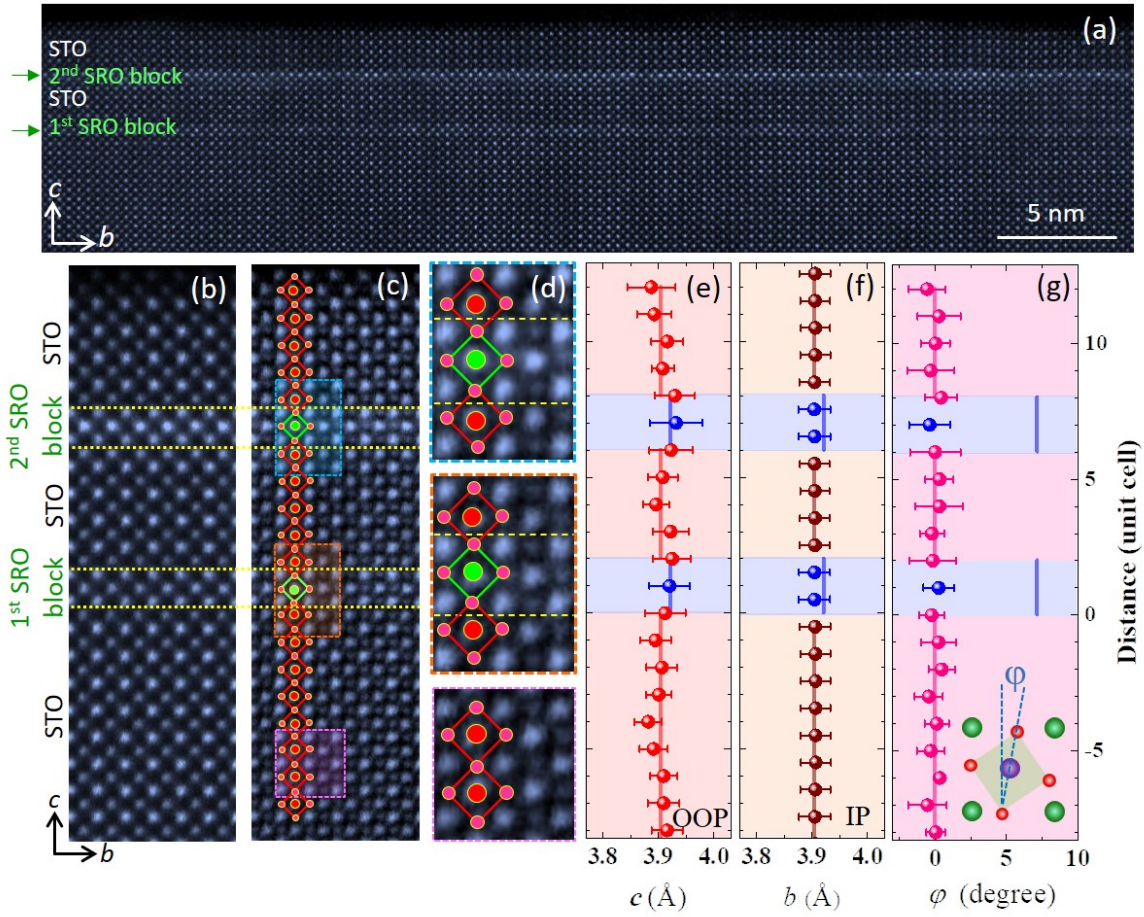

Figure 4.2. Atomically resolved structure of STO^5-SRO^1-STO^5 (with two single-u.c. SRO repeating blocks) viewed along the [100] direction: (a) large area HAADF-, (b) high magnification HAADF-, (c) intensity-inversed ABF, and (d) zoomed inversed ABF-STEM images. The dotted orange line marks the interface, whereas red and green squares in panel (c) signify the projected octahedral shapes in STO and SRO. (e) out-of-plane and (f) in -plane lattice parameter *c* and *b*, respectively, as a function of distance from the film-substrate interface. The error bar shows the standard deviations of the averaged measurements along the b-axis. The pseudocubic lattice parameters of bulk STO (3.905 Å) and SRO (3.925 Å) are indicated by a red and blue solid line, respectively. (g) Variation of projected octahedral tilt angle (φ). The definition of φ is specified in the inset. The solid blue line in panel (g) marks the φ in bulk SRO (~7.2°). No octahedra tilts across the interfaces are observed.

The individual Sr (Z = 38), Ru (Z = 44), and Ti (Z = 22) atoms could be distinguished based on intensity contrast [see Figure 4.2(a)-(d)], permitting us to determine the hetero-interfaces [see yellow lines in Figure 4.2(b)-(d)]. The HAADF-STEM images reveal that the

crystalline lattice is coherent across the interfaces in the entire heterostructure. Furthermore, it can be seen from the HAADF image that the Ru column in the 1st SRO block is darker than that in the 2nd SRO block, which is related to severe Ti-Ru intermixing as will be discussed later.

To quantitatively examine the lattice-mismatch-induced structural distortions, we determined the out-of-plane (OOP) and in-plane (IP) lattice parameters from A-site atomic positions [see Figure 4.2(e) and Figure 4.2(f)]. The IP lattice parameter (*b*) of the SRO/STO interlayer is consistent with the STO substrate [Figure 4.2(f)], indicating the sublayers are fully compressively strained (Bulk: a_{STO} =3.905 Å and a_{SRO} = 3.925 Å). The OOP lattice parameter (*c*) of the SRO blocks [Figure 4.2(e)] is nearly the same as that of STO, suggesting a cubic symmetry, but the octahedral volume is smaller (59.85 ± 0.09 $Å^3$) than the bulk SRO (~ 60.37 $Å^3$) value of RuO_6, which is associated with Ti-Ru intermixture (discussed later).

Furthermore, in the ABF image [see Figure 4.2(c)-(d)] of the STO^5-SRO^1-STO^5 heterostructure, oxygen columns are visible hence permitting us to determine the octahedral geometry. We have determined the projected octahedral tilt angle (φ) as a function of atomic distance [see Figure 4.2(g)]. The definition of φ is shown in the inset of Figure 4.2(g). The φ of SRO and STO interlayers are nearly constant (averaged $\varphi \approx 0.37° \pm 1.2°$) and comparable to the value of STO substrate ($\varphi \approx 0.27° \pm 1.07°$), suggesting that the RuO_6 octahedral tilt is completely suppressed, while the projected RuO_6 octahedra are illustrated with the red/green box in Figure 4.2(c)-(d).

The atomic-level view of the STO^5-SRO^2-STO^5 heterostructure with two 2-u.c. SRO repeating blocks is shown in Figure 4.3. The STEM images show coherent growth of the film where the two 2-u.c. SRO blocks are marked in Figure 4.3(a)-(d). Additionally, the trend of having a nearly constant IP lattice parameter (*b*) reiterates that the SRO/STO interlayers are epitaxially strained [Figure 4.3(f)], ensuring a high-quality heterostructure. The OOP lattice

parameter (*c*) of the STO layer follows its bulk value [Figure 4.3(e)], while the SRO blocks show increased OOP lattice parameter due to compressive strain, suggesting a tetragonal symmetry. This OPP lattice parameter (*c*) in 2-u.c. SRO blocks is also larger than that of monolayer SRO heterostructure [see Figure 4.2(e)], which will be discussed later.

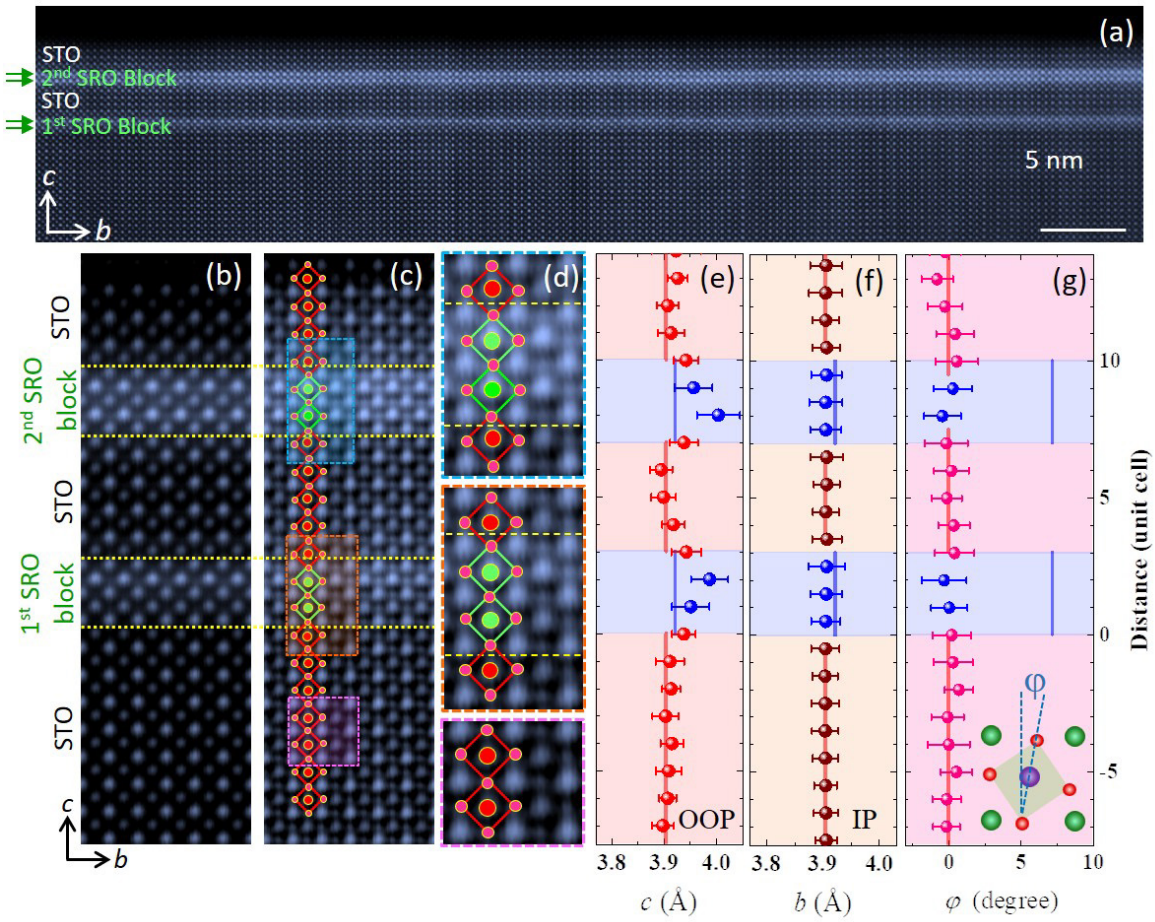

Figure 4.3. Atomically resolved structure of STO^5-SRO^2-STO^5 (with two single-u.c. SRO repeating blocks) viewed along the [100] direction: (a) large area HAADF-, (b) high magnification HAADF-, (c) intensity-inversed ABF, and (d) zoomed inversed ABF-STEM images. The dotted orange line marks the interface, whereas red and green squares in panel (c) signify the projected octahedral shapes in STO and SRO. (e) out-of-plane and (f) in -plane lattice parameter *c* and *b*, respectively, as a function of distance from the film-substrate interface. The error bar shows the standard deviations of the averaged measurements along the b-axis. The pseudocubic lattice parameters of bulk STO and SRO are indicated by a red and blue solid line, respectively. (g) Variation of projected octahedral tilt angle (φ). The definition of φ is specified in the inset. The solid blue line in panel (g) marks the φ in bulk SRO (~7.2°). No octahedra tilts across the interfaces are observed.

On the other hand, for the STO^5-SRO^2-STO^5 heterostructure, the SRO block maintain an

average octahedral tilt angle of $\varphi \approx 0.26° \pm 1.3°$ [as opposed to bulk SRO $\varphi \sim 7.2°$, see Figure 4.3(g)], whereas the observed φ of SRO interlayer is similar to the φ prevailing in the STO substrate ($0.25° \pm 1.15°$). Given that octahedral unit's preserve their connectivity via corner-shared oxygen atoms, the ultra-thin SRO confinement between cubic STO blocks facilitates the entire suppression of RuO_6 octahedral tilt angle, leading to stabilization of the artificially engineered bond angle of SRO [8,75,76].

To determine the possible B-site cation (Ti, Ru) intermixing in the heterostructures, we took and analyzed STEM/EELS maps from many areas of the samples. The results are presented in Figure 4.4. As shown in Figure 4.4(a)-(c), the Ti atoms diffuse significantly into the Ru sites in STO^5-SRO^1-STO^5, especially the first SRO block (i.e., a single RuO_2 layer), resulting in the low Ru column intensity in the HAADF image [see Figure 4.4(a)]. Quantitatively, the dopant Ti concentrations at the Ru sites were obtained from EELS profiles using the Lorentz-function-fitting method, with the Ti in the STO substrate as reference. We note a 61 ± 6 % Ti occupying the Ru site in the 1st (near substrate) SRO block and 25 ± 11% in the 2nd block of the STO^5-SRO^1-STO^5 heterostructure [see Figure 4.4(b)-(c)].

On the other hand, the EELS mapping results from two representative areas of STO^5-SRO^2-STO^5 [one shown in Figure 4.4(d)-(f) and the other in Figure 4.4(g)-(i), respectively] are rather different from STO^5-SRO^1-STO^5. Though, the Ti concentration is still significant and varies from one region to another in the RuO_2 layer proximal to STO substrate of the 1st SRO block [~10% or less as in Figure 4.4(f) to 60 % as in Figure 4.4(i)]. Nevertheless, few Ti ions ($\leq$10 %) diffuse into the second RuO_2 layer of the 1st SRO block or both RuO_2 layers of 2nd SRO blocks [see Figure 4.4(d)-(i)]. Overall, the spectroscopic observations suggest that the 2-u.c. SRO blocks in STO^5- SRO^2-STO^5 are nearly stoichiometric, while the single-u.c. SRO blocks in STO^5-SRO^1-STO^5 hold a higher Ru-cation off-stoichiometry due to interface intermixture.

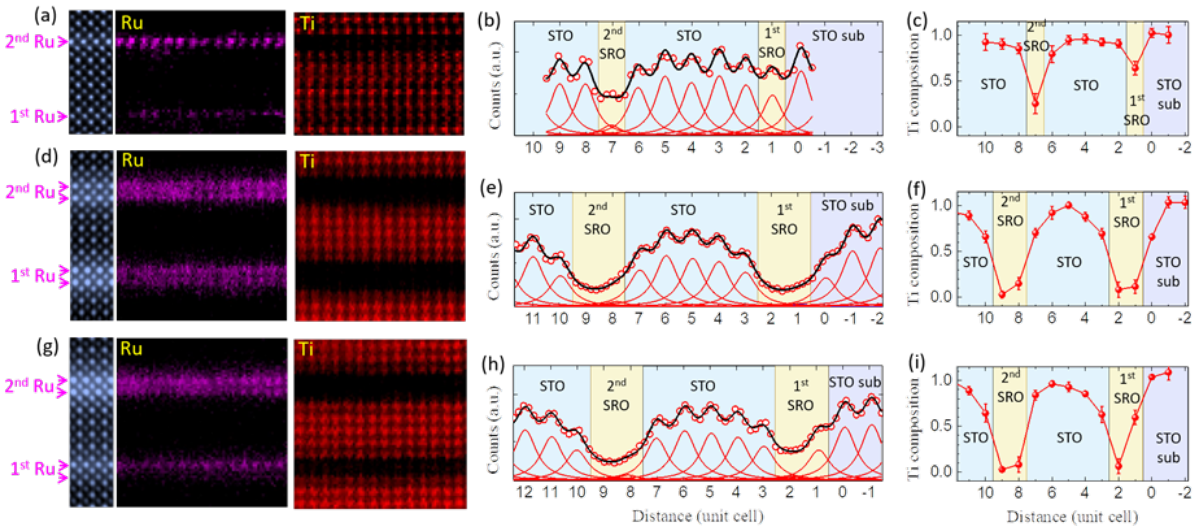

Figure 4.4. STEM/EELS maps and elemental concentration: (a) HAADF images and EELS elemental maps from Ti-$L_{2,3}$, and Ru-$M_{2,3}$ edges, (b) Least-squares fit of Ti EELS intensity profiles (red dots) from averaging the Ti maps over the horizontal direction in (a), and (c) Ti composition profiles across STO^5-SRO^1-STO^5 heterostructure. The black curve is a sum of the Lorentzian peaks fixed at the Ti lattice sites. The Lorentzian peaks indicate Ti concentration. The same arrangement of STEM/EELS characterization for two representative mapping areas of STO^5-SRO^2-STO^5 heterostructure, (d-f) and (g-i), respectively. The distance (in u.c.) is defined with respect to the film-substrate interface.

The substantial Ti atoms in the single-u.c. SRO blocks of the STO^5-SRO^1-STO^5 heterostructure bring the OOP lattice parameter (c) of SRO close to that of STO [Figure 4.2(e)]. Additionally, the RuO_6 octahedral volume is reduced (59.85 ± 0.09 Å^3) in comparison to the bulk SRO (~ 60.37 Å^3) (STO bulk volume: 59.45 Å^3). In contrast, owing to nearly stoichiometric Ru concentration, the SRO blocks in STO^5-SRO^2-STO^5 retain their bulk-like pseudocubic unit-cell nature. Because of the in-plane compressive strain, the RuO_6 in STO^5- SRO^2-STO^5 shows slight elongation in the c-axis [see Figure 4.3(e)] while maintaining RuO_6 octahedral volume (60.45 ± 0.19 Å^3) close to that in bulk SRO (~ 60.37 Å^3). In ultrathin oxide ABO_3 heterostructures, the interface B-site intermixture is unavoidable, irrespective of the growth method [77]. In fact, sensitivity of ruthenates to B-site disorder and volatile nature of Ru, makes it challenging to attain stoichiometric Ru films in the ultra-thin limit [78–80].

4.3.2 Resistivity

After a thorough understanding of the structure and composition, we proceed to investigate the transport and magneto-transport properties. Figure 4.5(a) shows sheet resistance as a function of the temperature of STO^5-SRO^n-STO^5 (n = 1, 2 u.c.) heterostructures. An insulating behavior of increasing resistance with lowering temperature is observed in STO^5-SRO^1-STO^5.

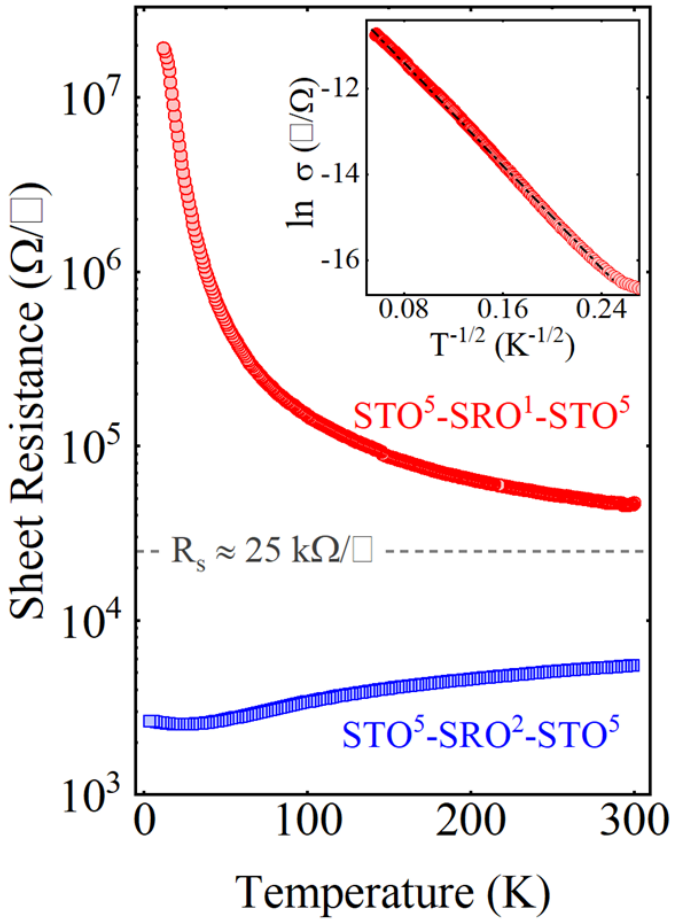

Figure 4.5. (a) Temperature-dependent sheet resistance of STO^5-SRO^n-STO^5 with n =1, 2. The inset shows a logarithmic plot of STO^5-SRO^1-STO^5 conductivity versus $T^{-1/2}$, representing the Efros-Shklovskii variable range hopping model. The grey dashed line is the quantum of resistance ($R_s \approx 25k\ \Omega/\square$).

Moreover, as shown in the inset of Figure 4.5(a), the transport of STO^5-SRO^1-STO^5 can be fitted nicely with Efros-Shklovskii variable-range hopping model, where conductivity

follows: $\sigma(T) = \sigma_0 e^{(T_{ES}/T)^{1/2}}$ ($T_{ES} = \beta_{ES}\, e^2/\varepsilon\, k_B\, \xi$ is a characteristic temperature, ξ is localization length, *e* elementary charge, ε dielectric constant [81,82]. The linear fitting of data yields $T_{ES} \approx$ 900 K, signifying the disorder-induced strong localization due to the Ti-Ru intermixture is likely the primary driving force for the insulating behavior. In the presence of strong localization effects, the kinetic theory of conductivity ($\sigma = e^2 k_F l/h$, where k_F is Fermi wave vector, and *l* is mean free path) breaks down, since the electronic mean free path (*l*) turn out to be equal to lattice spacing ($l \approx a$), leading to $k_F l \approx 1$, and system crosses the minimum metallic conductivity known as the Ioffe-Regel limit [83,84], where the sheet resistance limit is: $R_s = h/e^2 \approx 25\ k\Omega/\square$. Figure 4.5(a) confirms that the STO^5-SRO^1-STO^5 heterostructure sheet resistance exceeds the Ioffe-Regel limit in the measured temperature range. On other hand, the STO^5-SRO^2-STO^5 heterostructure shows the metallic character in the measured temperature range. Though, the small resistivity upturn below ~25 K is observed, mainly caused by the disorder-induced weak localization effects [54,63,85].

4.3.3 Magneto-resistance

We have performed magnetoresistance (MR) measurements; MR = $\{\rho(H) - \rho(0)\}/\rho(0)$, here $\rho(H)$ and $\rho(0)$ are resistivities in the presence and absence of a magnetic field, respectively (the external magnetic field *(H)* is perpendicular to the film plane). The MR of STO^5-SRO^1-STO^5 shows a parabolic nature [see Figure 4.6(a)], signifying an absence of FM order. In contrast, the MR of STO^5-SRO^2-STO^5 shows a butterfly loop MR, representing the FM state [see Figure 4.6 (b)]. The maximum (~ 2 T) in the MR at 5 K hysteretic curve corresponds to coercive field H_c, whereas the point of forward and backward sweeps overlapping is the saturation field (~6 T). The hysteretic MR characteristic of FM ordering persists up to ~55 K, though non-parabolic MR dependence continues up to ~120 K. For manganite's [86–89], granular magnetic systems [90,91], and SRO [92], the MR scales as

MR $\propto [M(H)/M_S]^2$, while MR $\propto [\mu_0 H]^2$ for nonmagnetic-conducting systems [74,90,93], where M_S is saturation magnetization and H the applied field.

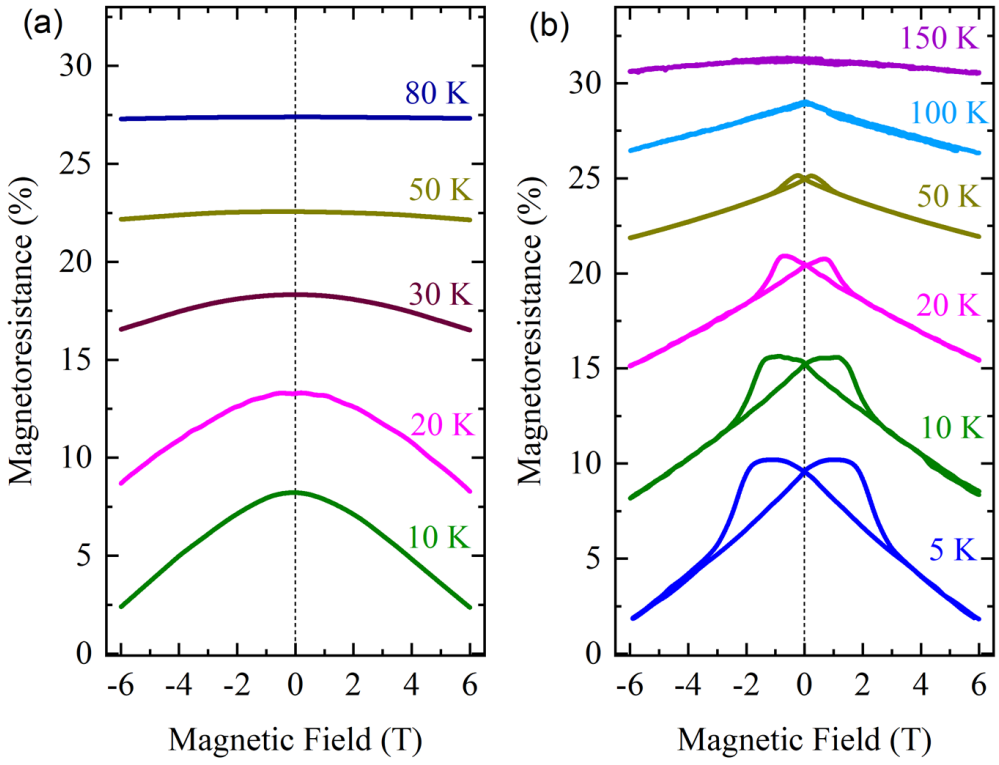

Figure 4.6. Magnetoresistance of (a) STO^5-SRO^1-STO^5, and (c) STO^5-SRO^2-STO^5 measured at different temperatures.

The magnetoresistance dependence on the magnetization (MR $\propto M^2$) suggests that electron transport depends on the magnetic moment's alignment within magnetic domains. As the magnetic moments are aligned, the carrier scattering decreases and so is the resistivity, while the resistivity is maximized at the coercive fields. Yet, trapping centers such as dislocations, defects, and non-magnetic inhomogeneity, might cause the pinning of domain walls, leading to enlarged switching fields. Moreover, the disappearance of the butterfly loop before the actual T_C is triggered by the dominance of thermal fluctuations over the pinning of domain walls. Nonetheless, the presence of a butterfly-like feature in the MR below 55 K corroborates the presence of FM ordering in STO^5-SRO^2-STO^5, while the single-u.c. SRO is non-FM.

4.3.4 Magnetic Characterization

The magnetization of STO^5-SRO^n-STO^5 (n = 1, 2 u.c.) heterostructures was also studied via SQUID magnetometry. To measure magnetization as a function of temperature $M(T)$, the samples were first cooled down to 5 K under the 0.2 T field, and then while warming in presence of 0.01 T, the data was collected.

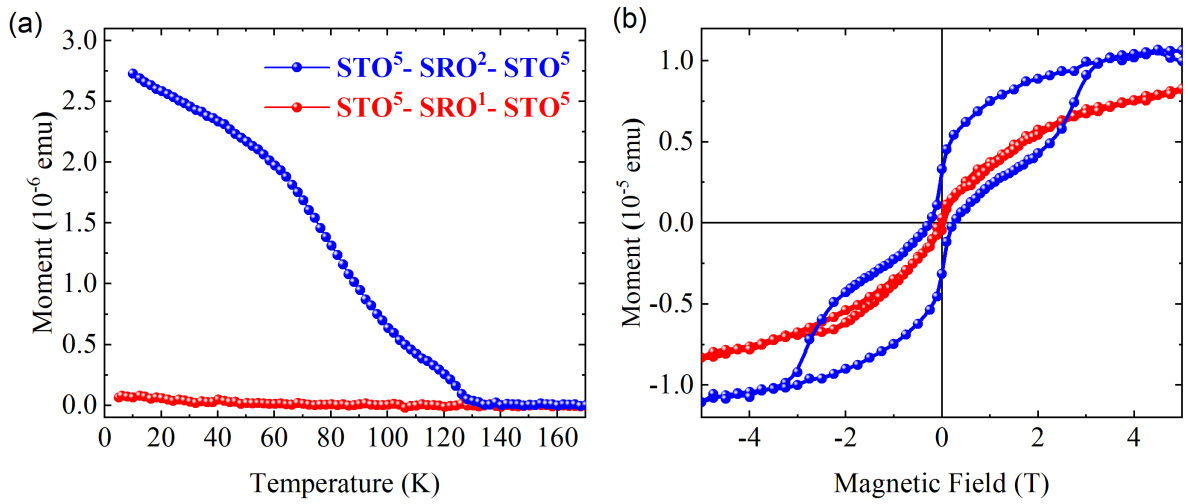

Figure 4.7. STO^5-SRO^n-STO^5 [n = 1, 2] (a) Temperature-dependent magnetization, and (b) magnetic hysteresis measured at 5 K.

The STO^5-SRO^1-STO^5 does not show any sign of FM transition, as the $M(T)$ curve is nearly flat [see Figure 4.7(a)], and the $M(H)$ is reminiscent of background hysteresis of the substrate [see Figure 4.7(b)], verifying the absence of FM state. However, STO^5-SRO^2-STO^5 exhibits robust FM ordering as shown by sharp paramagnetic to FM transition at $T_C \sim 128$ K in $M(T)$ [Figure 4.7(a)] and characteristic ferromagnetic hysteresis [see $M(H)$ in Figure 4.7(b)]. Overall, the electron transport and magnetic properties results indicate that the presence of metallicity is important for stabilizing ferromagnetism since an insulating SRO is non-magnetic.

4.3.5 Density Functional Calculations of Intrinsic and Extrinsic Heterostructures

In order to better understand the magnetic and electronic nature of the present heterostructures, we have performed DFT calculations on STO^5-SRO^n-STO^5 (n = 1,2 u.c.)

heterostructures. The DFT calculations were performed by Andrew O'Hara, Donghan Shin under guidance of Sokrates T. Pantelides at Department of Electrical Computer Engineering, Vanderbilt University, Nashville, Tennessee 37235, USA.

The electronic structure of bulk $SrRuO_3$ (SRO) according to Rondinelli et al. [13] is best described by including electron-electron correlations in the form of a Hubbard term with U = 0.6 eV. For Hubbard U values > 2 eV, in bulk, SRO becomes half-metallic [13,14,94]. For SRO ultra-thins films, theoretical calculations even with U > 3 eV are incapable to reproduce the observed insulating-nonmagnetic state [13]. Due to these observations, Rondinelli et al. [13] concluded that the insulating-nonmagnetic state is not caused by intrinsic changes such as enhanced electron interactions or structural changes, but rather triggered by surface roughness, defects, or disorder. However, according to Verissimo et al. [68], the single layer of Ru confined between STO lattice is a minority-spin half-metallic ferromagnet with U = 4 eV. Furthermore, recent calculations using a Hubbard U of 3.5 eV produced the most reasonable results for few-layer SRO films sandwiched between $BaTiO_3$ in thin-film heterostructures [67]. Therefore, we adopted Hubbard U = 3.5 eV in the present study of the STO^5-SRO^n-STO^5 heterostructures. Variation of the effective Hubbard U by ±0.5 eV does not change the qualitative results when tested on the stoichiometric STO^5-SRO^1-STO^5 heterostructure (i.e., it remains a ferromagnetic metal).

The structural calculations reveal that both the STO^5-SRO^1-STO^5 and the STO^5-SRO^2-STO^5 heterostructures feature non-tilted octahedra in the SRO layers, in accord with the STEM data. Thus, both experiments and theory rule out structural distortions to be the regulatory factor for the observed contrasting electro-magnetic properties in the two heterostructures. Beginning with the STO^5-SRO^1-STO^5 system, there are three possible magnetic arrangements for the Ru spins as shown in Figure 4.8(a) FM, Figure 4.8(b) checkerboard AFM (AFM1), and Figure

4.8(c) striped AFM (AFM2). The FM order is the ground state by 53 meV per Ru atom. In this FM state, the SRO layer in the STO^5-SRO^1-STO^5 system is half-metallic, namely metallic in only the minority-spin polarized electrons, while a gap appears between the spin-up t_{2g} and e_g states [see Figure 4.8(a)].

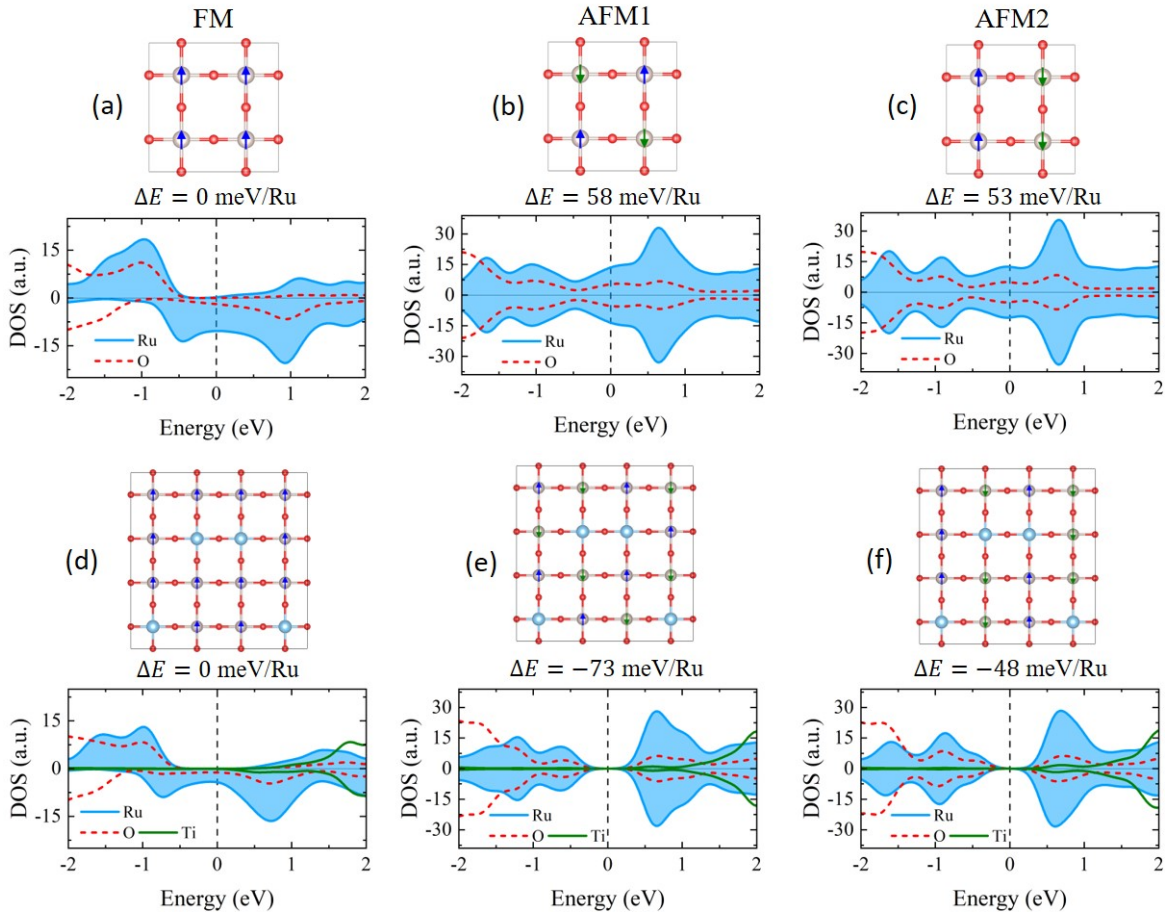

Figure 4.8. Magnetic arrangements (top) and projected density of states (bottom) for the RuO_2 planes in STO^5-SRO^1-STO^5 heterostructures. Panels (a) through (c) are for a heterostructure containing a stoichiometric RuO_2 plane. Panels (d) through (f) are for 25% substitution of Ti for Ru within the RuO_2 plane. All densities of states are normalized to the same lateral system size so that they can be compared.

In contrast, both the higher-energy AFM phases are metallic as shown by the density of states in Figure 4.8(b)-(c). The FM metallic ground state results are consistent with prior literature [68,69] and indicate that the observed non-FM insulating state is likely due to extrinsic effects and is not an intrinsic property of the system [13]. As demonstrated by the STEM results

in of STO^5-SRO^1-STO^5 heterostructure, the 1st SRO and 2nd SRO blocks contain 61 ± 6 % to 25 ± 11% Ru deficiency by Ti-for-Ru substitution, respectively. Therefore, from the original STO^5-SRO^1-STO^5 heterostructure model, we constructed a lateral heterostructure containing 16 Ru sites and replace four of them with Ti to achieve 25% Ru deficiency via substitution. The chosen arrangement shown in Figure 4.8(d)-(f) allows consideration of the same basic FM and AFM arrangements as before. We find that the introduction of the Ti leads to the energetic stabilization of both AFM arrangements relative to the FM solution. Furthermore, as seen in the density of states plots of Figure 4.8(d)-(f), the introduction of Ti within the RuO_2 layer leads to shifts in the oxygen/transition-metal hybridization and opens a bandgap of 0.4 eV for both AFM orderings. Thus, we can conclude that the introduction of Ti within the RuO_2 layer via interfacial intermixture observed in STEM is responsible for the observed magnetic and electronic properties. This result complements the report by Boschker and co-workers [74], where using adsorption-controlled molecular-beam epitaxy, the SRO in monolayer limit is unveiled to hold metallicity and FM order, echoing the importance of the role of interface-induced intermixing and impurities in determining heterostructure properties [77,79,80,95]. Although other Ti-for-Ru substitutional patterns are possible, these calculations become prohibitively expensive with current methods. For this reason, we did not explore if a critical percent substitution of Ti-for-Ru exists that can maintain FM and metallicity. Nevertheless, if defects are eradicated, a metallic-FM monolayer SRO could be stabilized [74].

For the STO^5-SRO^2-STO^5 heterostructure, we consider four possible AFM arrangements [see the top of Figure 4.9(a)] based on the prior single layer AFM arrangements (with differing coupling along the c-axis of the heterostructure) as well as an additional arrangement (AFM7) which has FM ordering within each plane. For AFM3 through AFM6, the total relative energy per Ru atom is much higher than the FM order compared to the stoichiometric STO^5-SRO^1-STO^5

case. The AFM7 case is also found to be higher in energy than the FM ordering, but is lower than the other STO^5-SRO^2-STO^5 energies since only the interlayer exchange coupling energy plays a role in the ΔE. As expected, the density of states for the layers [see Figure 4.9(b)] remains metallic like the stoichiometric STO^5-SRO^1-STO^5 structure and consistent with the experimental results.

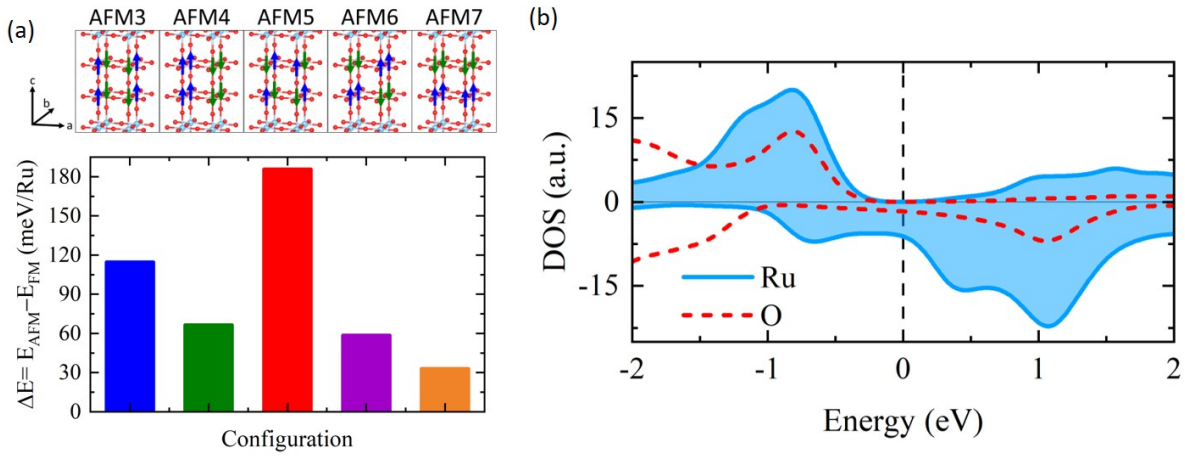

Figure 4.9. (a) Possible AFM arrangements for the Ru sublattice in the STO^5-SRO^2-STO^5 heterostructure and their relative energy per Ru atom compared to the FM ground state. (b) Density of states for the lower RuO_2 plane in the STO^5-SRO^2-STO^5 heterostructure.

4.4 Conclusion

In conclusion, by fabricating artificial heterostructures of the form STO^5-SRO^n-STO^5 (n = 1, 2 u.c.), we have shown that the heterostructure with 2-u.c. SRO is metallic and FM (T_C ~ 128 K) while the heterostructure with single-u.c. SRO is insulating and non-FM. There is no fundamental change in lattice structure with reducing the thickness of SRO, thus excluding structural modification as a controlling factor for such drastic property transitions. DFT results further suggest that a stoichiometric single-u.c. STO^5-SRO^1-STO^5 heterostructure would be FM and metallic. However, we observed that SRO in STO^5-SRO^1-STO^5 is non-stoichiometric, exhibiting a much greater amount of Ti in the SRO blocks due to Ti-Ru intermixture than in the STO^5-SRO^2-STO^5 heterostructure. The existence of these non-magnetic Ti impurities in single-

u.c. SRO drastically affects the electronic structure as well as the coherence for FM ordering. Therefore, we conclude that it is the off-stoichiometry dictated by the Ti-Ru intermixture that leads to the insulating and non-FM behavior of SRO in the single u.c. thickness limit. The experimental data of References [68,69,74] that find the single-unit-cell SRO film to be FM confirms our overall conclusions about both STO^{5}-SRO^{1}-STO^{5} and STO^{5}-SRO^{2}-STO^{5} heterostructures.

Chapter 5. Emergent Ferromagnetism and Insulator-Metal Transition in Ruthenates

Heterostructures of complex transition metal oxides are known to induce extraordinary emergent quantum states that arise from broken symmetry and other discontinuities at interfaces. Here we report the emergence of unusual, thickness-dependent properties in ultrathin $CaRuO_3$ films by unique insertion of a single isovalent SrO layer (referred to as "δ-doping"). While bulk $CaRuO_3$ is metallic and nonmagnetic, films thinner than or equal to ~15-unit cells (u.c.) are insulating though still nonmagnetic. However, δ-doping to middle of such $CaRuO_3$ films induces an insulator-to-metal transition and evolution of Griffiths phase to unusual ferromagnetism with strong magnetoresistive behavior. Atomically resolved imaging and density-functional-theory calculations reveal that the whole d-doped film preserves the bulk-$CaRuO_3$ orthorhombic structure, while appreciable structural and electronic changes are highly localized near the SrO layer. The results highlight delicate nature of magnetic ordering in $CaRuO_3$ and subtle effects that can alter it, especially the role of A-site cation in electronic and magnetic structure additional to lattice distortion in ruthenates. It also provides a practical approach to engineer material systems via highly localized modifications in their structure and composition that may offer new routes to the design of oxide electronics.[2]

5.1 Introduction

Complex-oxide heterostructures have been established as an effective engineering platform offering prospects to create tunable electro-magnetic functionalities, enabled by manipulation of the cooperative interplay between electronic spin, charge, orbital, and lattice degrees of freedom. [48,96] The stacking of different oxides disturbs the subtle equilibrium

[2] This work is published as a preprint: https://doi.org/10.21203/rs.3.rs-1729136/v1

among various interactions, leading to a wealth of exotic quantum states, such as two-dimensional electron or hole gas at the interface of two insulating materials; $LaAlO_3/SrTiO_3$ (LAO/STO) [51,97], the spontaneous magnetic reversal in $La_{2/3}Sr_{1/3}MnO_3$ films [98], a ferromagnetic (FM) interface between nonmagnetic constituents [47,99], polar magnetic metal phase in $BaTiO_3/SrRuO_3/BaTiO_3$ heterostructures [67], chiral ferromagnetism in $SrRuO_3$ films [52], and strain-induced superconductivity in RuO_2 films. [53] The continued advancements in thin-film synthesis have made possible the fabrication of complex-oxide layers down to extremely thin limits with atomic precision, providing fine control over different lattice structures and paving the pathway to observe unusual quantum states.

The two ABO_3 4*d* perovskite-structure ruthenates: $CaRuO_3$ (CRO) and $SrRuO_3$ (SRO), despite having similar structure and electron counting, present unusual contrast in their physical properties. SRO is a strong Stoner metallic ferromagnet [9,100], while CRO, though a metal [100], lacks long-range magnetic order. [29,101,102] Extensive experimental and theoretical studies led to lively debates on the origin of the contrasting behavior, though the most likely explanation is that the impact of replacing Sr with Ca in SRO is indirect. The smaller ionic radius of Ca (2.31 Å versus 2.55 Å for Sr) leads to different octahedral Ru-O-Ru bond angles that result in subtle changes of the Fermi-energy density of states (DOS). [13–15]

Thin films of CRO and SRO also exhibit distinct properties, depending on temperature, film thickness, substrate strain, as well as film stoichiometry. Relatively thick CRO films grown on STO (001) have been reported to be metallic [103], yet under similar epitaxial strain, an insulating CRO phase can emerge below a certain critical thickness [104,105], which depends on growth conditions and is much larger than the critical thickness (2-3 u.c.) for similar behavior by SRO films. [56,58,63] At present, the intrinsic critical thickness of stoichiometric CRO films is not known. In addition, theoretical calculations predicted that tensile epitaxial strain can drive

CRO to a FM state, yet experimental confirmation is lacking. [24,26] Moreover, cation substitution at Ru sites by defects/dopants has also attracted considerable attentions as a way to induce FM order in CRO, suggesting an extremely fragile ground state. [21–23,106–108] Therefore, the delicate nature of incipient ferromagnetism in CRO suggests that one can manipulate CRO thin films in unique ways to obtain unusual, even unexpected electro-magnetic properties.

The present work focuses on ultrathin CRO films, which we perturb by inserting a single SrO layer (thus, mimicking a single-u.c. SRO or δ-doping [75,109]) in the middle of the films, all fabricated with atomic precision. Combining magneto-transport measurements, atomically resolved imaging by scanning transmission electron microscopy (STEM), and electron energy-loss spectroscopy (EELS), along with density-functional-theory (DFT) calculations, we reveal a thickness-dependent metal to insulator transition (MIT) with no sign of long-range magnetic ordering in pristine CRO films. As the thickness reaches 15 or fewer u.c., the films become insulating. However, the insertion of a single SrO layer not only triggers an insulator-to-metal transition in 15 u.c. CRO films and enhances the conductivity of thicker films, but also drives the studied thin films (15-40 u.c.) toward emergent Griffith's phase and unusual ferromagnetism. Atomic-resolution imaging and DFT calculations reveal that SRO-layer insertion preserves the orthorhombic symmetry, and the structural and electronic changes are largely confined near the insertion layer. Our results underline the fragile nature of the magnetic properties and likely the electronic structure of CRO by which a highly localized modification is able to tip the delicate balance for both transport and magnetic ordering in the system.

5.2 Results and Discussions

5.2.1 Heterostructure Synthesis

The $SrTiO_3$ (STO) (5 mm × 5 mm × 0.5 mm) substrates with (001) surface was chosen

for the fabrication of heterostructures. We have fabricated epitaxial 15-u.c. CRO (CRO^{15}), 20-u.c. CRO (CRO^{20}), and 40-u.c. CRO (CRO^{40}) films on STO (001) substrates, and corresponding δ-doped CRO films containing a localized SrO layer nested in the middle, i.e., CRO^{7}-SrO-CRO^{8}, CRO^{10}-SrO-CRO^{10}, and CRO^{20}-SrO-CRO^{20}.

The STO substrates were initially sonicated in deionized water, followed by a 30 seconds treatment in the buffered hydrogen fluoride. After chemical etching, the substrates were annealed at 950° C in a flowing oxygen atmosphere to create atomically smooth surfaces. $CaRuO_3$ (CRO) film with a thickness of 40, 20, and 15 u.c. were grown by pulsed laser deposition (PLD) at 700° C with an oxygen pressure of 100 mTorr. The δ-doping of SrO was achieved from $SrRuO_3$ (SRO) target at a growth temperature of 700° C and oxygen pressure of 100 mTorr. A KrF excimer laser (λ = 248 nm) with a 10 Hz repetition rate, and with energy 350 and 300 mJ was focused on CRO and SRO targets, respectively. After growth, samples were cooled down at ~11°/min to room temperature in an oxygen atmosphere of 100 mTorr.

In-situ reflective high energy electron diffraction (RHEED) has been applied to monitor the growth of the heterostructures in this study. Figure 5.1 displays the RHEED images of both the substrate and CRO films and the RHEED spot intensities vs. growth time, reflecting the typical growth pattern of ruthenate perovskites. The RHEED image of STO substrate before deposition shows high-intensity specular spots and Kikuchi lines, verifying high substrate quality. Both time-dependent intensity profile of RHEED (0,0) spot and streaky RHEED pattern after film growth point to a flat crystalline surface having two-dimensional growth. The RHEED patterns of the CRO films possess an additional diffraction spot as marked yellow arrows. This half-order spot in CRO is an indicator of octahedral tilt/rotations, originating from unit cell doubling in bulk CRO because of orthorhombic octahedral distortions.

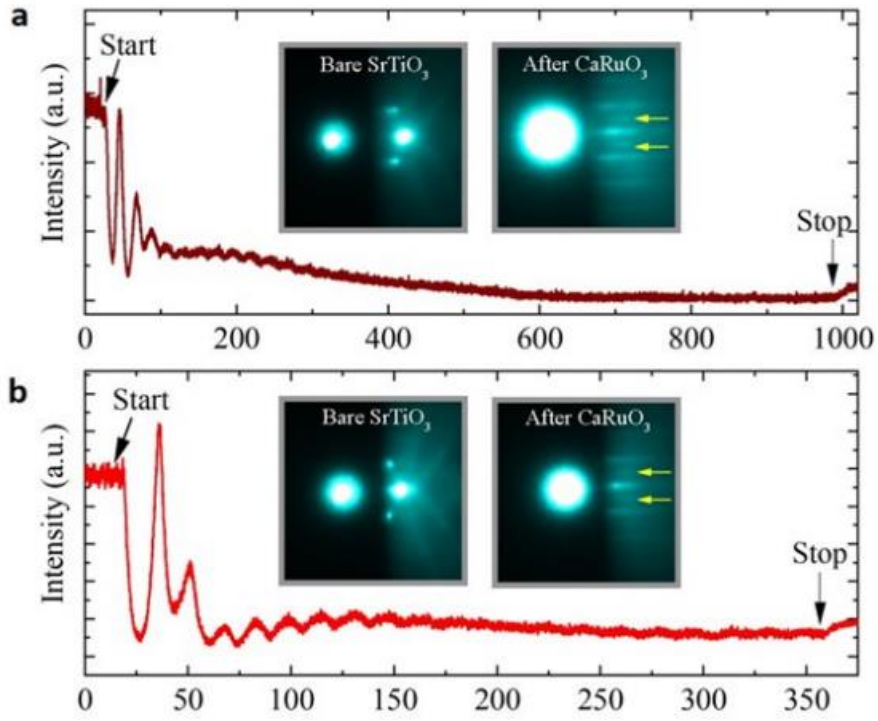

Figure 5.1. In-situ reflective high energy electron diffraction (RHEED) oscillations of (a) 40 u.c., and (b) 20 u.c. CRO films. The insets show RHEED patterns of bare STO substrate and after CRO film growth.

The X-ray diffraction was performed on a PanAlytical X'Pert thin-film diffractometer with Cu Kα−1 radiation with a single-crystal monochromator. Figure 5.2(a) shows a coupled (θ-2θ) scan around STO) $(001)_{pc}$ Bragg's reflection for 40 u.c. CRO film. We can perceive substrate and film peaks along with Laue interference fringes, confirming the good crystallinity of thin films. The measured out-of-plane (OP) pseudocubic lattice parameter of CRO film from Bragg's peak is ~3.83 Å. This is consistent with the fact that the OP parameter decreases (bulk pseudo-cubic CRO OP ~3.85 Å) to accommodate the lattice mismatch due to tensile strain. Moreover, the FWHM of film and substrate indicates high crystallinity [see Figure 5.2(b-c)]. The film is fully strained to the substrate as $Q_{\|}$ of film and substrate is identical as shown in Figure 5.2(d). Moreover, the core-level spectra are indicative of high-quality film epitaxy, and optimal film stoichiometry [see Figure 5.2(e-g)].

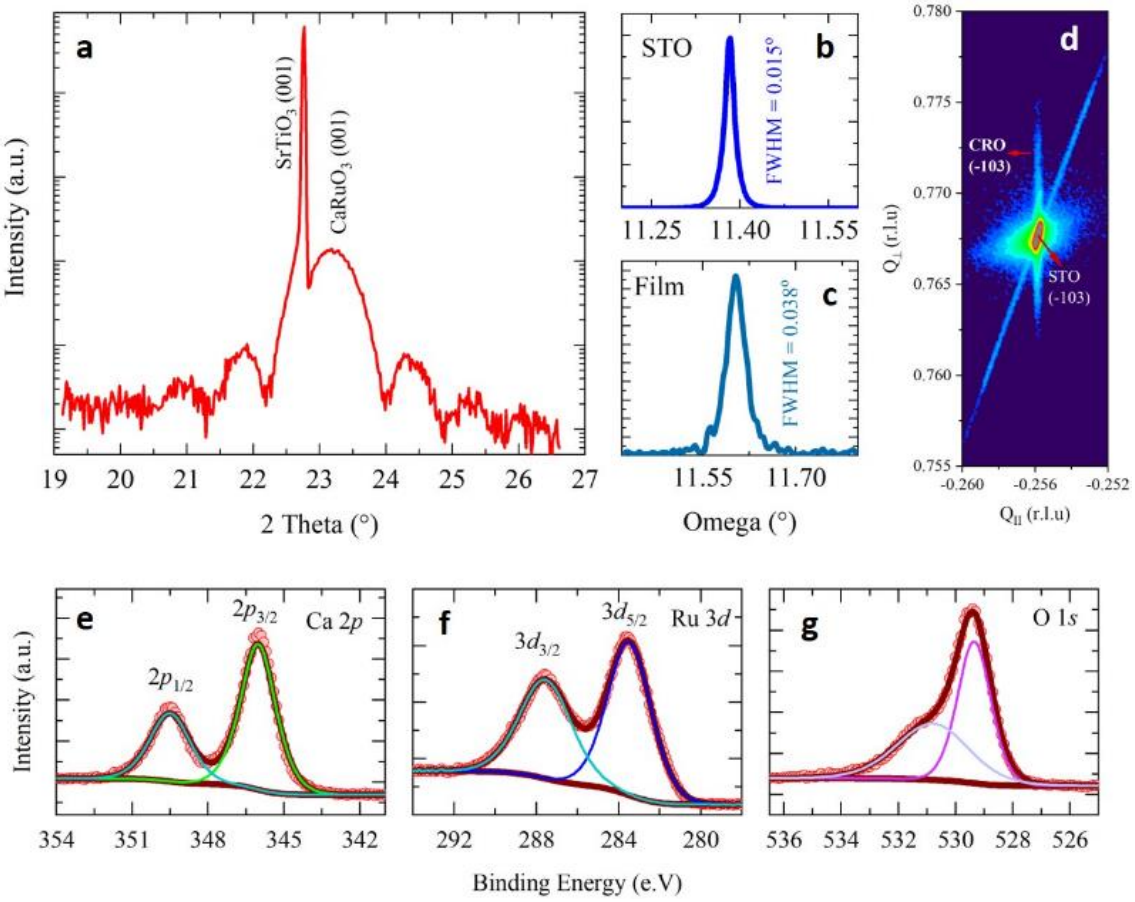

Figure 5.2. Coupled symmetric (θ-2θ) XRD scan of 40 u.c. CRO film. The presence of thickness fringes confirms high-quality hetero-interface and film surface. (b)-(c) Rocking curve around substrate/film $[001]_c$ and film. (d) Reciprocal space mapping (RSM) around (-103) of STO substrate. X-ray photoelectron spectroscopy (XPS) for the (e) Ca 2*p*, (f) Ru 3*d* core levels, and (g) O 1*s* spectra for 40 u.c. CRO film.

5.2.2 Atomically-Resolved Structure and Chemistry

We performed scanning transmission electron microscope (STEM) and Electron energy loss spectroscopy (EELS), whereas the results were attained via 200 kV JEOL ARM electron microscope at Brookhaven National Library equipped with double aberration correctors, a dual energy-loss spectrometer, and a cold field emission source. Cross-sectional TEM samples were thinned using a focused ion beam with Ga + ions followed by Ar + ions milling down to sample thickness of 30 nm.

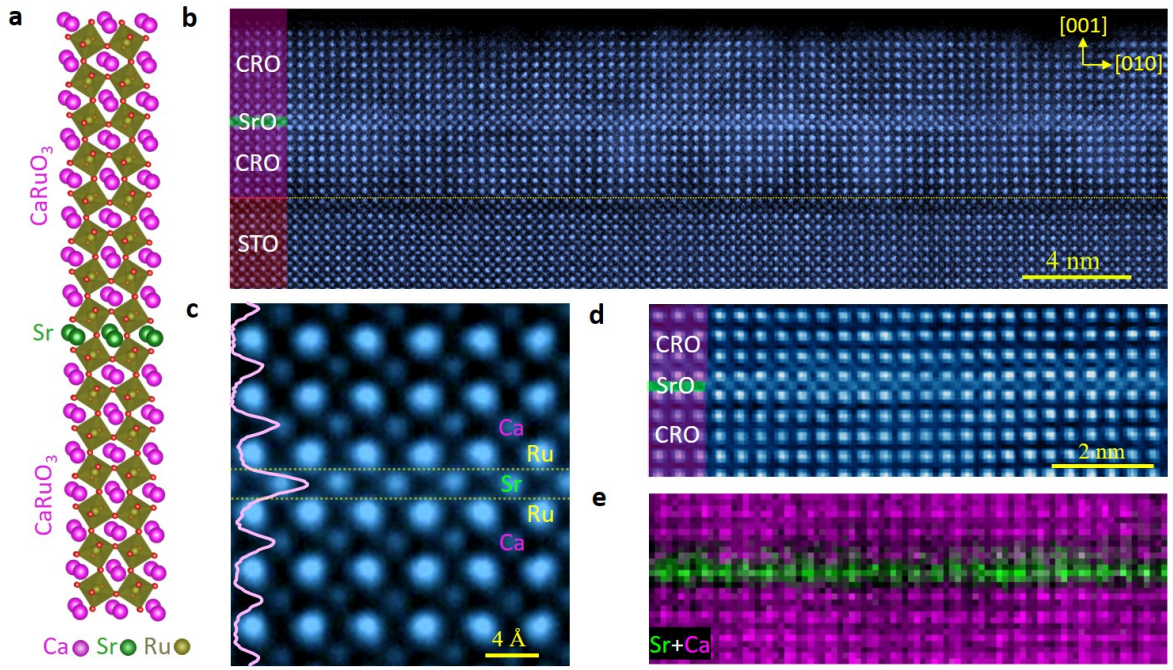

Figure 5.3. (a) Schematic of the nested SrO δ-doping in $CaRuO_3$. Atomic-resolution HAADF-STEM images of δ-doped CRO^7-SrO-CRO^8 heterostructure: (b) large-area, and (c) high magnification one with superimposed intensity profiles of Ca/Sr layer. (d) ADF image and (e) corresponding EELS map for Ca (purple) and Sr (green) cations. The electron beam is along the [100] direction of the STO substrate.

We have fabricated epitaxial 15-u.c. CRO (CRO^{15}), 20-u.c. CRO (CRO^{20}), and 40-u.c. CRO (CRO^{40}) films on $SrTiO_3$ (001) substrates, and corresponding δ-doped CRO films containing a localized SrO layer nested in the middle, i.e., CRO^7-SrO-CRO^8, CRO^{10}-SrO-CRO^{10}, and CRO^{20}-SrO-CRO^{20}. Figure 5.3(a) shows a schematic of the CRO^7-SrO-CRO^8 heterostructure while Figure 5.3(b-d) and Figure 5.4 display the atomically resolved structure of the same system for several different regions. It is apparent from the STEM image that the heterostructure is uniform with coherent and high-quality hetero-interfaces [see Figure 5.3(b-d), and Figure 5.4]. In Z-contrast HAADF images, Sr (Z = 38) columns appear brighter than Ca (Z = 20), whereby a uniform and homogeneous single Sr layer is observed clearly in Figure 5.3(c) and Figure 5.4(a-c). Furthermore, the EELS elemental maps of Ca (purple) and Sr (green) [see Figure 5.3(e) and Figure 5.4(b-c)] confirm that Sr is confined within a single layer with minimal if any

intermixing, establishing that nested SrO is a monolayer. The intermixture between Ca and Sr is very minimal. One interesting observation is that Sr is more likely to diffuse to the top CRO rather than the bottom layer [see the EELS maps in Figure 5.4(b-c)].

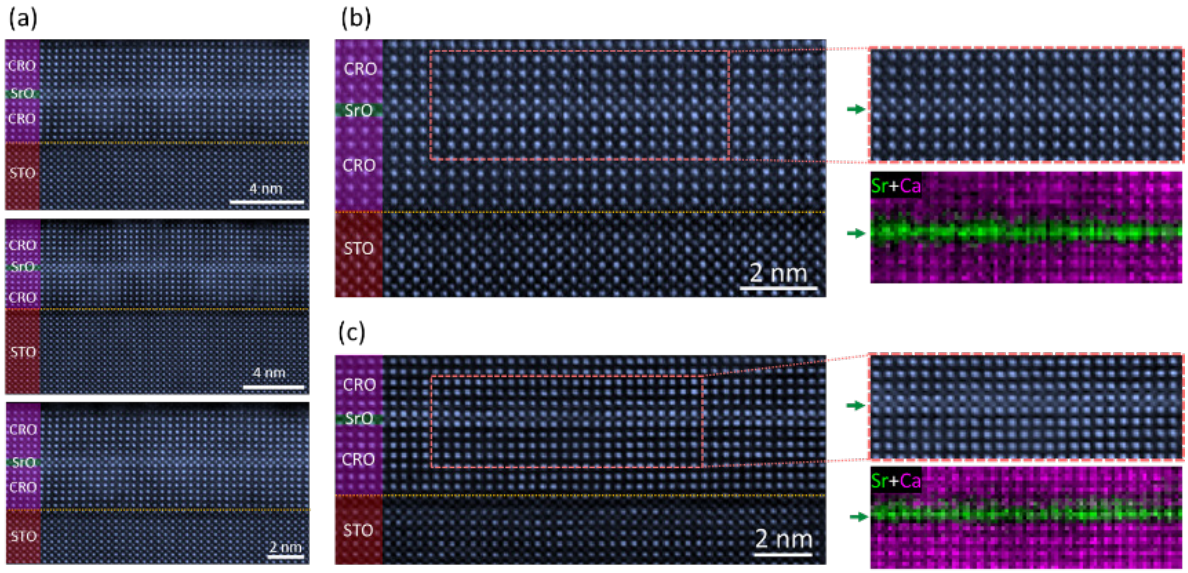

Figure 5.4. (a) Atomic-scale structure of δ-doped CRO[7]-SrO-CRO[8] heterostructure by STEM across three different regions. (b)-(c) Annular dark-field STEM image and corresponding EELS map for Ca (purple), and Sr (green) from the marked rectangular area. In the large area STEM-imaging, the brighter Sr -atomic monolayer could be observed. Furthermore, the unintegrated EELS map of the region with purple for Ca, and green for Sr establishes Sr is confined to single layer.

To quantitatively examine the lattice mismatch of CRO[7]-SrO-CRO[7] with the $SrTiO_3$ substrate, we have determined both the in-plane (IP) and out-of-plane (OP) lattice parameters from A-site atomic positions in high-angle annular dark-field (HAADF) imaging mode [see]. The measured IP pseudocubic lattice parameter (b) of film as shown in Figure 5.5(a) is matching well the STO substrate bulk (a_{STO} = 3.905 Å), confirming coherently strained film. On the other hand, the OP lattice parameter of CRO inter-layers is nearly the same as that of CRO bulk, while an appreciable dip could be observed in the layers adjacent to SrO, suggesting the presence of highly localized structural distortion [see Figure 5.5(b)]**.** Moreover, the TiO_6 interfacial layers in the STO side undergo an OP elongation due to large an octahedra mismatch of RuO_6 and TiO_6.

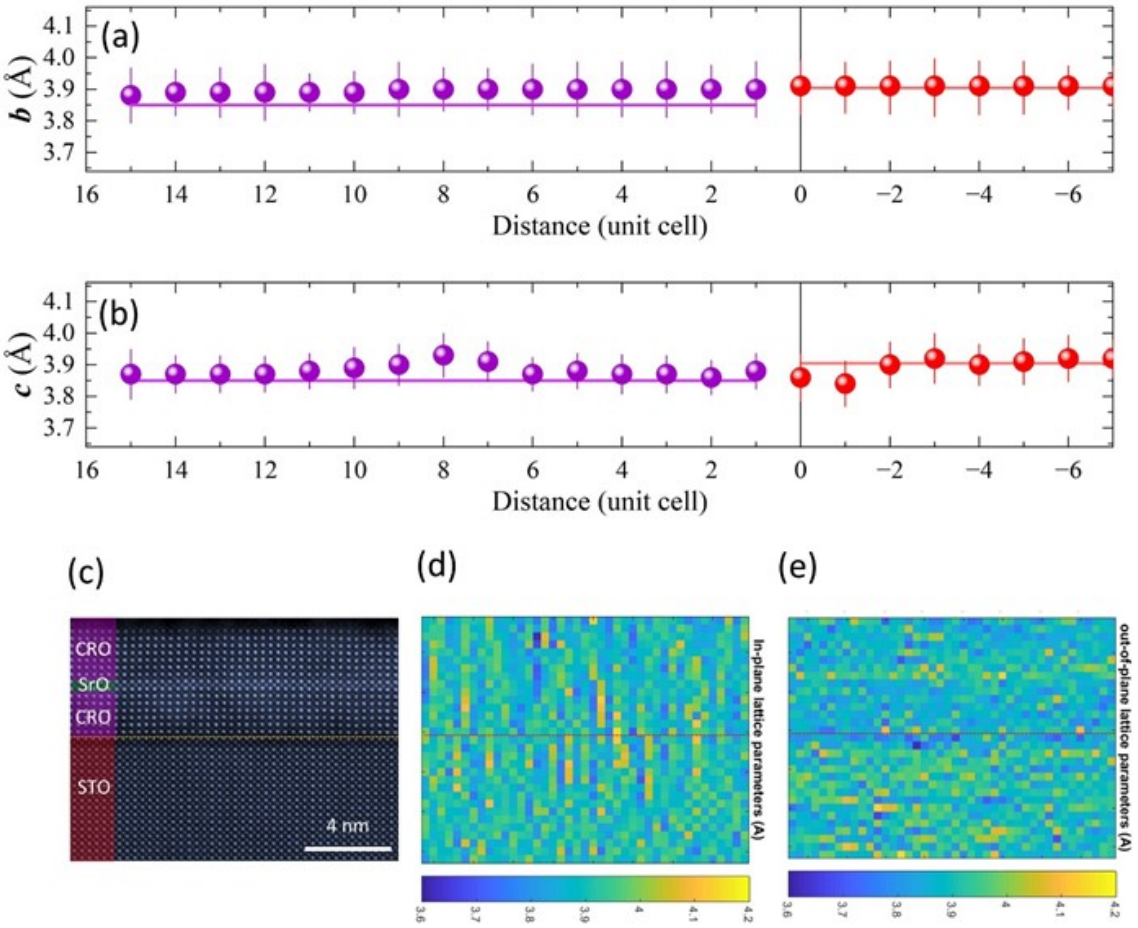

Figure 5.5. CRO^{7}-SrO-CRO^{7} heterostructure: (a) In-plane, and (b) out-of-plane lattice parameters plotted as a function of distance from the film-substrate interface. The error bar shows the standard deviations of the averaged measurements along the *b*-axis. The pseudocubic lattice parameters of bulk STO (3.905 Å) and CRO (3.85 Å) are indicated by a red and purple solid line, respectively. (c) Atomic-scale structure of the δ-doped CRO^{7}-SrO-CRO^{8} heterostructure by STEM, and corresponding (d) in-plane, and (e) out-of-plane lattice spacing mapping. The yellow dashed line in panel (c) represents the film-substrate interface.

5.2.3 Octahedra Rotational Domains

In most perovskites (ABO_3), the A and B cations radii mismatch often leads to a strain buildup along A-O and B-O bonds, though the strain is accommodated via BO_6 octahedral rotations. These rotations are often explained by Glazer notation ($a^x b^x c^x$) [3,110,111], which describes rotations of the octahedra about three orthogonal pseudo-cubic crystallographic axes: $[100]_{pc}$, $[010]_{pc}$, and $[001]_{pc}$. The relative BO_6 rotational magnitude about an axis is represented by letters *a*, *b*, and *c*. The superscript *x* refers to whether adjacent octahedral around one given

axis can rotate in-phase (+), out-of-phase (–), or no rotation (0). In Glazer notation, the orthorhombic CRO and SRO exhibit $a^+b^-b^-$ [*Pbnm* (No. 62)] [5] patterns as shown in Figure 5.6. This implies that octahedral rotations are in-phase around $[100]_{pc} \parallel [001]_O$, and out-of-phase about the $[010]_{pc} \parallel [1\text{-}10]_O$ and $[001]_{pc} \parallel [110]_O$.

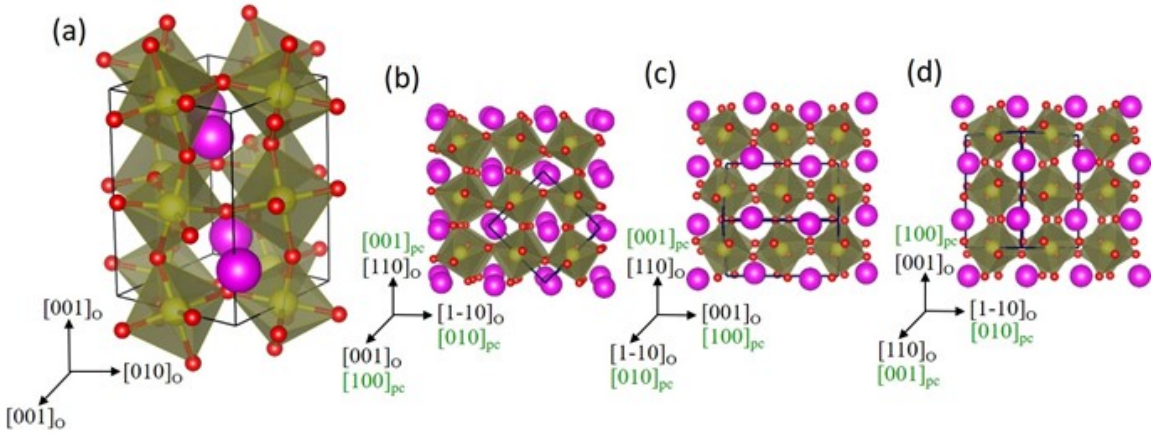

Figure 5.6. (a) Orthorhombic bulk structure CRO. (c)-(d) Schematics of $a^+b^-c^-$ rotational pattern. The octahedral rotations are (b) in-phase around $[001]_O$ ($[100]_{pc}$), (c) out-of-phase about $[1\text{-}10]_O$ ($[010]_{pc}$), and (d) $[110]_O$ ($[001]_{pc}$). Here, the subscripts desiginate Orthorhombic (O) and pseudo-cubic (pc) unit cells.

The orthorhombic (CRO) unit-cell oriented on the cubic STO (001) grows in the $[110]_O$ direction as shown in Figure 5.7(a). Therefore, either in-phase $[001]_O$ or out-of-phase $[1\text{-}10]_O$ rotation axis can align along the [100] direction of STO, generating two different structural domains with a 90° rotation (referred as A and B, see Figure 5.7]. [112,113] Viewing along the [100] direction of STO substrate, we can acquire projected structures of the film in $[001]_O$ direction from domain A and $[1\text{-}10]_O$ direction from domain B simultaneously. In domain A type structure, the in-phase rotation (+) pseudo-cubic $[100]_{pc}$ axis is aligned with the $[100]_S$ [see Figure 5.7(a-b)], thus following substrate-film orientation relation holds: CRO $[001]_O$ ($[100]_{pc}$) $\parallel$ $[100]_S$; CRO $[1\text{-}10]_O$ ($[010]_{pc}$)$\parallel$ $[010]_S$; CRO $[110]_O$ ($[001]_{pc}$) $\parallel$ $[001]_S$. In domain B, the CRO $[010]_{pc}$ out-of-phase rotation axis is parallel with $[100]_S$ [see Figure 5.7(e-f)], and orientation follows: CRO $[1\text{-}10]_O$ ($[010]_{pc}$)$\parallel$ $[100]_S$; CRO $[001]_O$ ($[100]_{pc}$) $\parallel$ $[010]_S$; CRO $[110]_O$ ($[001]_{pc}$) $\parallel$

$[001]_S$. The structure in domains A and B are equal, but with 90° rotation.

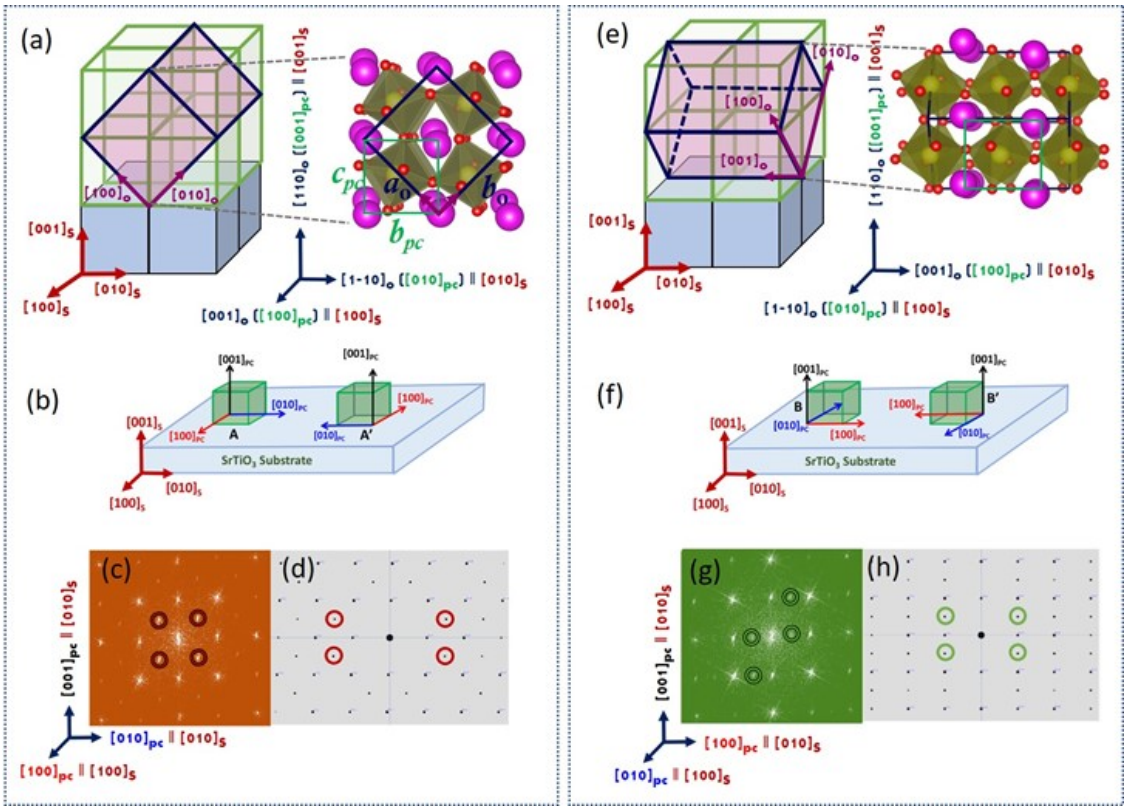

Figure 5.7. (a) Schematic illustration of CRO film with $[110]_O$ growth on a cubic $SrTiO_3$ substrate with CRO $[001]_O$ ($[100]_{pc}$) || $[100]_S$ (b) Representation of Domain A, whereas the in-phase rotation (+) film pseudocubic $[100]_{pc}$ axis (marked red) aligns with $[100]_S$. (c) Fast Fourier Transform (FFT) and (d) simulated electron diffraction patterns along in-phase rotation axis: $[100]_{pc}$ || $[100]_S$. (e) Illustration of $CaRuO_3$ film on $SrTiO_3$ substrate with orientation: CRO $[1\text{-}10]_O$ ($[010]_{pc}$) || $[100]_S$. (f) Representation of domain B, whereas in-phase rotation (+) pseudocubic $[100]_{pc}$ axis is parallel with $[010]_S$. (g) FFT and (h) simulated diffraction patterns with electron the beam perpendicular to the in-phase rotation axis, i.e. $[010]_{pc}$ || $[100]_S$.

Domain A and B structures are confirmed by the Fast Fourier Transform (FFT) results obtained from high-resolution STEM imaging. The FFT pattern shown in Figure 5.7(c) is consistent with the simulated diffraction pattern of Domain A as in Figure 5.7(d). This confirms the presence of domain A type unit-cell symmetry, where CRO $[100]_{pc}$ in-phase rotation axis is parallel with $[100]_S$ as observed for $SrRuO_3$ counterpart [112,114]. The consistency of the fractional spots (marked in green) in Figure 5.7(g-h) confirms domain B structural variant. Viewing along the $[001]_S$ direction, we can acquire CRO film octahedral structural information

in $[100]_{pc}$ direction from domain A and $[010]_{pc}$ direction from domain B simultaneously, as shown in Figure 5.7.

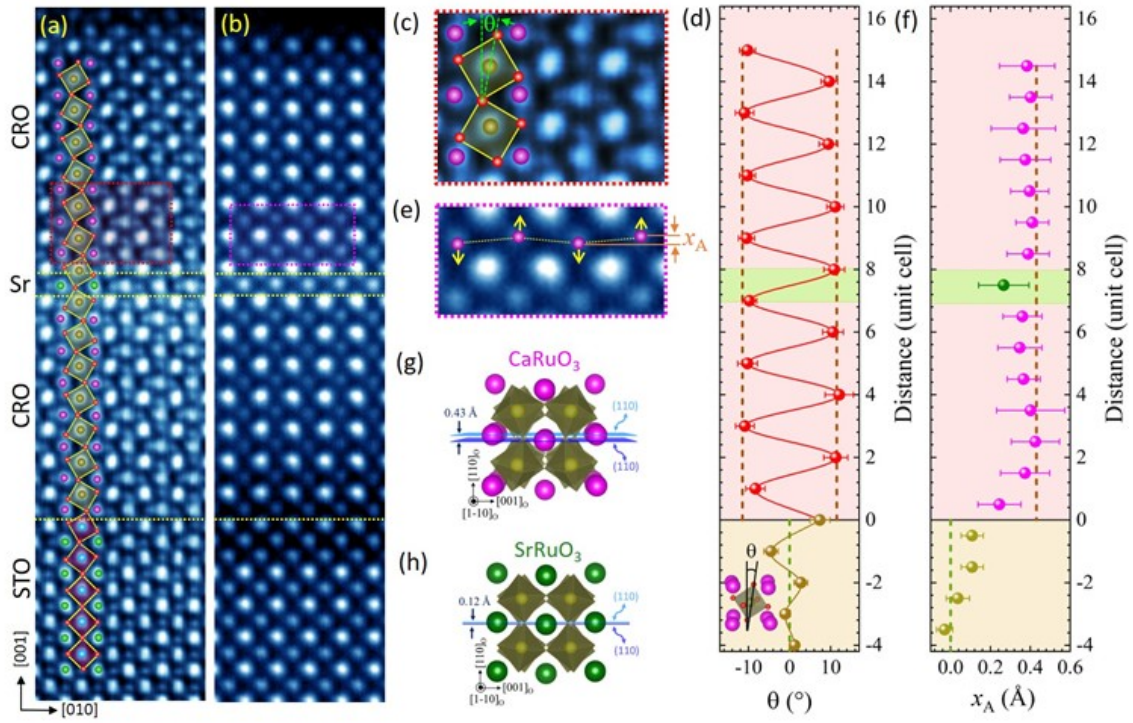

Figure 5.8. Atomically resolved structure of CRO[7]-SrO-CRO[8] heterostructure: (a) intensity-inversed ABF and (b) HAADF images representing domain A and B, respectively. (c) Zoom-in image of the area marked in (a) superimposed by projected octahedra and tilt angle (θ), and (d) θ as a function of distance from the film-substrate interface. (e) Zoom-in image of the area marked in (b) superimposed by the corresponding A-site cation displacement (x_A), and (f) x_A versus atomic distance. The arrows in (e) mark the A-site displacement direction thus forming an up-down buckling pattern in AO plane. The dashed lines in (d) and (f) represent the value of θ and x_A of bulk CRO (brown) and STO (green), respectively. Schematic of the bulk crystal structure of (g) CRO and (h) SRO showing A-site displacement projected along $[1\text{-}10]_O$ direction. The top (110) plane (light blue) passes through the center of the left and right Ca (Sr) atom, and the dark blue (110) plane bisects the center of the middle Ca (Sr)-atom, whereas the projected A-site displacement corresponds to the distance between the two parallel planes.

The high-resolution STEM imaging permits us to reveal the structural distortions as illustrated in Figure 5.8. The structure of domain A and B is identical, but when viewing simultaneously along the $[001]_S$ direction the RuO_6 tilt can be observed in domain A because the in-phase (+) octahedral rotation axis is parallel to [100]-STO [see Figure 5.7(a), Figure 5.8(a), and Figure 5.8(c)]. On the other hand, for domain B, the electron beam incident along the out-of-

phase (-) octahedral rotation axis, and hence the octahedra rotation/tilt could not be resolved in the ABF image because of oxygen overlapping [see Figure 5.7(e) and Figure 5.8(b)]. However, the A-site cation displacements due to orthorhombic distortion can be measured [109,115], showing a zigzag pattern [see Figure 5.8(b), and Figure 5.8(e)].

The projected octahedral tilt [θ as denoted in Figure 5.8(c) and Figure 5.8(d)] extracted from the ABF images of domain A [Figure 5.8(a) and Figure 5.8(c)] shows that except at the 1st unit-cell near film-substrate interface (~ 8.4°), the RuO_6 tilt angle in the CRO film is constant (~ 11°), a nearly identical behavior as that of CRO bulk (~ 11.5°). Hence, the octahedral mismatch is adjusted close to the film-substrate interface, where TiO_6 interfacial layers in the STO side undergo distortion to accommodate the octahedral mismatch of RuO_6-TiO_6. We note that the 15-u.c. undoped CRO film also has θ ~ 11° [see Figure 5.9(a), Figure 5.9(c), and Figure 5.9(f)]. Therefore, the octahedral network structure is not altered by the SrO-interlayer insertion. Instead, due to a corner-connectivity constraint, the octahedral geometry is conserved throughout the entire δ-doped heterostructure, i.e., the structure preserves bulk-CRO orthorhombic symmetry.

The A-site cation displacements (x_A), a signature of orthorhombicity [109,115], were determined quantitatively for individual layers with the domain B imaging [Figure 5.8**(b)** and Figure 5.8**(e)**]. It is seen that the δ-doped heterostructure [see Figure 5.8**(f)**] shows an averaged Ca-site x_A ~ 0.38 ± 0.07 Å, which matches that of a pristine CRO film [~ 0.38 ± 0.07 Å, see Figure 5.9(b), Figure 5.9(e), and Figure 5.9(g)] while slightly smaller than CRO bulk [~ 0.43 Å, see Figure 5.8(g)]. On the other hand, the x_A at nested SrO is reduced to 0.26 ± 0.10 Å [see Figure 5.8(f)], but it is significantly larger than that in bulk $SrRuO_3$ [~ 0.12 Å, see Figure 5.8(h)]. These observations suggest a small local structural modification is present in the SrO layer, which is induced by ionic (Ca/Sr) mismatch as governed by the Goldschmidt tolerance factor. [29,102]

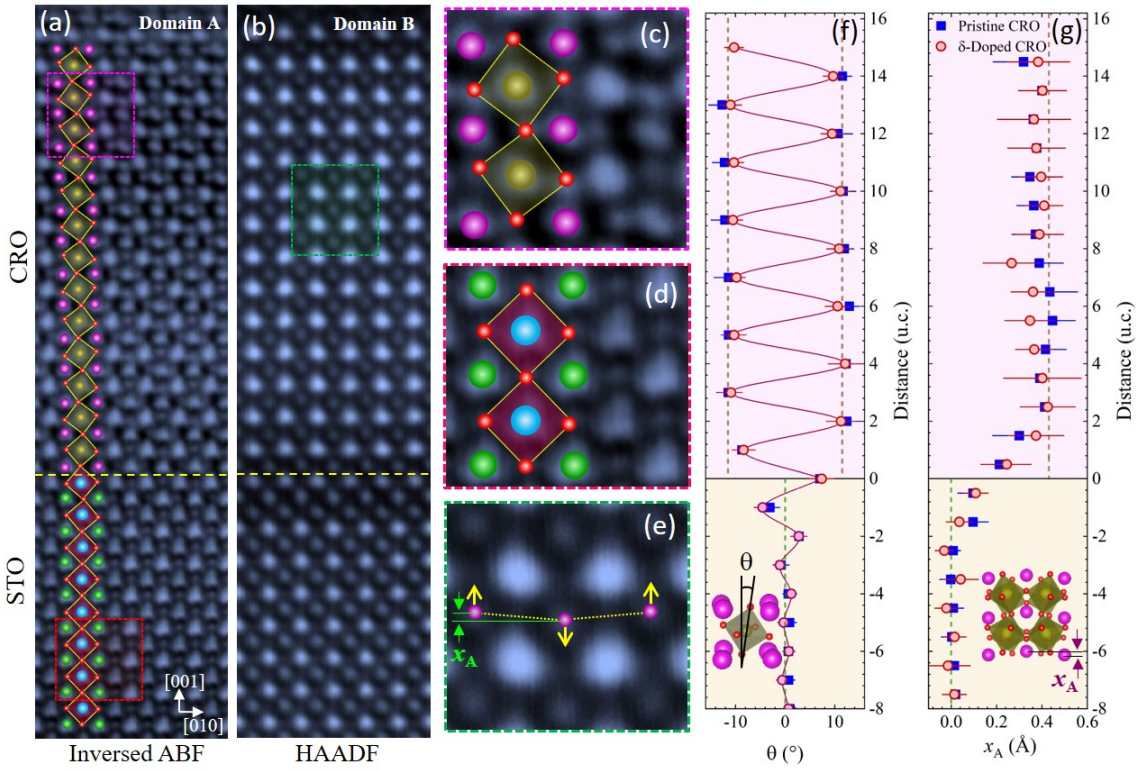

Figure 5.9. Undoped CRO 15 u.c. (CRO[15]) film STEM images: (a) intensity-inversed ABF, and (b) HAADF images. (c-d) Zoomed in portion of regions marked in panel (a) superimposed with projected octahedra shape. (e) Zoom-in image of the area marked in (b) overlaid by the corresponding A-site cation displacement (x_A), whereas the arrows in (e) mark the A-site displacement direction thus forming an up-down buckling pattern in AO plane. (f-g) Projected octahedral tilt angle (q) (f), and A-site cation displacement (x_A) (g) as a function of distance from interface of pristine CRO[15] and δ-doped CRO [CRO[7]-SrO-CRO[8]]. The dashed lines in (f) and (g) represent the projected tilt angle, and A-site cation displacements of bulk CRO (brown) and STO (green), respectively.

5.2.4 Electrical Properties of Pristine and δ-doped CRO Films

To understand the δ-doping effect on the electronic properties of CRO films, we have systematically measured the transport behavior of the CRO films with and without SrO insertion. The electron transport measurements were performed in a four-probe configuration on Quantum Design Physical Property measurement system (PPMS) in the temperature range of 300-5 K.

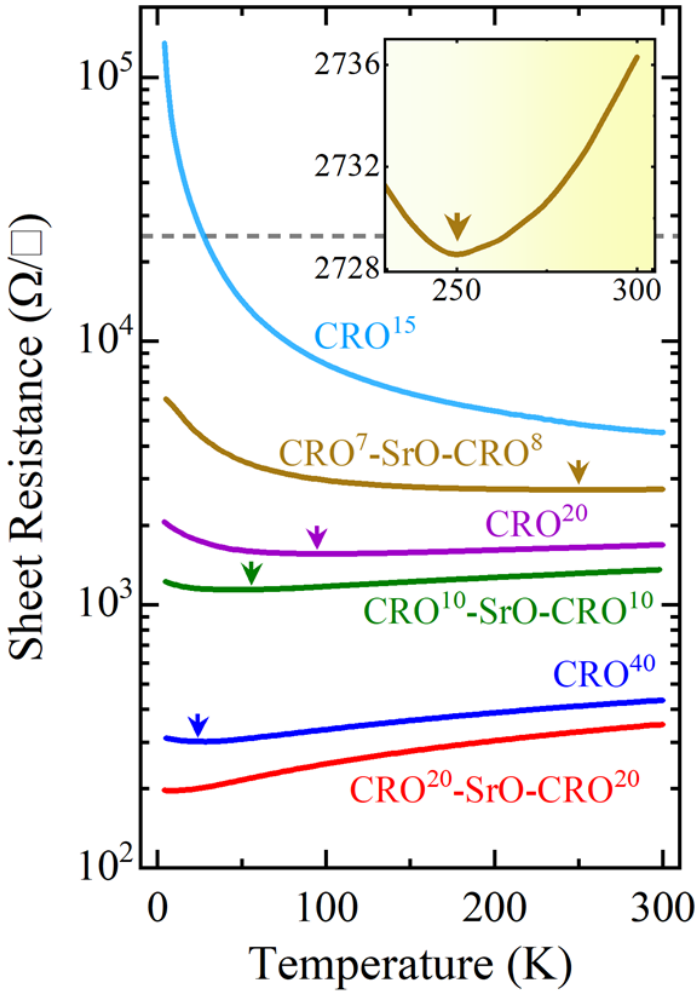

Figure 5.10. Pristine and δ-doped CRO; (a) temperature-dependent sheet resistance. In panel (a) the dashed grey-line marks the Mott-Ioffe-Regel limit representing quantum of resistance (25 kΩ), while the arrows indicate the characteristic temperature below which a resistivity upturn occurs. The inset of (a) shows the temperature-dependent sheet resistance of CRO^{7}-SrO-CRO^{8}, highlighting the resistivity upturn.

Figure 5.10 shows the temperature evolution of the sheet resistance of pristine and δ-doped CRO films of different thicknesses. As shown in Figure 5.10, the thicker pristine CRO^{40} film exhibits bulk-like metallic transport ($d\rho/dT > 0$) down to ~21 K, followed by a small resistivity upturn, characterized by weak localization. The 40 u.c. CRO film shows metallicity with a low temperature resistivity minimum. The resistivity upturn could arise from phenomenon of weak localization (as describe latter) [54,63,116–118].

Nevertheless, the intermediate-thickness: CRO^{20} film features a metallic behavior at high

temperatures, but exhibits a resistivity upturn below ~95 K [see Figure 5.10]. Such a robust resistivity upturn at low temperatures is frequently observed in many metallic oxide films [54,63,116,117], especially close to the verge of a metal-insulator transition. Finally, the 15 u.c. (CRO^{15}) film is identified to be fully insulating ($d\rho/dT < 0$ at all temperatures). In contrast to insulating CRO^{15}, the δ-doped film i.e., CRO^{7}-SrO-CRO^{8} displays improved conductivity holding a room temperature metallicity, though a strong upturn appears below ~ 250 K as shown in the inset of Figure 5.10. Likewise, the δ-doping consistently lowers the resistivity and resistivity upturn temperatures, as seen in CRO^{10}-SrO-CRO^{10} and CRO^{20}-SrO-CRO^{20} as displayed in Figure 5.10.

5.2.5 Metal-Insulator Transition

Now, we want to describe the low-temperature resistivity upturn observed in 40 u.c. CRO film. The resistivity upturn could arise from phenomenon such as weak localization (WL), or electron-electron interactions (EEI).

In disordered systems, weak-localization is caused by the quantum-interference of conducting electrons on systems defects leads to enhanced backscattering of the conducting electrons, and producing a resistivity upturn. Therefore, WL in 2D system outcomes in a quantum correction to conductivity, which possesses characteristic logarithmic: ln (T) dependence [85]. The effect of weak localization is an outcome of electron interference with itself, however, the wavefunctions of different electrons can also interfere.

The effect of weak localization is an outcome of electron interference with itself, however, the wavefunctions of different electrons can also interfere. Consequently, in disordered systems, increased carrier scattering diminishes the effective electron screening, thereby leading to EEI enhancement and a broad opening of the Coulombic gap possessing a zero density of states [119,120]. We refer to it as quantum mechanical EEI correction to conductivity, whereas

in 2D systems, the conductivity scales with temperature logarithm [85]. Figure 5.11 shows that the low-temperature resistivity upturn of CRO[40] indeed scales well with ln T, supporting that the resistivity upturn in CRO[40] is caused by weak localization.

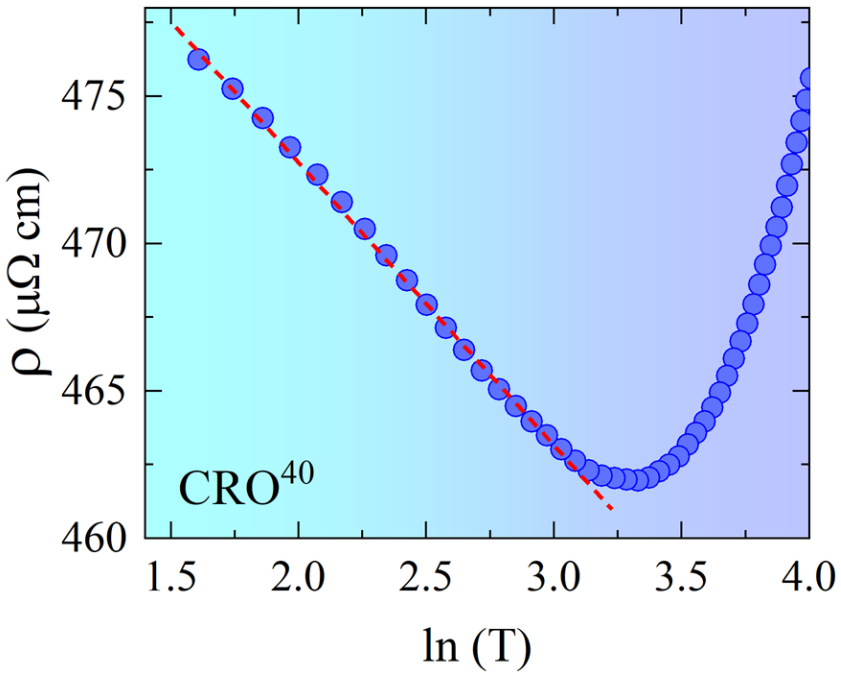

Figure 5.11. CRO 40 u.c. resistivity versus logarithm of temperature. The red solid line is linear fit.

To detect the temperature exponent for transport of CRO[15], we considered four conduction models. In the Anderson-type insulating state, the electron hopping to the nearest neighbor sites is restricted, since electronic thermal energy is smaller as compared to the energy difference between adjacent localized states, which means that electrons cannot overcome the energy barrier caused by disorder, and thus hopping to the far localized site is not probable. Though, to hop, the electrons have to locate a site, where the difference of energies between the two localized sites is small, which leads to variable range hopping (VRH) conduction. Mott categorized this phenomenon with resistivity scaling as: $\rho\,(T) = \rho_0 \exp\left[\left(\frac{T_M}{T}\right)^{\frac{1}{d+1}}\right]$. Here, d is system dimensionality: d = 1, 2, 3, and $T_M = \frac{\beta_M}{N(E_F)\xi^d k_B}$ is Mott characteristic temperature (β_M, ξ

and $N(E_F)$ is constant, localization length, and Fermi-level density of states, respectively [81,82].

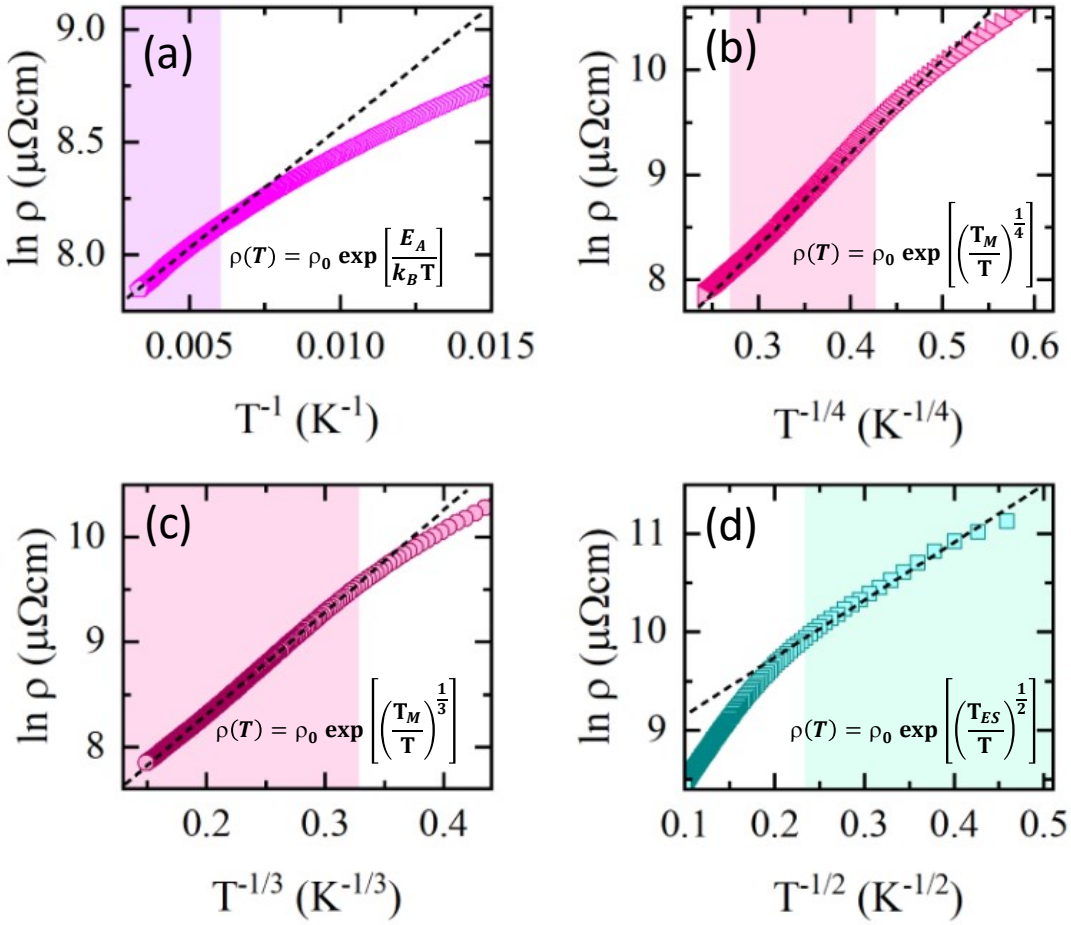

Figure 5.12. CRO 15 u.c. logarithmic resistivity versus (a) T^{-1} (thermal activation model), (c) $T^{-1/4}$ (3D-Mott VRH), (c) $T^{-1/3}$ (2D-Mott VRH), and (a) $T^{-1/2}$ (Efros VRH). The dashed line is the linear fit.

In Mott-type VRH, the Coulomb interaction between hopping sites is ignored, thus the density of states near Fermi level is considered as a constant. However, in Efros and Shklovskii variable range hopping (ES-VRH), where Coulombic interactions are taken into consideration, the *e-e* interactions lead to a Coulomb gap at low temperatures. In this case, the resistivity in all dimensions scales as: $\rho\,(T) = \rho_0 \exp\left[\left(\frac{T_{ES}}{T}\right)^{\frac{1}{2}}\right]$, here; $T_{ES} = \beta_{ES}\, e^2/\varepsilon\, k_B\, \xi$ is a Efros characteristic temperature with β_{ES}= 2.8, ξ is localization length, *e* elementary charge, and ε

dielectric constant [81,82,119].

The thermal activation: $\rho\ (T) = \rho_0\ e^{E_A/k_BT}$, where ρ_0 is the resistivity coefficient, and E_A is the activation energy. The Efros VRH $\rho\ (T) = \rho_0\ e^{(T_{ES}/T)^{1/2}}$, where T_{ES} is Efros temperature. The 2D-Mott VRH $\rho\ (T) = \rho_0\ e^{(T_M/T)^{1/3}}$, and 3D-Mott VRH $\rho\ (T) = \rho_0\ e^{(T_M/T)^{1/4}}$, where T_M is Mott temperature [see Figure 5.12]. In the high temperature range, thermal activation and 3D Mott-VRH could not produce a decent linear curve of logarithmic resistivity versus T^{-1} and $T^{-1/4}$, respectively [see Figure 5.12(c-b)]. Specifically, the CRO^{15} transport follows a Mott-type VRH [$\ln(\rho) \propto T^{-1/3}$] above ~25 K [Figure 5.12(c)], indicating that the transport is governed by disorder-driven Anderson localization [81,82,121,122]. At low temperatures, a crossover to Efros-type VRH [$\ln(\rho) \propto T^{-1/2}$] is observed [see Figure 5.12(d)], likely suggesting the significance of *e-e* interactions in the strong localization regime [120,123–125].

5.2.6 Magneto-transport

The δ-doping of CRO films not only triggers the enhancement of conductivity but also induces a pronounced ferromagnetic order revealed by magnetoresistance (MR) shown in Figure 5.13. The MR in pristine CRO^{40} and CRO^{20} is very small, as expected in paramagnetic metallic systems as in Figure 5.13(a). However, the MR effect is monotonically enhanced with reducing film thickness to CRO^{15}, encompassing a small but noticeable MR hysteresis, suggesting a weak and possibly short-range FM fluctuation phase. Meanwhile, the low-field MR in CRO^{15} is positive [see blue arrows in Figure 5.13(a)] and becomes negative at higher fields. The positive MR is a sign of electron-electron correlations (EECs) that are stronger at low temperatures [85,126,127], consistent with the presence of Efros-type VRH $\rho(T)$ behavior.

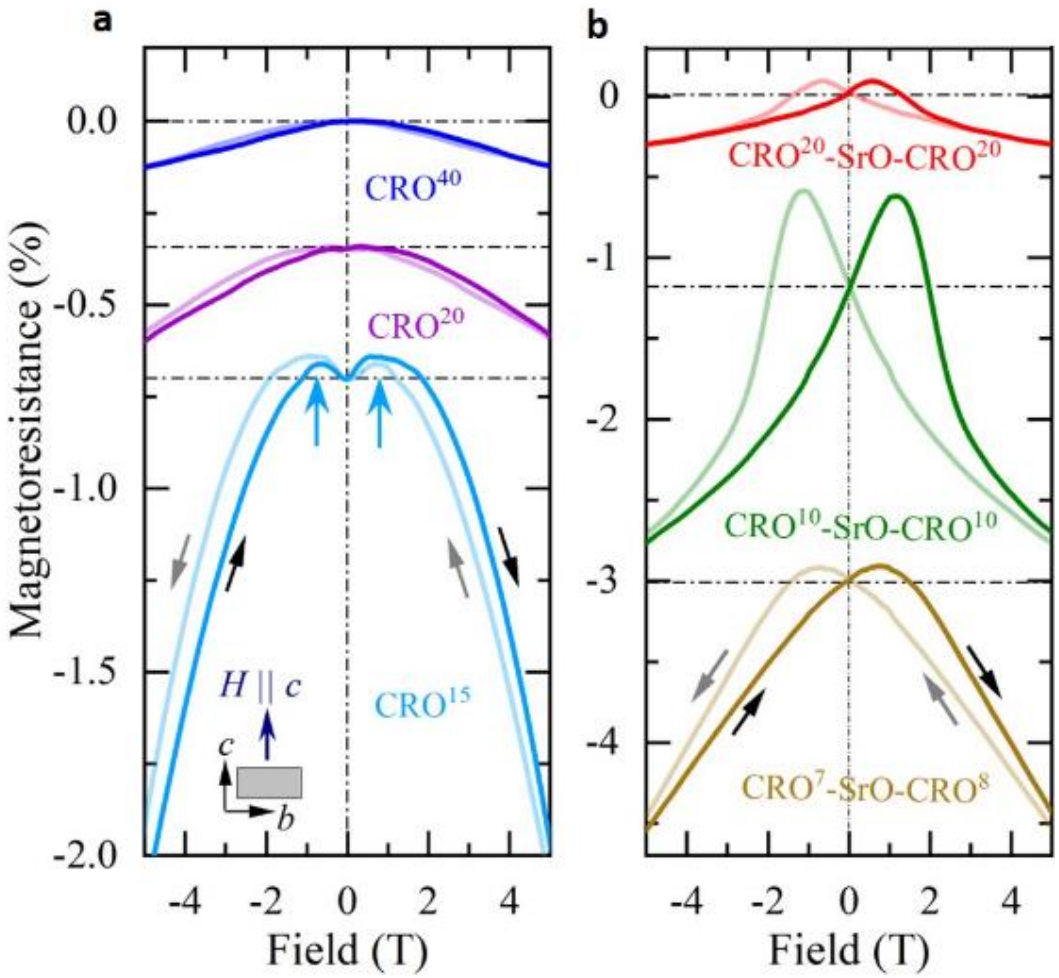

Figure 5.13. Magnetoresistance (MR) of (a) pristine and (b) δ-doped CRO at T = 5 K with the magnetic field applied along the film normal. The MR curves in (d)-(e) are offset to prevent overlapping.

In contrast, the δ-doping in CRO^{15} (i.e., CRO^{7}-SrO-CRO^{8}) leads to a clear butterfly-like MR [see Figure 5.13(b), characteristic of FM order. It is noteworthy that the emergence of an FM state concurs with the extinction of positive MR observed in pristine CRO^{15}. This feature likely supports the conjecture that the presence of FM ordering involves modification of EECs [108,128]. Such a distinctive hysteretic MR is also detected in both CRO^{10}-SrO-CRO^{10} and CRO^{20}-SrO-CRO^{20} [see Figure 5.13(b)], corroborating the appearance of FM ordering. [74,90,91,93,129,130] However, different from the pristine CRO films, the δ-doped films have a non-monotonic variation of MR effects with strongest one in CRO^{10}-SrO-CRO^{10}.

5.2.7 Magnetic Force Microscopy

To further reveal the unusual magnetic behavior in the δ-doped films, we performed cryogenic magnetic force microscopy (MFM) studies. The MFM experiments were carried out in a homemade cryogenic magnetic force microscope using commercial piezoresistive cantilevers (spring constant ≈ 3 N/m, resonant frequency ≈ 42 kHz). The MFM images of the CRO^{10}-SrO-CRO^{10} in different magnetic fields at 5.5 K are shown in Figure 5.14(a-h).

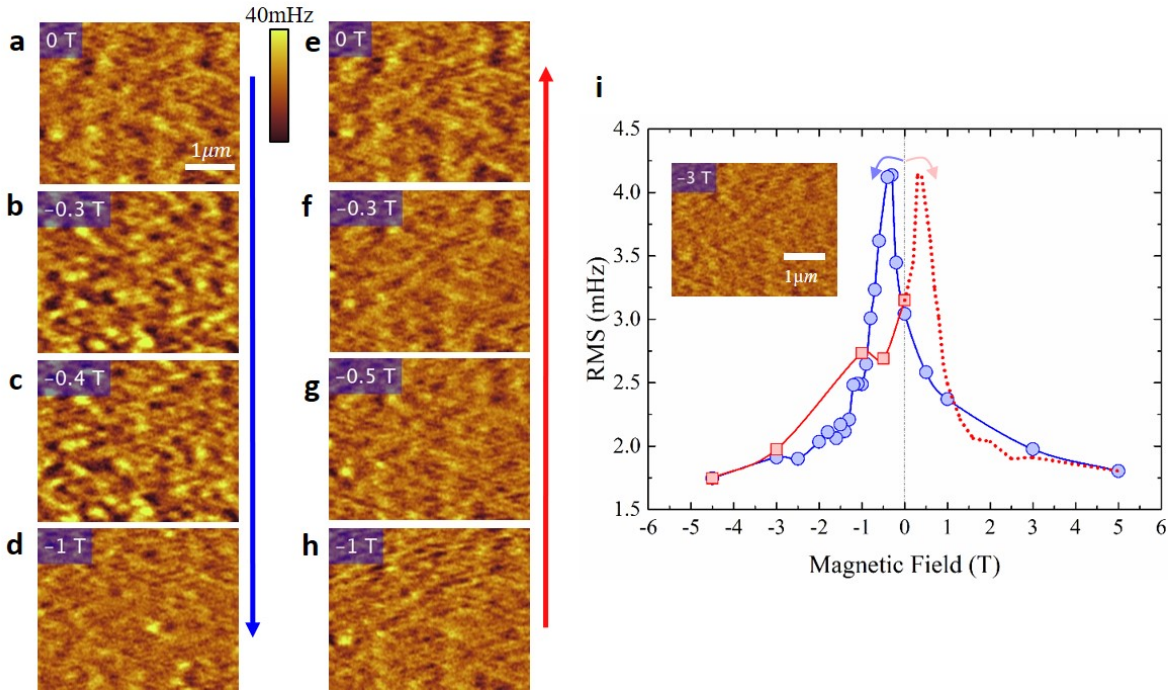

Figure 5.14. MFM images of the δ-doped CRO^{10}-SrO-CRO^{10} heterostructure taken in the increasing (a-d) and decreasing field (e-h) process (indicated by arrows). (i) Field-dependent RMS data representing the domain contrast. The inset in (i) is the MFM image of the same area measured at -3 T displaying a typical saturated state.

There is weak bubble-like magnetic contrast (bright-dark pattern) in the zero-field MFM image after the sample was saturated at a positive field (6 T), indicating magnetic inhomogeneity. The magnetic contrast is barely above the noise level of our MFM system. These features suggest that the FM order in the ground state is not fully long-range. With an increasing magnetic field, the dark-bright contrast increases strongly. More bubble-like magnetic contrast

emerges at -0.3 to 0.4 T [see Figure 5.14(b-c), indicating inhomogeneous switching of magnetic order. The field dependence of magnetic contrast as measured by the root-mean-square (RMS) value of the MFM images Figure 5.14(i) shows a sharp peak between 0 T and -1 T. While reaching its maximum value at around 0.3 T, the magnetic contrast is barely visible below -1 T, indicating that the sample is approaching saturation [see Figure 5.14(d). In accord with the above, the RMS value varies very little below -1 T. A typical MFM image of the sample at saturation is shown by the inset of Figure 5.14(i). In contrast to the negative ramping, relatively uniform magnetic contrast was observed between -6 T and 0 T after saturating the sample at -6 T as in Figure 5.14(h-e). Consistently, the RMS values of the MFM images do not vary much as shown in Figure 5.14(i), demonstrating the hysteretic behavior of the magnetic order. Overall, the evolution of the magnetic contrast and their hysteretic behavior provide supporting evidence of unusual ferromagnetism without fully long-range ordering in the sample.

5.2.8 Magnetization versus Temperature

The magnetization as a function of temperature M(T) of pristine and δ-dopped CRO films is shown in Figure 5.15(a). All pristine CRO films show a paramagnetic-like signal reminiscent of SrTiO3 substrate with no clear signs of ferromagnetic transition. Though, SrO δ-doping in the middle of CRO films induces a FM order as M(T) represents a paramagnetic to ferromagnetic transition. However, the M(T) curves in the δ-dopped CRO films has rather unusual T-dependence, showing non-typical long-range order M(T) line shape holding a very weak upturn between 35-60 K, though above, the magnitude of magnetization increases, but still relatively weak as compare to its sister counterpart SrRuO3 films.

Normally, a long-range ordered FM system above T_C obeys Curie-Weiss (CW) law; $\chi = \frac{C}{T-\theta_{cw}} = \frac{M}{H} \Rightarrow M^{-1} \propto (T- \theta_{cw})$, where C is the CW constant and θ_{cw} is the Weiss temperature, so that M^{-1} is linearly proportional to T above T_C. In our case here, a measurement of χ is not

feasible due to the extremely thin film limit, but the T-dependent inverse of magnetization [$M^{-1}(T)$] can shed light on the unusual CW behavior.

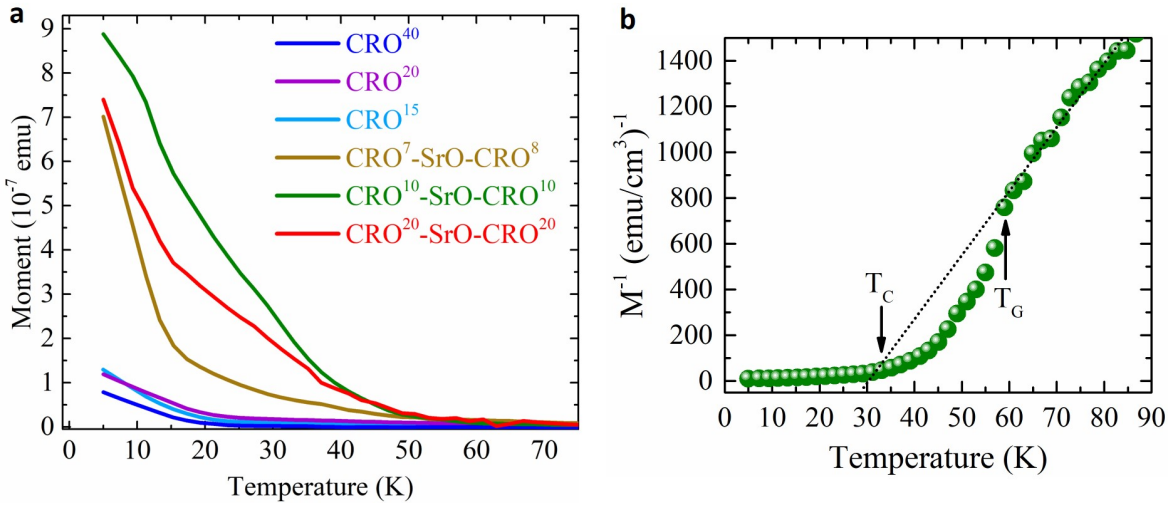

Figure 5.15. (a) Temperature-dependent magnetization of different thickness of undoped and δ-doped CRO films. (b) CRO^{10}-SrO-CRO^{10} magnetization (M) inverse as a function of temperature. The black dotted line indicates a guide for the linear fit.

As shown in Figure 5.15(b), the $M^{-1}(T)$ of CRO^{10}-SrO-CRO^{10} in the paramagnetic state exhibits fair linearity only above a characteristic temperature $T_G \sim 60$ K, but a sudden downturn occurs below T_G. Such a deviation from the CW law in the temperature range $T_C < T < T_G$ is reminiscent of a Griffiths-phase (GP) phenomenon. [29,131–134] GP is characterized by the coexistence of ferromagnetic entities within the globally paramagnetic phase, causing a non-analytical behavior in magnetic susceptibility with characteristic departure from Curie-Weiss behavior in the vicinity of T_C and T_G (T_G is referred to as Griffith's temperature). [29,131–134] Such GP signature has been reported in bulk Ca-doped $SrRuO_3$, where Ca substitution for Sr introduces ferromagnetic spin-spin coupling dilution through Ru-O-Ru bonds, and leads to T_C reduction [29].

5.2.9 Density Functional Theory Calculations

We have performed density functional theory (DFT) calculations on the heterostructure

shown schematically in Figure 5.16(a) to gain additional insights into the observed phenomena. Analyzing the structural changes due to the δ-doping, we find that the plane-projected octahedral tilt angle [see Figure 5.16(b)] remains essentially unchanged, whereas there is a dip in the A-site cation displacement x_A [see Figure 5.16(c)], consistent with the STEM data. Additionally, by looking at the RuO_2 interlayer spacing (Δ), a significant increase at the place of the δ-layer site occurs paralleling the dip in x_A [see Figure 5.16(d)]. Although not evident in the projected tilt angle (θ) measured by STEM, there is a large change in the 3D octahedral angle [Θ, see Figure 5.16(e)] at the δ-doping layer. Taken together, these results indicate that the insertion of the δ-doping layer causes a highly local modification of the atomic structure confined between the adjacent RuO_2 layers.

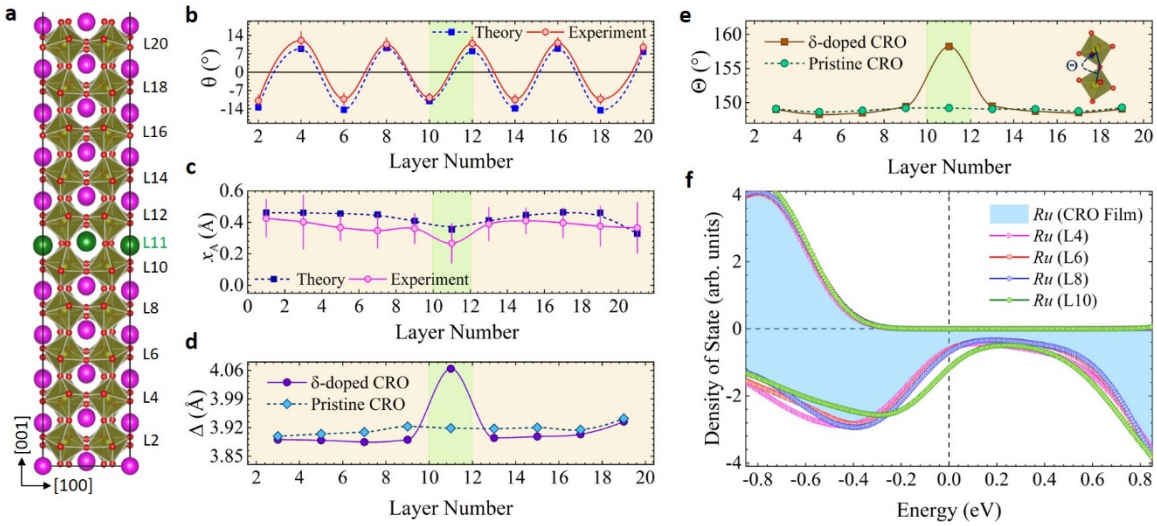

Figure 5.16. (a) Schematic representation of δ-doped heterostructures, where one of the Ca atomic (purple) layers is replaced by Sr atoms (green). (b) Theoretical and experimental projected octahedral tilt angle (θ), and (c) A-site cation displacement (x_A). (d) Calculated RuO_2 interlayer spacing (Δ), and (e) three-dimensional octahedron bond angle (Θ). (f) Layer-by-layer Ru-projected DOS of the heterostructure, with the selected layers labeled as in panel (a). Up-spins (majority) are represented as positive and down spins (minority) as negative.

Further, we show the calculated Ru-projected DOS for the pristine CRO thin-film in the layers adjacent to the CaO layer that gets replaced by SrO (blue-shaded region). It is clear that

the thin-film is semi-metallic [13,67]. We assume that such a thin film models CRO^{15}, which according to Figure 5.16(f), is on the verge of being ferromagnetic (the accuracy of our DFT+U calculations would not allow us to reliably predict at what thickness such a state would exist). In Figure 5.16(f)., we also show the Ru-projected DOS for the δ-doped film in several layers near the SrO plane. We note that the DOS in the immediately adjacent (green curves) differs from the others in that it signifies an enhancement of the DOS at the Fermi energy by approximately a factor of 2.

5.2.10 Discussions

If some form of disorder is present at increasing levels as the film thickness is reduced, the thinnest film may have sufficient disorder to induce Anderson localization in the small number of states at the Fermi energy E_F throughout the CRO film. Hence a MIT occurs at a critical thickness. If we then assume that the same level of disorder is present in a doped film as in an undoped film we reason as follows. In films of all thicknesses, a doped film has a larger DOS at E_F in the vicinity of the SrO layer than in the corresponding undoped film. Thus, in all doped films, only a fraction of the propagating states in the region of the SrO layer undergo localization, creating a "mobility edge", i.e., propagating states remain so, and the MIT is avoided. This effect enhances the conductivity of films above the critical thickness, as observed. For thin films below the critical thickness, the same effect induces metallic behavior in the region of the SrO layer, which is also in agreement with the experimental data since the data cannot tell if the film is conducting throughout or only in the region of the SRO layer. As for the Griffiths-phase-like ferromagnetism in doped CRO films, the above analysis also tells us that there may be sufficient density of propagating states at E_F in the SrO region to satisfy the Stoner criterion locally. We can then speculate that nonlocal exchange may trigger a domino effect, which generates patchy ferromagnetism throughout the CRO film. It is not currently practical to

perform DFT calculations in large heterostructures using hybrid functionals that include nonlocal exchange and check if the formation of FM patches in the CRO film lowers the total energy. The domino possibility remains to be tested.

5.3 Conclusion

In summary, we show that $CaRuO_3$, otherwise being metallic and at the verge of a magnetic critical point, retains its nonmagnetic nature but becomes insulating in thin film form under a critical thickness (15 u.c.). In contrast, d-doping a single layer of SrO into ultra-thin CRO films results in an emergent Griffiths phase to unusual ferromagnetism and a transition back to a metallic state while the entire heterostructures preserve the bulk-CRO orthorhombic lattice symmetry. Atomic-resolution imaging along with DFT calculations find that SrO-layer insertion causes only highly local structural and electronic changes. The calculated DOS at the Fermi energy shows a noticeable enhancement near the insertion layer, leading to the local satisfaction of the Stoner criterion, which in turn may induce patchy ferromagnetism in the entire film by nonlocal exchange interactions. The observations demonstrate the fragility of the emerging magnetic state in CRO, shedding light on the role of A-site cation in electronic and magnetic structure additional to lattice distortion in ruthenates. These findings provide an innovative pathway to understanding the correlated system's electronic and magnetic nature through heterostructure architecture.

Chapter 6. Strain Stabilized Ba Substitution Driven Cubic $SrRuO_3$

The ruthenates perovskite series ($ARuO_3$, A= Ca, Ba, or Sr) exhibits unique properties owing to a subtle interplay of crystal structure, and electronic spin degrees of freedom. Here, we demonstrate continuous tunning of crystal symmetry from orthorhombic to tetragonal to cubic-like phase (no octahedral rotations) in $SrRuO_3$ achieved via epitaxial-strain stabilized Ba substitution ($Sr_{1-x}Ba_xRuO_3$ with $0 \leq x \leq 0.7$). Remarkably, $Sr_{0.8}Ba_{0.2}RuO_3$ film without octahedral rotations ($a^0b^0c^0$), and flat Ru-O-Ru bond angle exhibits a nearly identical T_c ~145 K to that of orthorhombic $SrRuO_3$, and is accompanied by an enhanced perpendicular magnetic anisotropy. Though, increased Ba-substitution ($x \geq 0.5$) significantly condenses the ferromagnetism, suggesting that B-cation and oxygen atom bonding nature and bond length become more important than the octahedral bond angle. The results provide a confirmation that besides determining octahedral distortion, the A-site introduces certain entangled electro-magnetic effects that greatly affect the ruthenates magnetic order.

6.1 Introduction

Perovskite oxides (ABO_3) show a wide range of emergent functionalities originating from electro-magnetic interactions coupled to the octahedral units [8,49]. In the bulk perovskite oxide system, the oxygen octahedral environment is generally controlled via conventional chemical substitution or external stimuli such as hydrostatic pressure or temperature [102,135,136]. Besides, the lattice-mismatch epitaxial strained growth and artificial heterostructures [67,76,112,130,137–139] provide a possible engineering platform exploiting the structure-property relationship to stabilize perovskites oxides with multi-functional properties such as ferromagnetism in nonmagnetic materials [47,99], superconductivity [53], and ferroelectricity [50,140]. In particular, it has been shown that, by imposing an artificial heterostructures geometry, the magnetic anisotropy could be tuned due to the modified B-O-B

bond angle [6,7,141], highlighting the significance of the octahedral distortion controlling spins alignment and magnetization dynamics [6,7,141–145].

Perovskite ruthenates ($ARuO_3$) with substitution of A-site from Ca to Sr to Ba is an excellent candidate, where structural, and electron spin degrees of freedom are closely coupled [17,29,102,135]. The replacement of Sr^{2+} (1.44 Å) with Ca^{2+} (1.34 Å) ion preserves orthorhombic crystal symmetry, yet different sized ions (Ca^{2+} being smaller) substitution results in distinct Ru-O-Ru angles (CRO:148° and SRO:163°); leading to subtle modification in the Fermi-level density of states; a characteristic distinguishing ferromagnetic (FM) $SrRuO_3$ (SRO) from non-magnetic $CaRuO_3$ (CRO) [9,14,17,29,102,135]. In contrast, the larger A-site cation radii (Ba^{2+}: 1.61 Å) introduces a distinct effect of transitioning into a cubic-symmetry, yet ferromagnetism significantly reduces (T_c = 60 K), indicating that magnetism of ruthenates could not be simply explained by octahedra bond angle. Since the nominal electron counting is not changing, the octahedral angle, as well as A-O and Ru-O bonding nature appear to be controlling factor, but the dominant feature has still not been identified.

On other hand, it is difficult to synthesize the Ba-doped $SrRuO_3$ single crystals, whereas high pressures (18 GPa) are necessary to stabilize a perovskite structure, otherwise ambient conditions favor the formation of different polymorphs, making the stabilization of $Sr_{1-x}Ba_xRuO_3$ films rather difficult [29,135]. Yet, the challenge to engineer perovskite functionalities instigates finding innovative synthesis routes to manipulate the crystal structure. In this respect, the application of substrate-induced epitaxial strain delivers an auxiliary approach to high-pressure bulk synthesis and provides a viable epitaxial engineering platform to stabilize thin films with novel phases and multi-functionalities [53,146–150]. Thus, the epitaxial-strain provides the possibility to stabilize $Sr_{1-x}Ba_xRuO_3$ films, especially cubic-like perovskite ferromagnetic system stability would offer a possible platform to understand convoluted role of A-site cation in

determining the electro-magnetic structure of ruthenates.

In this study, we establish epitaxial stabilization of the $Sr_{1-x}Ba_xRuO_3$ thin films using strain engineering. Combining atomically resolved scanning transmission electron microscopy (STEM) imaging, electron energy-loss spectroscopy (EELS), and X-ray diffraction along with magneto-transport measurements, we reveal or show that in a series of $Sr_{1-x}Ba_xRuO_3$ thin films, depending upon the degree of strain-stabilized Ba-cation substitution, the crystal lattice could be continuously transmuted from bulk-like orthorhombic to cubic-like ($a^0b^0c^0$) phase enabled by change of RuO_6 distortions. Implanting Ba-cation, not only transforms the lattice symmetry but also triggers a modification in perpendicular magnetic anisotropy (PMA). The resultant cubic-like structure film is found to be ferromagnetic (T_c =145 K) with a strong PMA. However, increased Ba-implantation significantly reduces FM order, indicating that the A-site introduces certain intertwined effects that significantly impact the magnetic ordering of ruthenates.

6.2 Experimental Methods

Film Target Preparation. In this study, we systematically study the thin films of $Sr_{1-x}Ba_xRuO_3$ (x = 0, 0.08, 0.2, 0.5, 0.7). The desired series of $Sr_{1-x}Ba_xRuO_3$ thin film targets were synthesized by conventional solid-state reaction. The starting material of $SrCO_3$, $BaCO_3$, and RuO_2 in stoichiometric ratios was first mixed thoroughly and then heated at 1200° C in the air for 48 h. Regrinding and sintering at 1200 ° C were performed to increase the chemical homogeneity. The resultant powders were regrounded and pressed into pellets of 1'' under a pressure of 1000 psi. The pellets were then sintered at 1100° C for 48 h in an oxygen atmosphere. To increase the chemical homogeneity and target density, another sintering at 1100° C for 48 h in an oxygen atmosphere was performed.

Film Growth. The thin films of $Sr_{1-x}Ba_xRuO_3$ were grown by pulsed laser deposition (PLD) at 700° C with an oxygen pressure of 100 mTorr on TiO_2 terminated $SrTiO_3$ (001)

substrates. A KrF excimer laser (λ = 248 nm) with a 10 Hz repetition rate, and with an energy of 300 mJ was focused on $Sr_{1-x}Ba_xRuO_3$ targets. After film deposition, films were cooled down at ~10°/min to room temperature in an oxygen atmosphere of 100 mTorr. To monitor the film growth and thickness, the in-situ reflective high energy electron diffraction (RHEED) was employed. The film thickness was kept at ~ 40-unit cells (u.c.).

Scanning Transmission electron microscopy (STEM) and Electron energy loss spectroscopy (EELS). STEM and EELS experiments were performed on a 200 kV JEOL ARM electron microscope at Brookhaven National Library equipped with double aberration correctors, a dual energy-loss spectrometer, and a cold field-emission source. TEM samples were prepared using a focused ion beam with Ga^+ ions followed by Ar^+ ions milling to a thickness of ~30 nm. The atomic-resolution STEM images were collected with a 21 mrad convergent angle (30 μm condenser aperture) and a collection angle of 67 – 275 mrad for high-angle annular dark-field (HAADF) and 11 – 23 mrad for annular bright-field (ABF) imaging. The atomic positions were obtained using two-dimensional Gaussian fitting following the maximum intensity. The microscope conditions were optimized for EELS acquisition with a probe size of 0.8 Å, a convergence semi-angle of 20 mrad, and a collection semi-angle of 88 mrad. Dual EELS mode was used to collect low-loss and core-loss spectra simultaneously for energy drift calibration in the collecting process. EELS mapping was obtained across the whole film with a step size of 0.2 Å and a dwell time of 0.05 s/pixel. EELS background was subtracted using a power-law function, and multiple scattering was removed by a Fourier deconvolution method.

X-ray Diffraction. PanAlytical X'Pert thin-film diffractometer with Cu Kα−1 radiation with a single-crystal monochromator was employed to map out the X-ray coupled scan, omega scan, and reciprocal space mapping. The half-order integer spot measurements were carried out on a lab-based Malvern Panalytical X'Pert four-circle diffractometer with a collection time of

100-250 sec/point.

Electron and Magneto-transport. The magnetization was studied by using a Quantum Design Superconducting Quantum Interference Device, a reciprocating sample option. The electron transport measurements were performed in a four-probe configuration on a Quantum Design Physical Property measurement system in the temperature range 5-300 K. For the magnetoresistance (MR), the external magnetic field was applied along the film normal.

6.3 Results and Discussions

6.3.1 Crystal Structure

The crystal structure of films was analyzed using X-ray diffraction. Figure 6.1(a-b) shows the X-ray diffraction (θ-2θ) coupled scan around $SrTiO_3$ $(002)_{pc}$ Bragg's reflection for the series of $Sr_{1-x}Ba_xRuO_3$ thin films. In Figure 6.1(a-b), we can observe substrate and film peaks in conjunction with Laue interference fringes, confirming epitaxial stability and good crystallinity of thin films.

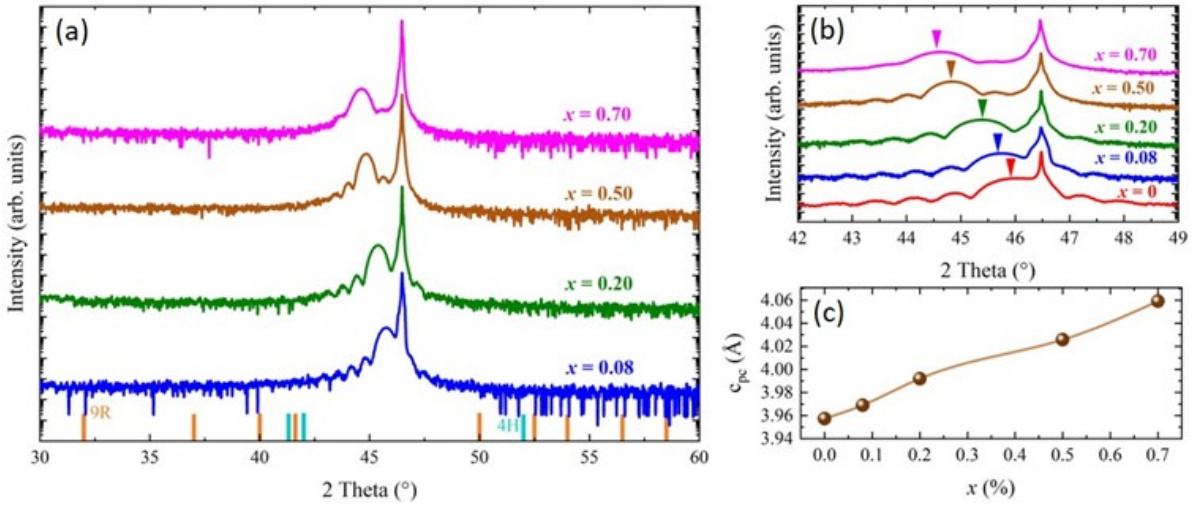

Figure 6.1. $Sr_{1-x}Ba_xRuO_3$ ($0 \leq x \leq 0.7$) thin films; (a) Long-range coupled (θ-2θ) X-ray scan, and (b) θ-2θ scan around (002) reflection spot. (c) out-of-plane pseudocubic (c_{pc}) lattice constant as function of Ba-doping concentration (x).

We note that the $Sr_{1-x}Ba_xRuO_3$ series of the bulk family could only be synthesized at high pressures, otherwise ambient conditions favor the development of different polymorphs [29,135].

The long-range couple scan displayed in Figure 6.1(a), establishes that we have succeeded in stabilizing a perovskite-type structure since the diffraction peaks are associated with polymorphs phases (nine-layered rhombohedral, four or six-layered hexagonal) are not observed [151]. The results demonstrate the effectiveness of epitaxial stabilization and the high crystalline quality of our thin films.

The lattice constant analysis shows that the out-of-plane lattice parameter could be systematically modified via Ba placement in presence of epitaxial strain [see Figure 6.1(c)]. For pristine $SrRuO_3$ film, we noted an out-of-plane lattice (OP) parameter of c_{pc}= 3.957 Å, whereas elongation in OP is caused by compressive strain (bulk $c_{pc,\ STO}$ = 3.905 Å < $c_{pc,\ SRO}$ =3.925 Å). On other hand, systematic Ba-substitution into the SRO lattice results in $(002)_{pc}$ peak shift to lower 2θ-angles [see Figure 6.1(a-b)]. The shifting of the peak suggests out-of-plane lattice parameter is expanded, whereas the OP parameter as a function of doping concentration (x) is shown in Figure 6.1(c). Such OP lattice enlargement with varying degrees of Ba cation substitution advocates a structural transition (more discussion later).

To further understand the crystal structure of $Sr_{1-x}Ba_xRuO_3$ thin films, we performed reciprocal space mappings (RSM) around (103) STO Bragg reflections. The RSM of $SrRuO_3$ film is shown in Figure 6.2(a). The inspection of film peaks shows different Q_z values for 103 and 013 diffraction peaks, indicating an orthorhombic structure. The observation of a $GdFeO_3$-type crystal structure agrees with the reported literature [4,70,152]. Furthermore, the film diffraction peaks have identical Q_x with STO as shown in Figure 6.2(a), confirming SRO film is coherently strained. In contrast, for the Ba (8%) substituted sample, the film diffraction peaks have matching Q_z, indicating a tetragonal structural variant as in Figure 6.2(b). With the increased Ba doping level to 20%, the appearance of film diffraction peaks at identical Q_z value [see Figure 6.2(c)], establishes as tetragonal crystal symmetry but this film holds a larger film-

substrate peak separation as compared to 8% Ba-doped SRO sample. We note that the trend of identical Q_x as that of STO endorses the epitaxially strained nature of the film, ensuring excellent film quality [see Figure 6.2(c)].

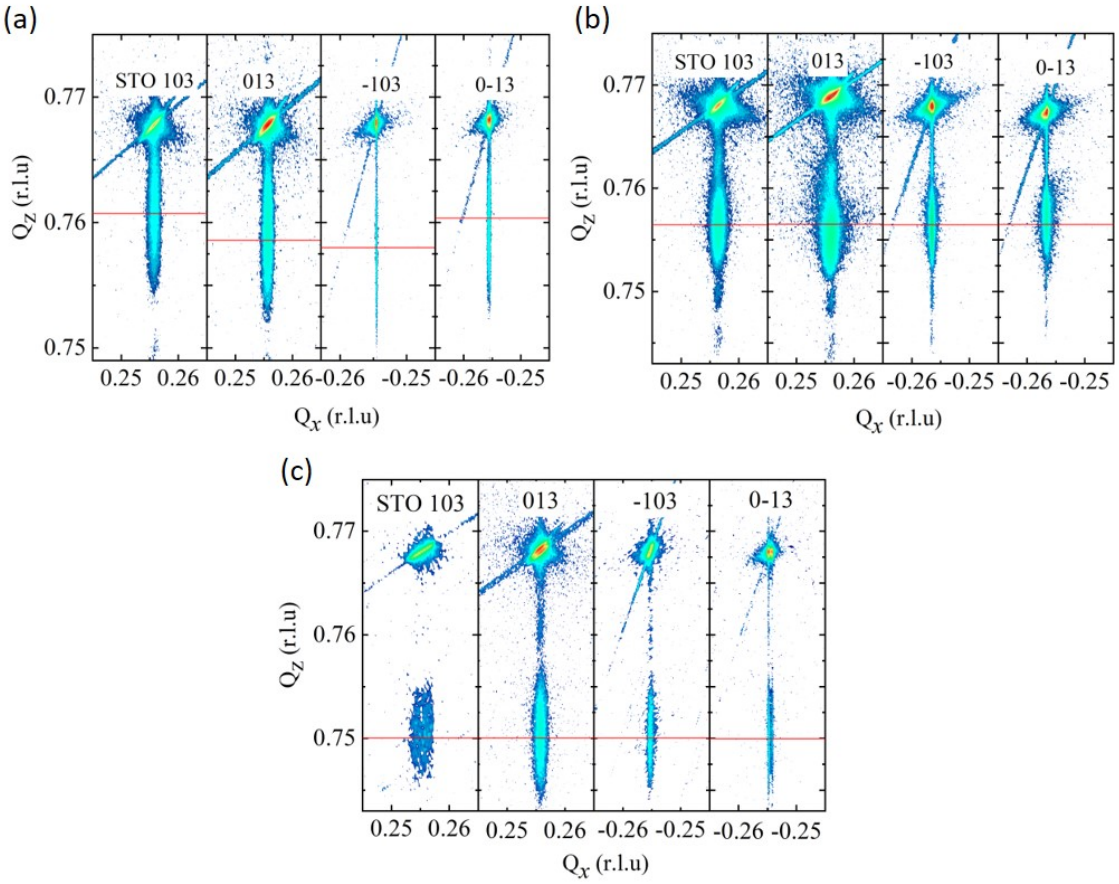

Figure 6.2. $Sr_{1-x}Ba_xRuO_3$ thin films; reciprocal space mapping (a) $x = 0$, (b) $x = 0.08$, and (c) $x = 0.2$.

6.3.2 Atomic-scale Structure and Composition

We have performed scanning transmission electron microscopy (STEM) and electron energy loss spectroscopy (EELS) to explore the atomic structure and chemical composition as shown in Figure 6.3. In STEM, the High-angle annular dark-field (HAADF) imaging contrast is dependent on atomic number (Z^2), thus HAADF mode is beneficial to visualize heavy atoms.

The high-angle-annular-dark-field (HAADF)-STEM (Z-contrast) images reveal coherent growth of high-quality $Sr_{0.92}Ba_{0.08}RuO_3$ [Figure 6.3(a-b)] and $Sr_{0.8}Ba_{0.2}RuO_3$ [Figure 6.3(d-e)]

films on the STO substrate. Importantly, the large area HAADF and highly magnified HAADF corroborate dislocation-free structures possessing coherent interfaces and of high quality. Furthermore, electron energy loss spectroscopy (EELS) elemental profiles of Ba and Sr elements laid out in Figure 6.3(c) and Figure 6.3(f). The qualitative elemental profiles were obtained by integrating EELS intensity maps from different regions. The EELS data confirms a homogeneous distribution of doped Ba in the films. The averaged Ba concentration was measured to be 0.07 ± 0.004 in the $Sr_{0.92}Ba_{0.08}RuO_3$ film [see Figure 6.3(c)] and 0.20 ± 0.017 in the $Sr_{0.8}Ba_{0.2}RuO_3$ film [see Figure 6.3(f)], which supports the desired doping concentration.

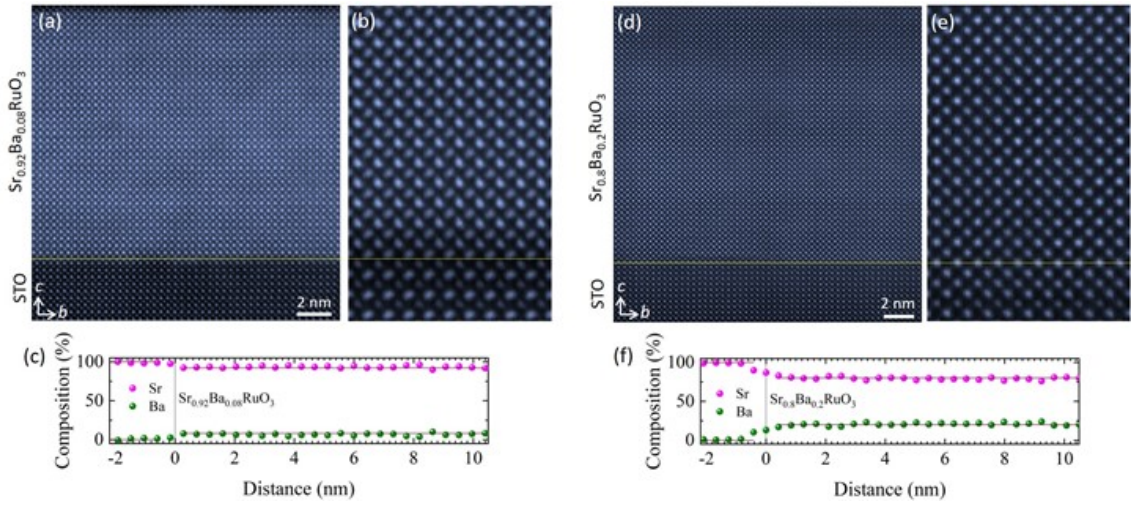

Figure 6.3. (a) Large area high-angle annular dark-field (HAADF)-STEM, and (b) highly magnified HAADF images taken along the [100]-STO direction for 8% Ba-doped SRO film. The yellow line marks the substrate-film interface. (c) Chemical composition profile of Sr (pink) and Ba (green) within 8% Ba-doped SRO film. (d) Large area HAADF-STEM, and (e) high-resolution HAADF images taken along the [100]-STO direction for 20% Ba-doped SRO film. (f) Chemical composition profile of Sr (pink) and Ba (green) within 20% Ba-doped SRO film.

6.3.3 RuO_6 Octahedron Rotations

To shed light on structural transition, we have investigated the RuO_6 octahedra rotations of $Sr_{1-x}Ba_xRuO_3$ thin films using a combination of atomically resolved scanning/transmission electron microscopy (S/TEM) and half-integer X-ray reflections. In perovskites (ABO_3), the Glazer notation [110,111] is used to describe these octahedral rotations, which describes

rotations of the octahedra about three orthogonal pseudo-cubic crystallographic axes: $[100]_{pc}$, $[010]_{pc}$, and $[001]_{pc}$. The BO_6 rotational magnitudes are specified by letters *a*, *b*, and *c*, referring to $[100]_{pc}$, $[010]_{pc}$, and $[001]_{pc}$ axes, respectively. The superscripts +, –, or 0 are used to show whether the adjacent octahedral around one axis rotate in-phase (+), out-of-phase (–), or no rotation (0). More specifically, the in-phase type rotations (+) give rise to ½ (odd-odd-even) type of reflections, while out-of-phase (–) produce ½ (odd-odd-odd) reflections [113,153].

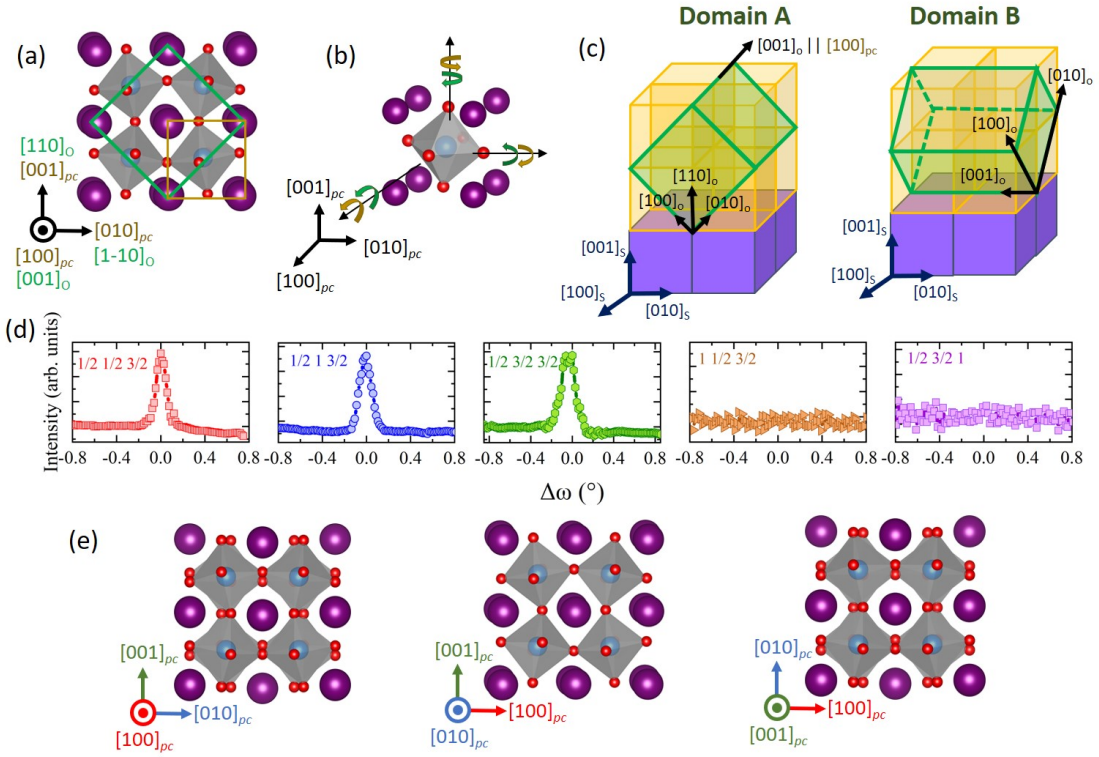

Figure 6.4. (a) Crystal structure of bulk $SrRuO_3$ (SRO). The orthorhombic (O) and pseudo-cubic (pc) unit cells are indicated by green and orange color, respectively. (b) Pseudocubic unit-cell of SRO. The octahedral rotation is in-phase along $[100]_{pc}$ ($[001]_O$), and out-of-phase about $[010]_{pc}$ ($[1\text{-}10]_O$), as well as along $[001]_{pc}$ ($[110]_O$) axes, respectively. (c) Schematic illustrations of orthorhombic SRO unit-cell orientation on a cubic $SrTiO_3$ substrate. The in-phase rotation (+) axis $[100]_{pc}$ of the film lies within the film plane, which aligns along $[100]_S$ of the substrate in Domain A, and along $[010]_S$ in Domain B. (d) Half-integer X-ray reflections for pristine SRO. (e) Representation of octahedral rotation pattern in pristine SRO film. Here, the coordinates are defined with respect to pseudocubic lattice.

Herein, the material of interest; orthorhombic $SrRuO_3$ falls into tilt system $a^+b^-c^-$ (*Pbnm* space group) as identified by the presence of an in-phase and two out-of-phase rotations [see

Figure 6.4(a-b)]. Generally, $SrRuO_3$ film on $SrTiO_3$ substrate grows in the $[110]_O$ direction, thus there are two possible orthorhombic unit-cell orientations, as given schematically in Figure 6.4(c). Consequently, the b^+ axis lies along the substrate plane with either in-phase $[100]_{pc}$ (a_p) or out-of-phase $[010]_{pc}$ (b_p) axis aligning with the $[100]_S$ (a) direction of the STO substrate, leading to a domain structure; referred as A and B [see Figure 6.4(c)]. In Domain A, the in-phase rotation (+) axis $[100]_{pc}$ (a_p) of the film lies parallel to $[100]_S$ of the substrate, i.e., ($[100]_{pc}$//$[100]_S$) [see Figure 6.4(c)]. In domain B type structure, the in-phase rotation (+) pseudo-cubic $[100]_{pc}$ (a_p) film axis is aligned with the $[010]_S$ STO-axis, and out-of-phase $[010]_{pc}$ (b_p) axis aligns parallel to the $[100]_S$ (i.e., $[010]_{pc}$//$[100]_S$) [Figure 6.4(c)]. The structure in domains A and B are equal, but with 90° rotation.

In our case, the half-angle reflections are revealed in Figure 6.4(d) establish a single domain (i.e. domain B) structure with an $a^-b^+c^-$ rotation pattern for pristine $SrRuO_3$ orthorhombic film [153,154]. As exposed in Figure 6.4(d), for pristine $SrRuO_3$, the $\left(\frac{1}{2},\frac{1}{2},\frac{3}{2}\right)$ peak reflects a^- rotation, while $\left(1,\frac{1}{2},\frac{3}{2}\right)$ absence excludes the possibility of a^+. In contrast, the $\left(\frac{1}{2},1,\frac{3}{2}\right)$ peak arises from b^+ octahedral rotation, which eliminates the existence of b^- rotations. Lastly, the occurrence of $\left(\frac{1}{2},\frac{3}{2},\frac{3}{2}\right)$ advocates c^-, while $\left(\frac{1}{2},\frac{3}{2},1\right)$ zero-peak rules out c^+ rotation. From these results; the $a^-b^+c^-$ rotation pattern is valid for $SrRuO_3$ film [153,154]. The inclination for single domain structure (i.e., type B) could be attributed to the vicinal nature of the (001)-STO substrate [41,45]. Previous studies have reported that on exactly 001-oriented STO substrate, the volume fraction for A and B-type domains could be identical, though, depending on the vicinal nature of the (001)-STO substrate, one kind of domain formation is preferred [113,114].

On other hand, the high-resolution transmission electron microscopy (HRTEM) images

and corresponding Fast Fourier Transform (FFT) patterns of 8% Ba substituted film ($Sr_{0.92}Ba_{0.08}RuO_3$) suggest the presence of coexistence of Domain A and B, suggesting that in-plane rotations are either – or +, respectively. Due to the coexisting domain A, and B structure [see Figure 6.5(a-c)], we can acquire simultaneously projected structures in $[100]_{pc}$ and $[010]_{pc}$ directions when viewing along the $[100]_S$ direction of the substrate.

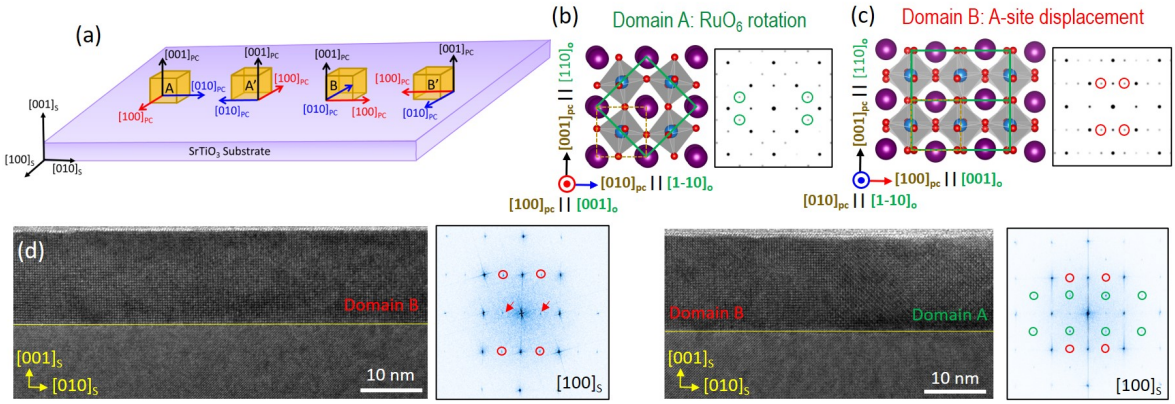

Figure 6.5. Domain structure in $Sr_{0.92}Ba_{0.08}RuO_3$ film. (a) Schematic illustration of domain structure in 8% Ba-doped SRO film grown on STO substrate. In Domain A, the in-phase rotation (+) axis $[100]_{pc}$ (marked in red) of the film lies within the plane, which aligns along $[100]_S$ of the substrate in Domain A, and along $[010]_S$ in Domain B. The subscript pc refers to pseudo-cubic structure of the film, and the subscript s refers to cubic structure of the substrate. (b-c) Projected crystal structures and simulated electron diffraction patterns in the $[100]_{pc}$ (Domain A) and $[010]_{pc}$ (Domain B) directions. (d-e) HRTEM image with electron beam incident along the $[100]_S$ direction, and corresponding Fast Fourier Transform (FFT) patterns with characteristic fractional spots marked in red (Domain B) and green (Domain A), respectively. The forbidden spots marked by the arrows, absent in the simulated electron diffractions, were observed due to multiple scattering of the electron and sample.

Figure 6.5(d-e) depicts HRTEM images and corresponding FFT patterns, which are in accordance with the simulated diffraction patterns in the $[100]_{pc}$ (Domain A) and $[010]_{pc}$ (Domain B) directions [see Figure 6.5(b-c)]. The two-domain structures could be distinguished by the presence of characteristic diffraction spots marked as green and red in Figure 6.5(d-e). Generally, the structural domain size can range from tens to hundreds of nanometers [112]. Our TEM observation of 8% Ba doped SRO reveals that the majority of regions are Domain B ($[010]_{pc}//[100]_S$) with a rotation pattern of $a^-b^+c^-$, while only a minor portion of regions are

Domain A ($[100]_{pc}$//$[100]_S$), i.e., a rotation of type $a^+b^-c^-$. The preference for Domain B-type structures could be attributed to STO substrate vicinality since the modified miscut angle and topography of substrate step edges would tend to transform the alignment of the orthorhombic longer c-axis alignment [113,114].

The structure of domains A and B is identical, but when along the $[001]_S$ direction, as in Figure 6.5(b-c), we can observe simultaneously the RuO_6 tilt in domain A, and A-site cation displacement in Domain B. The quantitative analysis of A-site atomic displacements exhibits a value of less than ~ 0.1 Å versus the bulk $SrRuO_3$ (0.12 Å), indicative of suppressed tilt/rotation angle along the in-plane direction. In addition, under a compressively strained scenario, we have the following condition: $a_p = b_p < c_p$ (tetragonal symmetry), hence to have considerably smaller a_p and b_p compared to c_p, the octahedron rotations magnitude along two in-plane axes (a_p and b_p) would be diminished reduced [113]. Considering the preceding discussion, we argue that 8% Ba-doped SRO film holds a tetragonal symmetry with the majority of film occupying an $a^-b^+c^-$ (domain B) rotation pattern, but possessing a diminished octahedral rotation magnitude (only a minor portion of film is domain A with $a^+b^-c^-$). In other words, the 8% Ba-introduction in SRO lattice under epitaxial strain results in a modification of crystal symmetry and octahedral rotation magnitude but does not alter octahedral rotation pattern.

To investigate the crystal structure of $Sr_{0.8}Ba_{0.2}RuO_3$ film, we have obtained HRTEM images across [100] and [210] STO-substrate directions, as revealed in Figure 6.6(a-d). The FFT results [see Figure 6.6(a-d)] obtained from HRTEM images confirms the absence of fractional spots, indicating a cubic structure. This is also evident annular-bright-field STEM image [see Figure 6.6(e)], where oxygen atoms forming a cubic symmetry with no tilt/rotation could be realized, corroborating a cubic structural symmetry. Furthermore, the half-integer reflection results revealed in Figure 6.6(e) suggests diminishing of corresponding peaks, supporting an

$a^0b^0c^0$ tilt system, which is in agreement with STEM imaging. Overall, STEM structural analysis combined with half-integer X-ray measurements advocates an $a^0b^0c^0$ tilt system, establishing a non-rotational octahedron symmetry typically observed in cubic-type perovskites. We note that for $Sr_{0.8}Ba_{0.2}RuO_3$ film, due to compressive epitaxial strain, the out-of-plane lattice expands, while the in-plane lattice parameter is locked with STO (i.e., $a_{pc} = b_{pc} < c_{pc}$), this leads to the formation of purely tetragonal structure (cubic-type) without any octahedral rotations: $a^0b^0c^0$; *Pm-3m*.

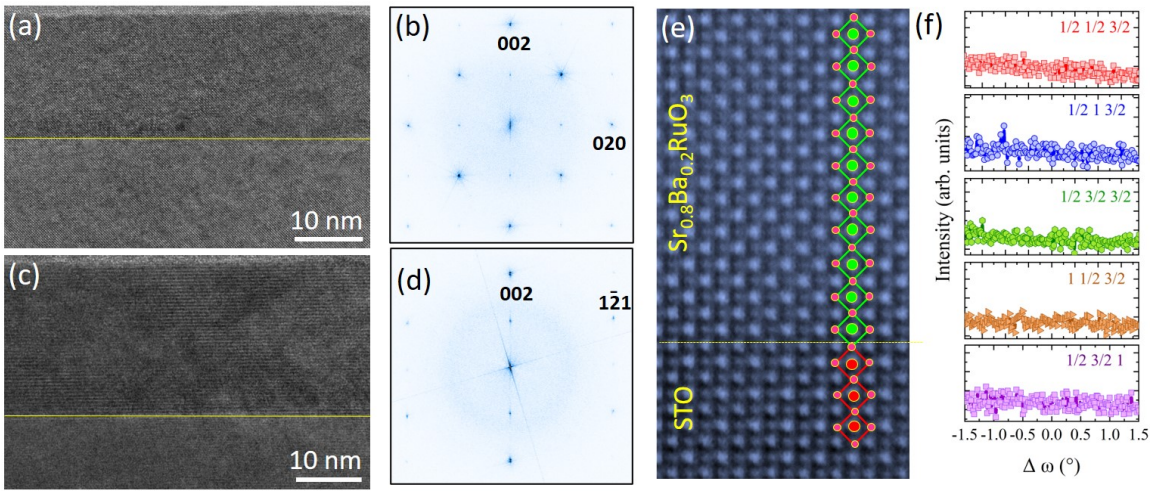

Figure 6.6. Crystal structure of $Sr_{0.8}Ba_{0.2}RuO_3$ film determined via S/TEM. (a) High-resolution transmission electron microscope (HRTEM) image taken along the [100] direction, and (b) the corresponding FFT pattern. (c) HRTEM image with (d) Fast Fourier Transform (FFT) pattern taken along the [210] direction. The FFT patterns are indexed using the notation of the pseudo-cubic structure. (e) Highly-magnified annular-bright-field (ABF) STEM image taken along the [100] direction with projected structural model superimposed. The yellow line marks the TiO_2-(Sr/Ba)O interface. In panel (e), non-octahedra tilt across the interfaces could be observed. (f) Half-integer X-ray reflections for $Sr_{0.8}Ba_{0.2}RuO_3$ film.

6.3.4 Magnetometry

In the following, we proceed to investigate the effects of structural symmetry on the physical properties of $Sr_{1-x}Ba_xRuO_3$ thin films. Figure 6.7 displays temperature-dependent magnetization [M(T)] and magnetic hysteresis [M(H)] of $Sr_{1-x}Ba_xRuO_3$ thin films obtained along three directions with respect to STO substrate: two in-plane directions; [100] and [010] and out

of plane [001] direction. The purely orthorhombic SRO film shows a sharp paramagnetic to ferromagnetic transition in M(T) near ~145 K holding a perpendicular magnetic anisotropy as shown in M(T) and M(H), where the easy axis resides along out of plane [001] direction as in Figure 6.7(a-b). This agrees with previous results [113,153,155–157]. We also observed an in-plane magnetic anisotropy, which is associated with different octahedral rotations along in-plane directions ($a^{-}b^{+}c^{-}$).

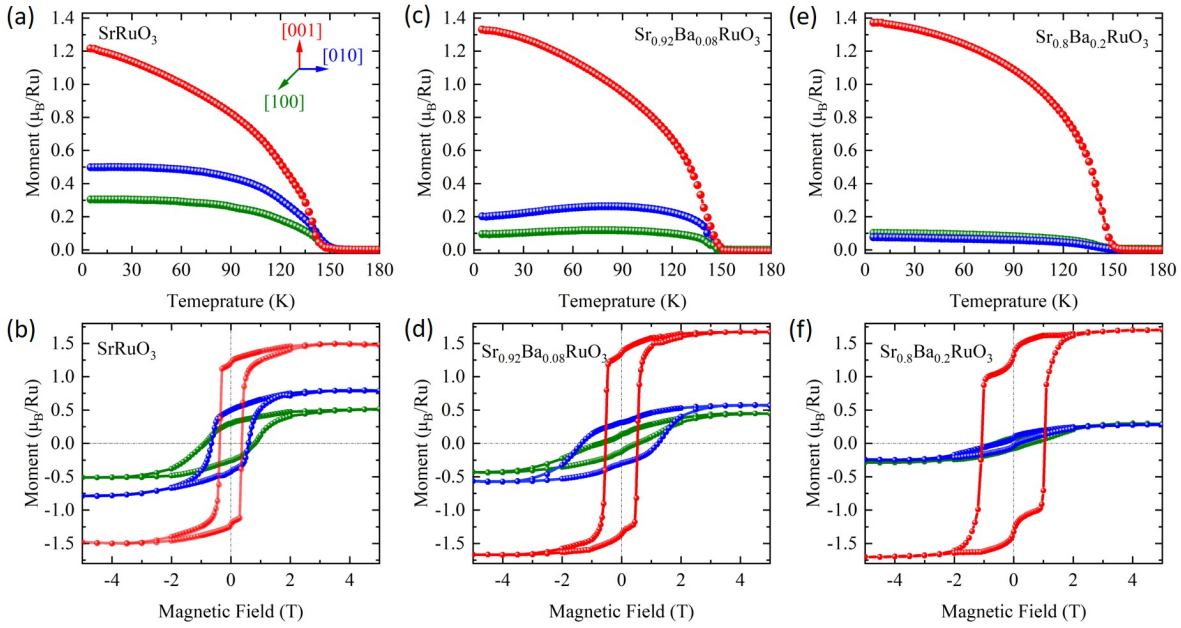

Figure 6.7. Magnetization as a function of temperature [M(T)], and magnetic field [M(H)] for the family of $Sr_{1-x}Ba_xRuO_3$ thin films. (a)-(b) $SrRuO_3$, (c)-(d) $Sr_{0.92}Ba_{0.08}RuO_3$, and (e)-(f) $Sr_{0.8}Ba_{0.2}RuO_3$. For M(T), the samples are cooled down in 2000 Oe to 5 K, and in the second step, in presence of 100 Oe, the data is collected during warm-up.

In contrast, the $Sr_{0.92}Ba_{0.08}RuO_3$ tetragonal variant film reveals suppression of magnetic moments across two in-plane directions, while maintaining an out-of-plane easy magnetization axis [see Figure 6.7(c-d)]. Interestingly, under structural transformation to purely tetragonal (cubic-type with no octahedral rotations: $a^0b^0c^0$) form in $Sr_{0.8}Ba_{0.2}RuO_3$ film, the system still exhibits robust ferromagnetism (T_c ~145 K) with greatly enhanced perpendicular magnetic anisotropy (PMA) [see Figure 6.7(e-f)]. Moreover, the alignment of the magnetic spins along

two in-plane moments is highly suppressed, leading to an isotropic in-plane magnetic response in $Sr_{0.8}Ba_{0.2}RuO_3$ film [see Figure 6.7(e-f)]. The observed magnetic behavior is attributed to purely tetragonal structural symmetry ($a^0b^0c^0$) such that the easy magnetization axis is more aligned with the out-of-plane axis.

6.3.5 Electron Transport

Further, to investigate the itinerancy of $Sr_{1-x}Ba_xRuO_3$ thin films, the temperature-dependent resistivity [ρ(T)] measurement is revealed in Figure 6.8(a).

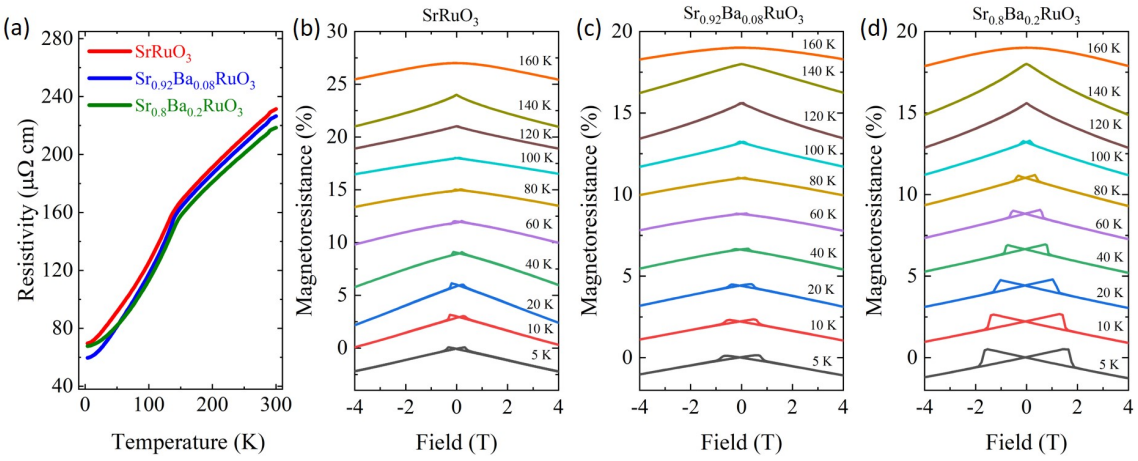

Figure 6.8. (a) $Sr_{1-x}Ba_xRuO_3$ thin films, temperature-dependent resistivity. Magnetoresistance (MR) was measured at different temperatures of (b) $SrRuO_3$, (c) $Sr_{0.92}Ba_{0.08}RuO_3$, and (d) $Sr_{0.8}Ba_{0.2}RuO_3$ thin films with a magnetic field applied along out-of-plane direction.

All films exhibit a metallic behavior of decreasing resistivity with temperature and undergo a paramagnetic to ferromagnetic transition as revealed by a kink in ρ(T) as in Figure 6.8(a). Additionally, we have measured the magnetoresistance: MR =$[R(6T) - R(0)]/R(0)$, where R(6 T), and R(0) are the resistances at a magnetic field of 6 T, and 0 T, respectively. We note that for non-magnetic systems, the MR holds a parabolic shape, while FM systems show a negative, non-parabolic MR. In our case, the presence of hysteretic MR at the lowest temperature 5 K, indeed confirms the presence of robust ferromagnetic ordering in $SrRuO_3$, $Sr_{0.92}Ba_{0.08}RuO_3$, and $Sr_{0.8}Ba_{0.2}RuO_3$ thin films [see Figure 6.8(b-d)]. It could be seen that the MR magnetic

hysteresis endures up to 90-100 K, whereas above a non-parabolic MR persists up to ~145 K. These observations show that systems hold a magnetic order up to ~ 145 K, supporting the SQUID magnetometry.

6.3.6 Hall Transport

Furthermore, for samples under study, we discuss the Anomalous Hall effect (AHE), which describes intrinsic magnetization. The total hall or transverse resistance is specified as $R_{xy} = R_0 H + R_A M$. Here, the first term (R_0H) signifies the ordinary Hall component arising from Lorentz force contribution with R_0 being the ordinary Hall coefficient and H the magnetic field. The second term ($R_{AHE} = R_A M$) indicates the anomalous contribution, where R_A is the anomalous Hall coefficient, and M is the magnetization. For clarification of the anomalous component, we subtracted the ordinary Hall term by linear fitting, which is obtained from the total hall resistance versus the applied field curve in the high field's regime. The anomalous contribution measured at different temperatures for the series of $Sr_{1-x}Ba_xRuO_3$ (x = 0, 0.08, and 0.2) thin films is shown in Figure 6.9.

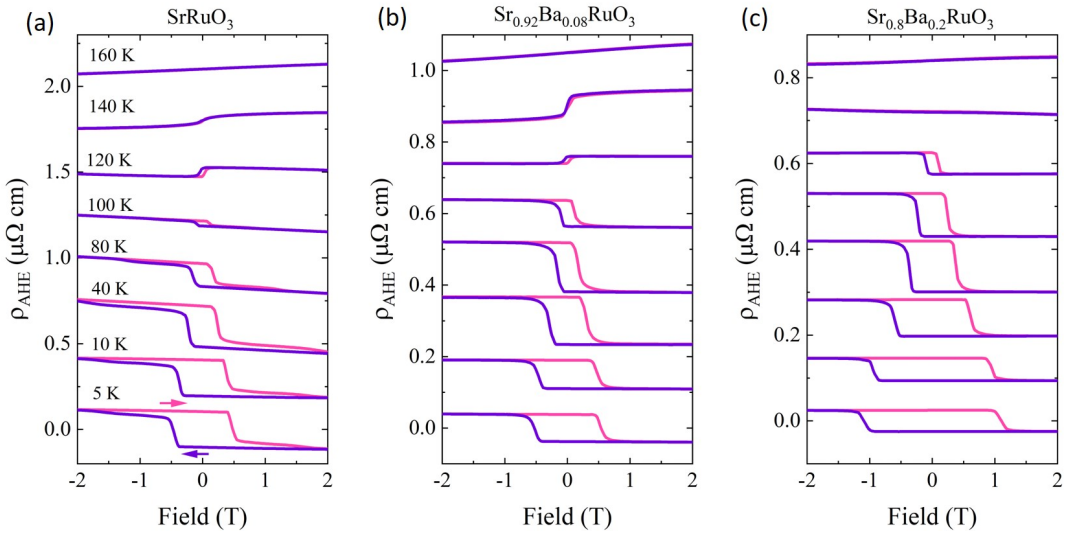

Figure 6.9. Anomalous Hall resistivity of (a) $SrRuO_3$, (b) $Sr_{0.92}Ba_{0.08}RuO_3$, and (c) $Sr_{0.8}Ba_{0.2}RuO_3$ thin films.

For, films under study, the reversed hysteretic curve at the lowest temperatures signifies a

robust FM order encompassing a negative R_A [see Figure 6.9(a)]. The $SrRuO_3$ ($x = 0$) film displays an inverted magnetic hysteresis loop till 100 K, while at high temperatures at 100 K, a sign reversal occurs as in Figure 6.9(a). Comparable hall structure with pronounced inverted squarish shape hysteresis at low temperatures, signifying strong ferromagnetism could be seen $Sr_{0.92}Ba_{0.08}RuO_3$ [Figure 6.9(b)] for and $Sr_{0.8}Ba_{0.2}RuO_3$ [Figure 6.9(c)] films.

6.3.7 Ferromagnetism versus Ba-substitution

Finally, we discuss the evolution of ferromagnetism and T_c in a series of $Sr_{1-x}Ba_xRuO_3$ as presented in Figure 6.10. The pristine SRO possesses a T_c of 145 K, while the tetragonally distorted variant 8%-Ba-doped SRO film demonstrates a little enhanced T_c of 149 K.

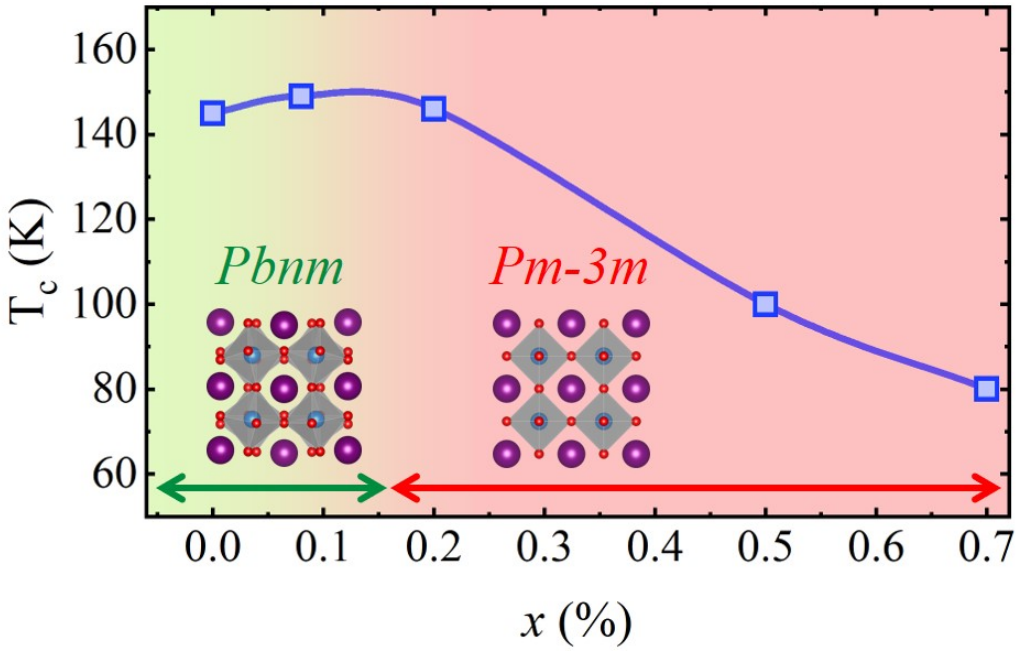

Figure 6.10. Phase diagram of T_c in series of $Sr_{1-x}Ba_xRuO_3$ thin films as function of Ba-concentration (x).

Remarkably, in purely tetragonal form (cubic-type octahedral rotations: $a^0b^0c^0$), the $Sr_{0.8}Ba_{0.2}RuO_3$ film without octahedral rotations and flat Ru-O-Ru bond angle has nearly identical T_c ~145 K as compare to the orthorhombic variant. However, the increased Ba concentration to 50% Ba, while retaining a cubic [*Pm-3m*: $a^0b^0c^0$] phase results in a suppression

of the ferromagnetism and T_c ~100 K, which reduces further to 80 K for 70 % Ba. This suggests, even though the structure remains in a higher symmetry regime (cubic), the introduction of more Ba introduces some subtle changes in electronic and magnetic structure, which condenses the ferromagnetic order.

In the 4d perovskite ruthenates $ARuO_3$ (A= Ba, Ca, or Sr) family, the magnetic ordering is explained via the Stoner picture [13–15,158]. Mazin and Singh [14] showed that $SrRuO_3$ in an idealized cubic symmetry displays a van Hove singularity in the Fermi-level density of states $D(E_F)$ primarily due to flat Ru $4dt_{2g}$ bands hybridized with O-2p bands. Though imposing an orthorhombically distorted structure lifts the degeneracy from Ru $4d\ t_{2g}$ states, leading to a reduction in Ru 4d-O-2p overlap accompanied with slight bandwidth narrowing and a small splitting of the van Hove peak. In $SrRuO_3$, comparatively smaller $GdFeO_3$-type distortions as oppose to $CaRuO_3$ are considered ideal for the indirect exchange magnetic interactions, leading to FM metal (T_c ~ 160 K) [9,17]. Under, this model, a maximized T_c, even higher than $SrRuO_3$ is projected in a crystal symmetry with a flat Ru-O-Ru bond angle of 180° [14,29,135]. Though, in our case, we have revealed that orthorhombically distorted pristine $SrRuO_3$ film and purely tetragonal $Sr_{0.8}Ba_{0.2}RuO_3$ film with a *Pm-3m* ($a^0b^0c^0$) symmetry have nearly identical T_c. However, the increased Ba concentration significantly reduces the T_c [see Figure 6.10]. In $Sr_{1-x}Ba_xRuO_3$ series, the final member: $BaRuO_3$ encompasses larger bond lengths: ⟨Ba-O⟩ =2.832 Å and ⟨Ba-O⟩ = 2.003 Å (versus bulk $SrRuO_3$: ⟨Sr-O⟩ =2.780 Å and ⟨Ru-O⟩ = 1.984 Å) [135]. As a result of increased elongation of the Ru-O bond, it is highly probable that Ru-O orbital overlap decreases and leads to a reduction in the exchange energy. The exchange is related to both the Ru-O-Ru bond angle and the Ru-O bond length. Thus, even though the Ru-O-Ru bond is flat (180°), the increased Ru-O bond length probably leads to a contrasting effect of weakening the Ru-O orbital hybridization. The Ru-O bonding is important since in SRO ~70% of the net

ordered moments are associated with the Ru-site and the remaining magnetism resides on the O sites [13,14,159]. This effect is also observed in the ferromagnetic manganites, where $(La,Ba)MnO_3$ has a lower ordering temperature than $(La,Sr)MnO_3$ [160]. Despite having a straighter octahedral bond angle (180°), the opposing effect of B-O bond length expansion outcomes in a MnO orbital overlap reduction, which decreases the ferromagnetic transition temperature. Therefore, the B-site cation and oxygen atom bonding nature and bond length become more important than the octahedral bond angle. The results provide a direct confirmation that besides determining octahedral distortion, the A-site introduces certain entangled electro-magnetic effects that greatly affect the ruthenates magnetic ordering.

6.4 Conclusion

In conclusion, we fabricated the $Sr_{1-x}Ba_xRuO_3$ thin films. Here, we have shown that with varying degrees of Ba substitution in $SrRuO_3$ under epitaxial strain a cubic-like crystal structure with non-rotational RuO_6 unit geometry commonly could be formed. The epitaxially stabilized cubic-type ruthenate system is ferromagnetically ($T_c \sim 145$ K) ordered with a strong perpendicular magnetic anisotropy. Our results demonstrate the importance of octahedral unit structure in determining the electromagnetic properties of ruthenates. Moreover, the investigation provides an essential understanding of ruthenates ferromagnetism, indicating sensitivity to A-site and advocating the A-O and Ru-O orbital hybridization importance.

Chapter 7. Summary of Findings and Outlook

In Chapter 4 of this thesis, I presented a systematic study on ultrathin epitaxial ruthenate oxide: $SrRuO_3$ (SRO); spatially confined between $SrTiO_3$ (STO) i.e., STO^5-SRO^n-STO^5 with n = 1- and 2-unit cells. Our experimental results demonstrate that the STO^5-SRO^1-STO^5 film is nonmagnetic and insulating. The RuO_6 octahedra network in STO^5-SRO^1-STO^5 is governed by STO cubic structure without any octahedral tilt or rotational distortion. However, once the SRO thickness is increased to 2-unit cells, the system becomes ferromagnetic-metal but retains a non-tilted octahedral symmetry, thus excluding the role of the lattice structure. Our atomically resolved spectroscopy demonstrates that STO^5-SRO^1-STO^5 heterostructure displays a Ru-Ti intermixing in the RuO_2 layer compared to STO^5-SRO^2-STO^5. Density-functional-theory calculations support that stoichiometric n = 1 and n = 2 heterostructures are metallic and ferromagnetic with no octahedral tilts, while non-stoichiometry in the Ru sublattice in the n = 1 case opens an energy gap and induces antiferromagnetic ordering. Thus, the results designate that the non-stoichiometry is the cause of the observed loss of metallicity and ferromagnetism in the n = 1 case. The results highlight the role of non-stoichiometry and interface-induced intermixture in determining the functionality of spatially confined materials. To that end, it is imperative to develop film growth methodology via which the interface-induced intermixture and non-stoichiometric effects could be minimized.

In Chapter 5, we report the emergence of unusual, thickness-dependent properties in ultrathin $CaRuO_3$ (CRO) films by unique insertion of a single isovalent SrO layer (referred to as "δ-doping"). While bulk $CaRuO_3$ holds a metallic and nonmagnetic nature, the thin-films of CRO confined to a thickness of ~15-unit cells (u.c.) become insulating, while retaining a nonmagnetic state. The 15 u.c. (CRO15) film is identified to be fully insulating, where it exhibits Efros-variable range hopping at low temperatures. In contrast, the δ-doping to the middle of such

$CaRuO_3$ film induces an insulator-to-metal transition and enhancement of conductivity. The δ-doping of CRO films not only triggers the enhancement of conductivity but also induces a pronounced ferromagnetic order revealed by magnetoresistance (MR). The atomically resolved imaging exposes that the whole δ-doped film preserves the bulk-$CaRuO_3$ orthorhombic structure, while a small local structural modification is present in the SrO layer. The density functional theory calculations support that the SrO layer can cause a modulation on the adjacent Ru t_{2g} bands, highlighting the presence of highly local subtle electronic and structural effects introduced via Ca/Sr replacement. The outcomes highlight the delicate nature of magnetic ordering in $CaRuO_3$ and entangled effects that can alter it, especially the role of A-site cation in electronic and magnetic structure in addition to lattice distortion in ruthenates.

Considering that we observed a metal-to-insulator transition governed by disordering effects, in this regard, the DFT calculations cannot catch up with the essence of such observed emergent behavior, thus calculations beyond standard methods are required. Moreover, one key question to address is to explore experimentally whether the δ-doping trigged ferromagnetic ordering is highly local near the SrO layer or the effects extend into the CRO film. Experimental investigations via techniques such as X-ray circular and linear dichroism and Lorentz microscopy could be utilized to explore the magnetic structure. Moreover, the next step would be to utilize different substrates and explore the effect of compressive versus tensile strain on film properties. The methodology explained in Chapter 5 could be utilized to explore the correlated system's electronic and magnetic nature through heterostructure architecture.

Lastly, in Chapter 6, we demonstrate an unusual tuning of crystal lattice symmetry in pristine $SrRuO_3$, achieved via epitaxial-strain stabilized Ba substitution. Using strain stabilized Ba implantation in $SrRuO_3$, the crystal symmetry could be continuously transmuted from bulk-like orthorhombic to cubic-like phase. The cubic film exhibits robust ferromagnetic ordering (T_c

= 145 K) with a strong perpendicular magnetic anisotropy. However, increased Ba implantation dramatically diminishes the T_c, while the system retains a cubic form. This suggests, that even though the structure remains in a higher symmetry regime (cubic), the introduction of more Ba introduces some subtle changes in electronic and magnetic structure, which condenses the ferromagnetic order. The outcomes provide a direct confirmation that besides determining octahedral distortion, the A-site introduces certain entangled electromagnetic effects, that greatly affect the Ru-O hybridization, leading to a profound effect on the ruthenates magnetic ordering.

In this dissertation work, we have explored how heterostructure engineering could be employed effectively to control and isolate the several significant parameters that contribute to the emergent electromagnetic phenomena in perovskite ruthenate oxides.

Appendix. Copyright Information

American Physical Society
Reuse and Permissions License

25-Sep-2022

This license agreement between the American Physical Society ("APS") and Zeeshan Ali ("You") consists of your license details and the terms and conditions provided by the American Physical Society and SciPris.

Licensed Content Information

License Number:	RNP/22/SEP/058319
License date:	25-Sep-2022
DOI:	10.1103/PhysRevB.105.054429
Title:	Origin of insulating and nonferromagnetic ${\mathrm{SrRuO}}_{3}$ monolayers
Author:	Zeeshan Ali et al.
Publication:	Physical Review B
Publisher:	American Physical Society
Cost:	USD $ 0.00

Request Details

Does your reuse require significant modifications: No

Specify intended distribution locations:	Worldwide
Reuse Category:	Reuse in a thesis/dissertation
Requestor Type:	Student
Items for Reuse:	Whole Article
Format for Reuse:	Electronic

Information about New Publication:

University/Publisher:	Louisiana State University
Title of dissertation/thesis:	CONTROLLING ELECTRO-MAGNETIC FUNCTIONALITY OF RUTHENATES BY HETEROSTRUCTURE DESIGN
Author(s):	Zeeshan Ali
Expected completion date:	Dec. 2022

License Requestor Information

Name:	Zeeshan Ali
Affiliation:	Individual
Email Id:	zee89ali@gmail.com
Country:	United States

References

[1] R. J. D. Tilley, Perovskites : Structure-Property Relationships (John Wiley & Sons, 2016).

[2] G. Koster, M. Huijben, and G. Rijnders, Epitaxial Growth of Complex Metal Oxides, 1st ed. (Woodhead Publishing, 2015).

[3] A. M. Glazer, Simple Ways of Determining Perovskite Structures, Acta Crystallogr. Sect. A **31**, 756 (1975).

[4] A. Vailionis, W. Siemons, and G. Koster, Room Temperature Epitaxial Stabilization of a Tetragonal Phase in $ARuO_3$ (A=Ca and Sr) Thin Films, Appl. Phys. Lett. **93**, 051909 (2008).

[5] A. Vailionis, H. Boschker, W. Siemons, E. P. Houwman, D. H. A. Blank, G. Rijnders, and G. Koster, Misfit Strain Accommodation in Epitaxial ABO_3 Perovskites: Lattice Rotations and Lattice Modulations, Phys. Rev. B **83**, 064101 (2011).

[6] D. Kan, R. Aso, R. Sato, M. Haruta, H. Kurata, and Y. Shimakawa, Tuning Magnetic Anisotropy by Interfacially Engineering the Oxygen Coordination Environment in a Transition Metal Oxide, Nat. Mater. **15**, 432 (2016).

[7] Z. Liao, M. Huijben, Z. Zhong, N. Gauquelin, S. Macke, R. J. Green, S. Van Aert, J. Verbeeck, G. Van Tendeloo, K. Held, G. A. Sawatzky, G. Koster, and G. Rijnders, Controlled Lateral Anisotropy in Correlated Manganite Heterostructures by Interface-Engineered Oxygen Octahedral Coupling, Nat. Mater. **15**, 425 (2016).

[8] J. M. Rondinelli, S. J. May, and J. W. Freeland, Control of Octahedral Connectivity in Perovskite Oxide Heterostructures: An Emerging Route to Multifunctional Materials Discovery, MRS Bull. 2012 373 **37**, 261 (2012).

[9] A. Callaghan, C. W. Moeller, and R. Ward, Magnetic Interactions in Ternary Ruthenium Oxides, Inorg. Chem. **5**, 1572 (1966).

[10] W. Lu, W. Song, P. Yang, J. Ding, G. M. Chow, and J. Chen, Strain Engineering of Octahedral Rotations and Physical Properties of $SrRuO_3$ Films, Sci. Rep. **5**, 1 (2015).

[11] B. J. Kennedy and B. A. Hunter, High-Temperature Phases of $SrRuO_3$, Phys. Rev. B **58**, 653 (1998).

[12] G. Koster, L. Klein, W. Siemons, G. Rijnders, J. S. Dodge, C. B. Eom, D. H. A. Blank, and M. R. Beasley, Structure, Physical Properties, and Applications of $SrRuO_3$ Thin Films, Rev. Mod. Phys. **84**, 253 (2012).

[13] J. M. Rondinelli, N. M. Caffrey, S. Sanvito, and N. A. Spaldin, Electronic Properties of Bulk and Thin Film $SrRuO_3$: Search for the Metal-Insulator Transition, Phys. Rev. B **78**, 155107 (2008).

[14] I. I. Mazin and D. J. Singh, Electronic Structure and Magnetism in Ru-Based Perovskites, Phys. Rev. B **56**, 2556 (1997).

[15] K. Maiti, Role of Covalency in the Ground-State Properties of Perovskite Ruthenates: A First-Principles Study Using Local Spin Density Approximations, Phys. Rev. B **73**, 235110 (2006).

[16] S. Thomas, B. Kuiper, J. Hu, J. Smit, Z. Liao, Z. Zhong, G. Rijnders, A. Vailionis, R. Wu, G. Koster, and J. Xia, Localized Control of Curie Temperature in Perovskite Oxide Film by Capping-Layer-Induced Octahedral Distortion, Phys. Rev. Lett. **119**, 177203 (2017).

[17] G. Cao, S. McCall, M. Shepard, J. Crow, and R. Guertin, Thermal, Magnetic, and Transport Properties of Single-Crystal, Phys. Rev. B - Condens. Matter Mater. Phys. **56**, 321 (1997).

[18] J. P. Carlo, T. Goko, I. M. Gat-Malureanu, P. L. Russo, A. T. Savici, A. A. Aczel, G. J. MacDougall, J. A. Rodriguez, T. J. Williams, G. M. Luke, C. R. Wiebe, Y. Yoshida, S. Nakatsuji, Y. Maeno, T. Taniguchi, and Y. J. Uemura, New Magnetic Phase Diagram of $(Sr,Ca)_2RuO_4$, Nat. Mater. **11**, 323 (2012).

[19] G. Cao, O. Korneta, S. Chikara, L. E. DeLong, and P. Schlottmann, Non-Fermi-Liquid Behavior in Single-Crystal $CaRuO_3$: Comparison to Ferromagnetic $SrRuO_3$, Solid State Commun. **148**, 305 (2008).

[20] K. Yoshimura, T. Imai, T. Kiyama, K. R. Thurber, A. W. Hunt, and K. Kosuge, ^{17O}NMR Observation of Universal Behavior of Ferromagnetic Spin Fluctuations in the Itinerant Magnetic System $Sr_{1-x}Ca_xRuO_3$., Phys. Rev. Lett. **83**, 4397 (1999).

[21] A. Maignan, B. Raveau, V. Hardy, N. Barrier, and R. Retoux, Ferromagnetism Induced by Chromium Substitution in the $CaRuO_3$ Perovskite, Phys. Rev. B **74**, 024410 (2006).

[22] V. Durairaj, S. Chikara, X. N. Lin, A. Douglass, G. Cao, P. Schlottmann, E. S. Choi, and R. P. Guertin, Highly Anisotropic Magnetism in Cr-Doped Perovskite Ruthenates, Phys. Rev. B **73**, 214414 (2006).

[23] T. He and R. J. Cava, Disorder-Induced Ferromagnetism in $CaRuO_3$, Phys. Rev. B **63**, 172403 (2001).

[24] S. Tripathi, R. Rana, S. Kumar, P. Pandey, R. S. Singh, and D. S. Rana, Ferromagnetic $CaRuO_3$, Sci. Rep. **4**, 3877 (2015).

[25] S. Kumar, S. Tripathi, E. V. Phanendra, R. S. Singh, and D. S. Rana, Giant Ferromagnetism and Exchange Bias in Tensile Strained and Cr Modified $CaRuO_3$ Thin Films, Appl. Phys. Lett. **104**, 4 (2014).

[26] A. T. Zayak, X. Huang, J. B. Neaton, and K. M. Rabe, Manipulating Magnetic Properties of $SrRuO_3$ and $CaRuO_3$ with Epitaxial and Uniaxial Strain, Phys. Rev. B **77**, 214410 (2008).

[27] H. Mukuda, K. Ishida, Y. Kitaoka, K. Asayama, R. Kanno, and M. Takano, Spin Fluctuations in the Ruthenium Oxides RuO_2, $SrRuO_3$, $CaRuO_3$, and Sr_2RuO_4 Probed by Ru NMR, Phys. Rev. B - Condens. Matter Mater. Phys. **60**, 12279 (1999).

[28] K. Maiti and R. S. Singh, Evidence against Strong Correlation in 4d Transition-Metal Oxides $CaRuO_3$ and $SrRuO_3$, Phys. Rev. B - Condens. Matter Mater. Phys. **71**, 161102 (2005).

[29] C. Q. Jin, J. S. Zhou, J. B. Goodenough, Q. Q. Liu, J. G. Zhao, L. X. Yang, Y. Yu, R. C. Yu, T. Katsura, A. Shatskiy, and E. Ito, High-Pressure Synthesis of the Cubic Perovskite BaRuO3 and Evolution of Ferromagnetism in $ARuO_3$ (A = Ca, Sr, Ba) Ruthenates, Proc. Natl. Acad. Sci. U. S. A. **105**, 7115 (2008).

[30] B. D. Cullity and C. D. Graham, Introduction to Magnetic Materials (IEEE/Wiley, 2008).

[31] S. Blundell, Magnetism in Condensed Matter (Oxford University Press, 2001).

[32] M. Reis, Fundamentals of Magnetism (Elsevier Inc., 2013).

[33] N. F. (Nevill F. Mott, Metal-Insulator Transitions (Taylor & Francis, London ;;New York :, 1990).

[34] M. Imada, A. Fujimori, and Y. Tokura, Metal-Insulator Transitions, Rev. Mod. Phys. **70**, 1039 (1998).

[35] E. Morintale, C. Constantinescu, and M. Dinescu, Thin Films Development by Pulsed Laser-Assisted Deposition, Ann. Univ. Craiova, Phys. **20**, 43 (2010).

[36] J. Shen, Z. Gai, and J. Kirschner, Growth and Magnetism of Metallic Thin Films and Multilayers by Pulsed-Laser Deposition, Surf. Sci. Rep. **52**, 163 (2004).

[37] R. Eason, Pulsed Laser Deposition of Thin Films : Applications-Led Growth of Functional Materials (Wiley-Interscience, 2007).

[38] M. Volmer and A. Weber, Keimbildung in Übersättigten Gebilden, Zeitschrift Für Phys. Chemie **119U**, 277 (1926).

[39] F. C. Frank and J. H. van der Merwe, One-Dimensional Dislocations. II. Misfitting Monolayers and Oriented Overgrowth, Proc. R. Soc. A Math. Phys. Eng. Sci. **198**, 216 (1949).

[40] I. N. Stranski and L. Krastanow, Zur Theorie Der Orientierten Ausscheidung von Ionenkristallen Aufeinander, Monatshefte Für Chemie **71**, 351 (1937).

[41] K. Oura, M. Katayama, A. V. Zotov, V. G. Lifshits, and A. A. Saranin, Surface Science (Springer Berlin Heidelberg, Berlin, Heidelberg, 2003).

[42] Z. Cao, Thin Film Growth : Physics, Materials Science and Applications (Woodhead Pub Ltd, 2011).

[43] C. Kittel, Introduction to Solid State Physics (Wiley, Hoboken, NJ, 2005).

[44] M. Lee, X-Ray Diffraction for Materials Research (Apple Academic Press, 2017).

[45] Z. Ali, Growth, Transport, and Magnetic Properties of Oblique-Angle-Deposited Permalloy Thin Films, Miami University, 2018.

[46] Physical Property Measurement System Hardware Manual.

[47] A. Brinkman, M. Huijben, M. Van Zalk, J. Huijben, U. Zeitler, J. C. Maan, W. G. Van Der Wiel, G. Rijnders, D. H. A. Blank, and H. Hilgenkamp, Magnetic Effects at the Interface between Non-Magnetic Oxides, Nat. Mater. **6**, 493 (2007).

[48] P. Zubko, S. Gariglio, M. Gabay, P. Ghosez, and J.-M. Triscone, Interface Physics in Complex Oxide Heterostructures, Annu. Rev. Condens. Matter Phys. **2**, 141 (2011).

[49] A. Bhattacharya and S. J. May, Magnetic Oxide Heterostructures, Annu. Rev. Mater. Res. **44**, 65 (2014).

[50] R. Ramesh and D. G. Schlom, Creating Emergent Phenomena in Oxide Superlattices, Nat. Rev. Mater. **4**, 257 (2019).

[51] A. Ohtomo and H. Y. Hwang, A High-Mobility Electron Gas at the $LaAlO_3/SrTiO_3$ Heterointerface, Nature **427**, 423 (2004).

[52] W. Wang, M. W. Daniels, Z. Liao, Y. Zhao, J. Wang, G. Koster, G. Rijnders, C.-Z. Chang, D. Xiao, and W. Wu, Spin Chirality Fluctuation in Two-Dimensional Ferromagnets with Perpendicular Magnetic Anisotropy, Nat. Mater. **18**, 1054 (2019).

[53] J. P. Ruf, H. Paik, N. J. Schreiber, H. P. Nair, L. Miao, J. K. Kawasaki, J. N. Nelson, B. D. Faeth, Y. Lee, B. H. Goodge, B. Pamuk, C. J. Fennie, L. F. Kourkoutis, D. G. Schlom, and K. M. Shen, Strain-Stabilized Superconductivity, Nat. Commun. **12**, 59 (2021).

[54] R. Scherwitzl, S. Gariglio, M. Gabay, P. Zubko, M. Gibert, and J. M. Triscone, Metal-Insulator Transition in Ultrathin $LaNiO_3$ Films, Phys. Rev. Lett. **106**, 246403 (2011).

[55] Z. Liao, F. Li, P. Gao, L. Li, J. Guo, X. Pan, R. Jin, E. W. Plummer, and J. Zhang, Origin of the Metal-Insulator Transition in Ultrathin Films of $La_{2/3}Sr_{1/3}MnO_3$, Phys. Rev. B - Condens. Matter Mater. Phys. **92**, 125123 (2015).

[56] Y. J. Chang, C. H. Kim, S.-H. Phark, Y. S. Kim, J. Yu, and T. W. Noh, Fundamental Thickness Limit of Itinerant Ferromagnetic $SrRuO_3$ Thin Films, Phys. Rev. Lett. **103**, 057201 (2009).

[57] K. Takiguchi, Y. K. Wakabayashi, H. Irie, Y. Krockenberger, T. Otsuka, H. Sawada, S. A. Nikolaev, H. Das, M. Tanaka, Y. Taniyasu, and H. Yamamoto, Quantum Transport Evidence of Weyl Fermions in an Epitaxial Ferromagnetic Oxide, Nat. Commun. **11**, 4969 (2020).

[58] J. Xia, W. Siemons, G. Koster, M. R. Beasley, and A. Kapitulnik, Critical Thickness for Itinerant Ferromagnetism in Ultrathin Films of $SrRuO_3$, Phys. Rev. B **79**, 140407 (2009).

[59] D. Toyota, I. Ohkubo, H. Kumigashira, M. Oshima, T. Ohnishi, M. Lippmaa, M. Takizawa, A.

Fujimori, K. Ono, M. Kawasaki, and H. Koinuma, Thickness-Dependent Electronic Structure of Ultrathin $SrRuO_3$ Films Studied by in Situ Photoemission Spectroscopy, Appl. Phys. Lett. **87**, 1 (2005).

[60] D. Toyota, I. Ohkubo, H. Kumigashira, M. Oshima, T. Ohnishi, M. Lippmaa, M. Kawasaki, and H. Koinuma, Ferromagnetism Stabilization of Ultrathin $SrRuO_3$ Films: Thickness-Dependent Physical Properties, J. Appl. Phys. **99**, 8 (2006).

[61] F. Bern, M. Ziese, A. Setzer, E. Pippel, D. Hesse, and I. Vrejoiu, Structural, Magnetic and Electrical Properties of $SrRuO_3$ Films and $SrRuO_3/SrTiO_3$ Superlattices, J. Phys. Condens. Matter **25**, (2013).

[62] K. Ishigami, K. Yoshimatsu, D. Toyota, M. Takizawa, T. Yoshida, G. Shibata, T. Harano, Y. Takahashi, T. Kadono, V. K. Verma, V. R. Singh, Y. Takeda, T. Okane, Y. Saitoh, H. Yamagami, T. Koide, M. Oshima, H. Kumigashira, and A. Fujimori, Thickness-Dependent Magnetic Properties and Strain-Induced Orbital Magnetic Moment in $SrRuO_3$ Thin Films, Phys. Rev. B - Condens. Matter Mater. Phys. **92**, 3 (2015).

[63] X. Shen, X. Qiu, D. Su, S. Zhou, A. Li, and D. Wu, Thickness-Dependent Metal-Insulator Transition in Epitaxial $SrRuO_3$ Ultrathin Films, J. Appl. Phys. **117**, 015307 (2015).

[64] C. Autieri, Antiferromagnetic and Xy Ferro-Orbital Order in Insulating $SrRuO_3$ Thin Films with SrO Termination, J. Phys. Condens. Matter **28**, (2016).

[65] L. Si, Z. Zhong, J. M. Tomczak, and K. Held, Route to Room-Temperature Ferromagnetic Ultrathin $SrRuO_3$ Films, Phys. Rev. B - Condens. Matter Mater. Phys. **92**, 1 (2015).

[66] K. Gupta, B. Mandal, and P. Mahadevan, Strain-Induced Metal-Insulator Transition in Ultrathin Films of $SrRuO_3$, Phys. Rev. B **90**, 125109 (2014).

[67] M. Meng, Z. Wang, A. Fathima, S. Ghosh, M. Saghayezhian, J. Taylor, R. Jin, Y. Zhu, S. T. Pantelides, J. Zhang, E. W. Plummer, and H. Guo, Interface-Induced Magnetic Polar Metal Phase in Complex Oxides, Nat. Commun. **10**, 5248 (2019).

[68] M. Verissimo-Alves, P. García-Fernández, D. I. Bilc, P. Ghosez, and J. Junquera, Highly Confined Spin-Polarized Two-Dimensional Electron Gas in $SrTiO_3/SrRuO_3$ Superlattices, Phys. Rev. Lett. **108**, 107003 (2012).

[69] B. Sohn, J. R. Kim, C. H. Kim, S. Lee, S. Hahn, Y. Kim, S. Huh, D. Kim, Y. Kim, W. Kyung, M. Kim, M. Kim, T. W. Noh, and C. Kim, Observation of Metallic Electronic Structure in a Single-Atomic-Layer Oxide, Nat. Commun. **12**, 6171 (2021).

[70] S. H. Chang, Y. J. Chang, S. Y. Jang, D. W. Jeong, C. U. Jung, Y. J. Kim, J. S. Chung, and T. W. Noh, Thickness-Dependent Structural Phase Transition of Strained $SrRuO_3$ Ultrathin Films: The Role of Octahedral Tilt, Phys. Rev. B - Condens. Matter Mater. Phys. **84**, 1 (2011).

[71] M. Izumi, K. Nakazawa, Y. Bando, Y. Yoneda, and H. Terauchi, Magnetic Properties of $SrRuO_3/SrTiO_3$ Superlattices, Solid State Ionics **108**, 227 (1998).

[72] M. Izumi, K. Nakazawa, and Y. Bando, TC Suppression of $SrRuO_3/SrTiO_3$ Superlattices, J. Phys. Soc. Japan **67**, 651 (1998).

[73] Z. Cui, A. J. Grutter, H. Zhou, H. Cao, Y. Dong, D. A. Gilbert, J. Wang, Y.-S. Liu, J. Ma, Z. Hu, J. Guo, J. Xia, B. J. Kirby, P. Shafer, E. Arenholz, H. Chen, X. Zhai, and Y. Lu, Correlation-Driven Eightfold Magnetic Anisotropy in a Two-Dimensional Oxide Monolayer, Sci. Adv. **6**, (2020).

[74] H. Boschker, T. Harada, T. Asaba, R. Ashoori, A. V. Boris, H. Hilgenkamp, C. R. Hughes, M. E. Holtz, L. Li, D. A. Muller, H. Nair, P. Reith, X. Renshaw Wang, D. G. Schlom, A. Soukiassian, and J. Mannhart, Ferromagnetism and Conductivity in Atomically Thin $SrRuO_3$, Phys. Rev. X **9**, 011027 (2019).

[75] E. J. Moon, Q. He, S. Ghosh, B. J. Kirby, S. T. Pantelides, A. Y. Borisevich, and S. J. May, Structural " δ Doping" to Control Local Magnetization in Isovalent Oxide Heterostructures, Phys. Rev. Lett. **119**, 197204 (2017).

[76] S. J. May, C. R. Smith, J. W. Kim, E. Karapetrova, A. Bhattacharya, and P. J. Ryan, Control of Octahedral Rotations in $(LaNiO_3)^n/(SrMnO_3)^m$ Superlattices, Phys. Rev. B - Condens. Matter Mater. Phys. **83**, 2 (2011).

[77] N. Nakagawa, H. Y. Hwang, and D. A. Muller, Why Some Interfaces Cannot Be Sharp, Nat. Mater. **5**, 204 (2006).

[78] L. Capogna, A. P. Mackenzie, A. P. Mackenzie, R. S. Perry, S. A. Grigera, L. M. Galvin, P. Raychaudhuri, A. J. Schofield, C. S. Alexander, G. Cao, S. R. Julian, and Y. Maeno, Sensitivity to Disorder of the Metallic State in the Ruthenates, Phys. Rev. Lett. **88**, 766021 (2002).

[79] H. P. Nair, Y. Liu, J. P. Ruf, N. J. Schreiber, S. L. Shang, D. J. Baek, B. H. Goodge, L. F. Kourkoutis, Z. K. Liu, K. M. Shen, and D. G. Schlom, Synthesis Science of $SrRuO_3$ and $CaRuO_3$ Epitaxial Films with High Residual Resistivity Ratios, APL Mater. **6**, (2018).

[80] W. Siemons, G. Koster, A. Vailionis, H. Yamamoto, D. H. A. Blank, and M. R. Beasley, Dependence of the Electronic Structure of $SrRuO_3$ and Its Degree of Correlation on Cation Off-Stoichiometry, Phys. Rev. B - Condens. Matter Mater. Phys. **76**, 075126 (2007).

[81] B. I. Shklovskii and A. L. Efros, Electronic Properties of Doped Semiconductors, Vol. 45 (Springer Berlin Heidelberg, 1984).

[82] V. F. Gantmakher and L. I. Man, Electrons and Disorder in Solids (Oxford University Press, 2005).

[83] D. C. Licciardello and D. J. Thouless, Constancy of Minimum Metallic Conductivity in Two Dimensions, Phys. Rev. Lett. **35**, 1475 (1975).

[84] N. E. Hussey, K. Takenaka, and H. Takagi, Universality of the Mott–Ioffe–Regel Limit in Metals, Http://Dx.Doi.Org/10.1080/14786430410001716944 **84**, 2847 (2007).

[85] P. A. Lee and T. V. Ramakrishnan, Disordered Electronic Systems, Rev. Mod. Phys. **57**, 287 (1985).

[86] N. Furukawa, Transport Properties of the Kondo Lattice Model in the Limit S= ∞ and D= ∞, J. Phys. Soc. Japan **63**, 3214 (1994).

[87] Y. Tokura, A. Urushibara, T. Arima, Y. Moritomo, A. Asamitsu, G. Kido, and N. Furukawa, Giant Magnetotransport Phenomena in Filling-Controlled Kondo Lattice System: $La_{1-x}Sr_xMnO_3$, J. Phys. Soc. Japan **63**, 3931 (1994).

[88] J. Fontcuberta, B. Martínez, A. Seffar, S. Piñol, J. L. García-Muñoz, and X. Obradors, Colossal Magnetoresistance of Ferromagnetic Manganites: Structural Tuning and Mechanisms, Phys. Rev. Lett. **76**, 1122 (1996).

[89] Y. Tomioka, A. Asamitsu, and Y. Tokura, Magnetotransport Properties and Magnetostructural Phenomenon in Single Crystals of $La_{0.7}(Ca_{1-y}Sr_y)MnO_3$, Phys. Rev. B - Condens. Matter Mater. Phys. **63**, 024421 (2001).

[90] J. Wu, J. W. Lynn, C. J. Glinka, J. Burley, H. Zheng, J. F. Mitchell, and C. Leighton, Intergranular Giant Magnetoresistance in a Spontaneously Phase Separated Perovskite Oxide, Phys. Rev. Lett. **94**, 037201 (2005).

[91] J. Q. Xiao, J. S. Jiang, and C. L. Chien, Giant Magnetoresistance in Nonmultilayer Magnetic Systems, Phys. Rev. Lett. **68**, 3749 (1992).

[92] L. M. Wang, H. E. Horng, and H. C. Yang, Anomalous Magnetotransport in $SrRuO_3$ Films: A Crossover from Fermi-Liquid to Non-Fermi-Liquid Behavior, Phys. Rev. B - Condens. Matter Mater. Phys. **70**, 014433 (2004).

[93] D. B. Kacedon, R. A. Rao, and C. B. Eom, Magnetoresistance of Epitaxial Thin Films of Ferromagnetic Metallic Oxide $SrRuO_3$ with Different Domain Structures, Appl. Phys. Lett. **71**, 1724 (1997).

[94] D. J. Singh, Electronic and Magnetic Properties of the 4d Itinerant Ferromagnet $SrRuO_3$, J. Appl. Phys. **79**, 4818 (1996).

[95] L. F. Kourkoutis, J. H. Song, H. Y. Hwang, and D. A. Muller, Microscopic Origins for Stabilizing Room-Temperature Ferromagnetism in Ultrathin Manganite Layers, Proc. Natl. Acad. Sci. U. S. A. **107**, 11682 (2010).

[96] H. Y. Hwang, Y. Iwasa, M. Kawasaki, B. Keimer, N. Nagaosa, and Y. Tokura, Emergent Phenomena at Oxide Interfaces, Nat. Mater. **11**, 103 (2012).

[97] H. Lee, N. Campbell, J. Lee, T. J. Asel, T. R. Paudel, H. Zhou, J. W. Lee, B. Noesges, J. Seo, B. Park, L. J. Brillson, S. H. Oh, E. Y. Tsymbal, M. S. Rzchowski, and C. B. Eom, Direct Observation of a Two-Dimensional Hole Gas at Oxide Interfaces, Nat. Mater. **17**, 231 (2018).

[98] M. Saghayezhian, S. Kouser, Z. Wang, H. Guo, R. Jin, J. Zhang, Y. Zhu, S. T. Pantelides, and E. W. Plummer, Atomic-Scale Determination of Spontaneous Magnetic Reversal in Oxide Heterostructures, Proc. Natl. Acad. Sci. **116**, 10309 (2019).

[99] K. S. Takahashi, M. Kawasaki, and Y. Tokura, Interface Ferromagnetism in Oxide Superlattices of $CaMnO_3/CaRuO_3$, Appl. Phys. Lett. **79**, 1324 (2001).

[100] R. J. Bouchard and J. L. Gillson, Electrical Properties of $CaRuO_3$ and $SrRuO_3$ Single Crystals, Mater. Res. Bull. **7**, 873 (1972).

[101] G. Cao, S. McCall, M. Shepard, J. E. Crow, and R. P. Guertin, Thermal, Magnetic, and Transport Properties of Single-Crystal $Sr_{1-x}Ca_xRuO_3$ ($0<x<1.0$), Phys. Rev. B **56**, 321 (1997).

[102] L. T. Nguyen, M. Abeykoon, J. Tao, S. Lapidus, and R. J. Cava, Long-Range and Local Crystal Structures of the $Sr_{1-x}Ca_xRuO_3$ Perovskites, Phys. Rev. Mater. **4**, 034407 (2020).

[103] C. B. Eom, R. J. Cava, R. M. Fleming, J. M. Phillips, R. B. Van Dover, J. H. Marshall, J. W. P. Hsu, J. J. Krajewski, and W. F. Peck, Single-Crystal Epitaxial Thin Films of the Isotropic Metallic Oxides $Sr_{1-x}Ca_xRuO3$ ($0 \leq x \leq 1$), Science. **258**, 1766 (1992).

[104] R. A. Rao, Q. Gan, C. B. Eom, R. J. Cava, Y. Suzuki, J. J. Krajewski, S. C. Gausepohl, and M. Lee, Strain Stabilized Metal–Insulator Transition in Epitaxial Thin Films of Metallic Oxide $CaRuO_3$, Appl. Phys. Lett. **70**, 3035 (1998).

[105] S. Hyun, J. H. Cho, A. Kim, J. Kim, T. Kim, and K. Char, Coexistence of Metallic and Insulating Phases in Epitaxial $CaRuO_3$ Thin Films Observed by Scanning Microwave Microscopy, Appl. Phys. Lett. **80**, 1574 (2002).

[106] T. He and R. J. Cava, The Effect of Ru-Site Dopants on the Magnetic Properties of $CaRuO_3$, J. Phys. Condens. Matter **13**, 8347 (2001).

[107] V. Hardy, B. Raveau, R. Retoux, N. Barrier, and A. Maignan, Nature of the Ferromagnetism Induced by Nonmagnetic Substitutions on the Ru Site of $CaRuO_3$, Phys. Rev. B **73**, 094418 (2006).

[108] S. Shen, Z. Li, Z. Tian, W. Luo, S. Okamoto, and P. Yu, Emergent Ferromagnetism with Fermi-Liquid Behavior in Proton Intercalated $CaRuO_3$, Phys. Rev. X **11**, 021018 (2021).

[109] J. Y. Zhang, J. Hwang, S. Raghavan, and S. Stemmer, Symmetry Lowering in Extreme-Electron-Density Perovskite Quantum Wells, Phys. Rev. Lett. **110**, 256401 (2013).

[110] A. M. Glazer, The Classification of Tilted Octahedra in Perovskites, Acta Crystallogr. Sect. B Struct. Crystallogr. Cryst. Chem. **28**, 3384 (1972).

[111] P. M. Woodward, Octahedral Tilting in Perovskites. I. Geometrical Considerations, Acta Crystallogr. Sect. B Struct. Sci. **53**, 32 (1997).

[112] P. Siwakoti, Z. Wang, M. Saghayezhian, D. Howe, Z. Ali, Y. Zhu, and J. Zhang, Abrupt Orthorhombic Relaxation in Compressively Strained Ultra-Thin $SrRuO_3$ Films, Phys. Rev. Mater. **5**, 114409 (2021).

[113] R. Gao, Y. Dong, H. Xu, H. Zhou, Y. Yuan, V. Gopalan, C. Gao, D. D. Fong, Z. Chen, Z. Luo, and

L. W. Martin, Interfacial Octahedral Rotation Mismatch Control of the Symmetry and Properties of $SrRuO_3$, ACS Appl. Mater. Interfaces **8**, 14871 (2016).

[114] J. C. Jiang, W. Tian, X. Q. Pan, Q. Gan, and C. B. Eom, Domain Structure of Epitaxial SrRuO3 Thin Films on Miscut (001) $SrTiO_3$ Substrates, Appl. Phys. Lett. **72**, 2963 (1998).

[115] E. J. Moon, R. Colby, Q. Wang, E. Karapetrova, C. M. Schlepütz, M. R. Fitzsimmons, and S. J. May, Spatial Control of Functional Properties via Octahedral Modulations in Complex Oxide Superlattices, Nat. Commun. **5**, 5710 (2014).

[116] A. Biswas, K.-S. Kim, and Y. H. Jeong, Metal Insulator Transitions in Perovskite SrIrO3 Thin Films, J. Appl. Phys. **116**, 213704 (2014).

[117] G. Wang, Z. Wang, M. Meng, M. Saghayezhian, L. Chen, C. Chen, H. Guo, Y. Zhu, E. W. Plummer, and J. Zhang, Role of Disorder and Correlations in the Metal-Insulator Transition in Ultrathin $SrVO_3$ Films, Phys. Rev. B **100**, 155114 (2019).

[118] Z. Ali, D. Basaula, K. F. Eid, and M. Khan, Anisotropic Properties of Oblique Angle Deposited Permalloy Thin Films, Thin Solid Films **735**, 138899 (2021).

[119] B. L. Altshuler, A. G. Aronov, and P. A. Lee, Interaction Effects in Disordered Fermi Systems in Two Dimensions, Phys. Rev. Lett. **44**, 1288 (1980).

[120] A. L. Efros and B. I. Shklovskii, Coulomb Gap and Low Temperature Conductivity of Disordered Systems, J. Phys. C Solid State Phys. **8**, L49 (1975).

[121] P. W. Anderson, Absence of Diffusion in Certain Random Lattices, Phys. Rev. **109**, 1492 (1958).

[122] T. Ying, Y. Gu, X. Chen, X. Wang, S. Jin, L. Zhao, W. Zhang, and X. Chen, Anderson Localization of Electrons in Single Crystals: $Li_xFe_7Se_8$, Sci. Adv. **2**, e150123 (2016).

[123] H. Volker, P. Jost, and M. Wuttig, Low-Temperature Transport in Crystalline $Ge_1Sb_2Te_4$, Adv. Funct. Mater. **25**, 6390 (2015).

[124] N. V. Lien and R. Rosenbaum, General Crossovers from Two-Dimensional Mott $T^{-1/3}$ to Soft-Gap $T^{-\nu}$ Variable-Range Hopping, Phys. Rev. B **56**, 14960 (1997).

[125] C. Lu, A. Quindeau, H. Deniz, D. Preziosi, D. Hesse, and M. Alexe, Crossover of Conduction Mechanism in Sr_2IrO_4 Epitaxial Thin Films, Appl. Phys. Lett. **105**, 082407 (2014).

[126] G. Bergmann, Weak Localization in Thin Films: A Time-of-Flight Experiment with Conduction Electrons, Phys. Rep. **107**, 1 (1984).

[127] P. A. Lee and T. V. Ramakrishnan, Magnetoresistance of Weakly Disordered Electrons, Phys. Rev. B **26**, 4009 (1982).

[128] H. T. Dang, J. Mravlje, A. Georges, and A. J. Millis, Electronic Correlations, Magnetism, and Hund's Rule Coupling in the Ruthenium Perovskites $SrRuO_3$ and $CaRuO_3$, Phys. Rev. B - Condens. Matter Mater. Phys. **91**, 1 (2015).

[129] Z. Ali, D. Basaula, W. Zhou, J. Brock, M. Khan, and K. F. Eid, Controlling the Charge Transport Mode in Permalloy Films Using Oblique Angle Deposition, J. Magn. Magn. Mater. **484**, 430 (2019).

[130] Z. Ali, Z. Wang, A. O'Hara, M. Saghayezhian, D. Shin, Y. Zhu, S. T. Pantelides, and J. Zhang, Origin of Insulating and Non-Ferromagnetic $SrRuO_3$ Monolayers, Phys. Rev. B **105**, 054429 (2022).

[131] M. B. Salamon, P. Lin, and S. H. Chun, Colossal Magnetoresistance Is a Griffiths Singularity, Phys. Rev. Lett. **88**, 197203 (2002).

[132] P. Tong, B. Kim, D. Kwon, T. Qian, S. I. Lee, S. W. Cheong, and B. G. Kim, Griffiths Phase and Thermomagnetic Irreversibility Behavior in Slightly Electron-Doped Manganites $Sm_{1-x}Ca_xMnO_3$ ($0.80 \leq x \leq 0.92$), Phys. Rev. B **77**, 184432 (2008).

[133] J. Deisenhofer, D. Braak, H. A. Krug Von Nidda, J. Hemberger, R. M. Eremina, V. A. Ivanshin, A. M. Balbashov, G. Jug, A. Loidl, T. Kimura, and Y. Tokura, Observation of a Griffiths Phase in Paramagnetic $La_{1-x}Sr_xMnO_3$, Phys. Rev. Lett. **95**, 2 (2005).

[134] A. K. Pramanik and A. Banerjee, Griffiths Phase and Its Evolution with Mn-Site Disorder in the Half-Doped Manganite $Pr_{0.5}Sr_{0.5}Mn_{1-y}Ga_yO_3$ (Y=0.0, 0.025, and 0.05), Phys. Rev. B **81**, 1 (2010).

[135] J. G. Cheng, J. S. Zhou, and J. B. Goodenough, Lattice Effects on Ferromagnetism in Perovskite Ruthenates, Proc. Natl. Acad. Sci. U. S. A. **110**, 13312 (2013).

[136] J. S. Zhou, K. Matsubayashi, Y. Uwatoko, C. Q. Jin, J. G. Cheng, J. B. Goodenough, Q. Q. Liu, T. Katsura, A. Shatskiy, and E. Ito, Critical Behavior of the Ferromagnetic Perovskite $BaRuO_3$, Phys. Rev. Lett. **101**, 3 (2008).

[137] H. Guo, Z. Wang, S. Dong, S. Ghosh, M. Saghayezhian, L. Chen, Y. Weng, A. Herklotz, T. Z. Ward, R. Jin, S. T. Pantelides, Y. Zhu, J. Zhang, and E. W. Plummer, Interface-Induced Multiferroism by Design in Complex Oxide Superlattices, Proc. Natl. Acad. Sci. U. S. A. **114**, E5062 (2017).

[138] C. Domínguez, A. B. Georgescu, B. Mundet, Y. Zhang, J. Fowlie, A. Mercy, A. Waelchli, S. Catalano, D. T. L. Alexander, P. Ghosez, A. Georges, A. J. Millis, M. Gibert, and J. M. Triscone, Length Scales of Interfacial Coupling between Metal and Insulator Phases in Oxides, Nat. Mater. **19**, 1182 (2020).

[139] B. Chen, N. Gauquelin, R. J. Green, J. H. Lee, C. Piamonteze, M. Spreitzer, D. Jannis, J. Verbeeck, M. Bibes, M. Huijben, G. Rijnders, and G. Koster, Spatially Controlled Octahedral Rotations and Metal-Insulator Transitions in Nickelate Superlattices, Nano Lett. **21**, 1295 (2021).

[140] J. Wang, J. B. Neaton, H. Zheng, V. Nagarajan, S. B. Ogale, B. Liu, D. Viehland, V. Vaithyanathan, D. G. Schlom, U. V. Waghmare, N. A. Spaldin, K. M. Rabe, M. Wuttig, and R. Ramesh, Epitaxial $BiFeO_3$ Multiferroic Thin Film Heterostructures, Science (80-.). **299**, 1719 (2003).

[141] S. Lin, Q. Zhang, M. A. Roldan, S. Das, T. Charlton, M. R. Fitzsimmons, Q. Jin, S. Li, Z. Wu, S. Chen, H. Guo, X. Tong, M. He, C. Ge, C. Wang, L. Gu, K. J. Jin, and E. J. Guo, Switching Magnetic Anisotropy of $SrRuO_3$ by Capping-Layer-Induced Octahedral Distortion, Phys. Rev. Appl. **13**, 1 (2020).

[142] D. Yia, J. Liu, S. L. Hsu, L. Zhang, Y. Choi, J. W. Kim, Z. Chen, J. D. Clarkson, C. R. Serrao, E. Arenholz, P. J. Ryan, H. Xu, R. J. Birgeneau, and R. Ramesh, Atomic-Scale Control of Magnetic Anisotropy via Novel Spin-Orbit Coupling Effect in $La_{2/3}Sr_{1/3}MnO_3/SrIrO_3$ Superlattices, Proc. Natl. Acad. Sci. U. S. A. **113**, 6397 (2016).

[143] D. Yi, C. L. Flint, P. P. Balakrishnan, K. Mahalingam, B. Urwin, A. Vailionis, A. T. N'Diaye, P. Shafer, E. Arenholz, Y. Choi, K. H. Stone, J. H. Chu, B. M. Howe, J. Liu, I. R. Fisher, and Y. Suzuki, Tuning Perpendicular Magnetic Anisotropy by Oxygen Octahedral Rotations in $(La_{1-x}Sr_xMnO_3)/(SrIrO_3)$ Superlattices, Phys. Rev. Lett. **119**, 1 (2017).

[144] B. Dieny and M. Chshiev, Perpendicular Magnetic Anisotropy at Transition Metal/Oxide Interfaces and Applications, Rev. Mod. Phys. **89**, 025008 (2017).

[145] Z. Ali, M. Saghayezhian, Z. Wang, A. O'hara, D. Shin, W. Ge, Y.-T. Chan, W. Wu, S. Pantelides, Y. Zhu, and J. Zhang, Emergent Unusual Ferromagnetism and Insulator-Metal Transition in δ-Doped Ultrathin Ruthenates, (2022).

[146] D. G. Schlom, L.-Q. Chen, C.-B. Eom, K. M. Rabe, S. K. Streiffer, and J.-M. Triscone, Strain Tuning of Ferroelectric Thin Films, Annu. Rev. Mater. Res. **37**, 589 (2007).

[147] J. H. Lee, P. Murugavel, H. Ryu, D. Lee, J. Y. Jo, J. W. Kim, H. J. Kim, K. H. Kim, Y. Jo, M. H. Jung, Y. H. Oh, Y. W. Kim, J. G. Yoon, J. S. Chung, and T. W. Noh, Epitaxial Stabilization of a New Multiferroic Hexagonal Phase of $TbMnO_3$ Thin Films, Adv. Mater. **18**, 3125 (2006).

[148] J. H. Haeni, P. Irvin, W. Chang, R. Uecker, P. Reiche, Y. L. Li, S. Choudhury, W. Tian, M. E. Hawley, B. Craigo, A. K. Tagantsev, X. Q. Pan, S. K. Streiffer, L. Q. Chen, S. W. Kirchoefer, J. Levy, and D. G. Schlom, Room-Temperature Ferroelectricity in Strained $SrTiO_3$, Nature **430**, 758 (2004).

[149] P. A. Salvador, T. D. Doan, B. Mercey, and B. Raveau, Stabilization of $YMnO_3$ in a Perovskite Structure as a Thin Film, Chem. Mater. **10**, 2592 (1998).

[150] O. Y. Gorbenko, S. V. Samoilenkov, I. E. Graboy, and A. R. Kaul, Epitaxial Stabilization of Oxides in Thin Films, Chem. Mater. **14**, 4026 (2002).

[151] S. A. Lee, J. M. Ok, J. Lee, J. Y. Hwang, S. Yoon, S. J. Park, S. Song, J. S. Bae, S. Park, H. N. Lee, and W. S. Choi, Epitaxial Stabilization of Metastable 3C $BaRuO_3$ Thin Film with Ferromagnetic Non-Fermi Liquid Phase, Adv. Electron. Mater. **7**, (2021).

[152] K. J. Choi, S. H. Baek, H. W. Jang, L. J. Belenky, M. Lyubchenko, and C. B. Eom, Phase-Transition Temperatures of Strained Single-Crystal $SrRuO_3$ Thin Films, Adv. Mater. **22**, 759 (2010).

[153] W. Lu, P. Yang, W. D. Song, G. M. Chow, and J. S. Chen, Control of Oxygen Octahedral Rotations

and Physical Properties in $SrRuO_3$ Films, Phys. Rev. B - Condens. Matter Mater. Phys. **88**, 1 (2013).

[154] A. Herklotz, A. T. Wong, T. Meyer, M. D. Biegalski, H. N. Lee, and T. Z. Ward, Controlling Octahedral Rotations in a Perovskite via Strain Doping, Sci. Rep. **6**, 1 (2016).

[155] A. J. Grutter, F. J. Wong, E. Arenholz, A. Vailionis, and Y. Suzuki, Evidence of High-Spin Ru and Universal Magnetic Anisotropy in $SrRuO_3$ Thin Films, Phys. Rev. B - Condens. Matter Mater. Phys. **85**, 1 (2012).

[156] L. Klein, J. S. Dodge, T. H. Geballe, A. Kapitulnik, A. F. Marshall, L. Antognazza, and K. Char, Perpendicular Magnetic Anisotropy and Strong Magneto-optic Properties of $SrRuO_3$ Epitaxial Films, Appl. Phys. Lett. **66**, 2427 (1998).

[157] R. Palai, H. Huhtinen, J. F. Scott, and R. S. Katiyar, Observation of Spin-Glass-like Behavior in $SrRuO_3$ Epitaxial Thin Films, Phys. Rev. B **79**, 104413 (2009).

[158] H. T. Dang, J. Mravlje, A. Georges, and A. J. Millis, Electronic Correlations, Magnetism and Hund's Rule Coupling in the Ruthenium Perovskites $SrRuO_3$ and $CaRuO_3$, Phys. Rev. B - Condens. Matter Mater. Phys. **91**, 195149 (2015).

[159] S. Kunkemöller, K. Jenni, D. Gorkov, A. Stunault, S. Streltsov, and M. Braden, Magnetization Density Distribution in the Metallic Ferromagnet $SrRuO_3$ Determined by Polarized Neutron Diffraction, Phys. Rev. B **100**, 1 (2019).

[160] P. G. Radaelli, G. Iannone, M. Marezio, H. Y. Hwang, S.-W. Cheong, J. D. Jorgensen, and D. N. Argyriou, Structural Effects on the Magnetic and Transport Properties of Perovskite $A_{1-x}A'_xMnO_3$ (X=0.25, 0.30), Phys. Rev. B **56**, 8265 (1997).

Vita

Zeeshan Ali was born in Rawalpindi, Pakistan in 1989. He finished his undergraduate degree in physics from University of Punjab, Lahore, Pakistan in Dec, 2014. He came to USA in July 2016, and completed a Masters in physics from Miami University, OH. Immediately after, he started his PhD in department of physics and astronomy at Louisiana State University. He expects to receive his Doctor of Philosophy degree in December, 2022.